

Modeling And Control  
of a Quadrotor Aircraft  
UAV

by

Aniket Ravindra Shirsat

Applied Project Presented in Partial Fulfillment  
of the Requirement for the Degree  
Master of Science

Approved April 2015 by the  
Graduate Supervisory Committee:

Panagiotis Artemiadis, Chair  
Armando A Rodriguez

ARIZONA STATE UNIVERSITY

May 2015

## ABSTRACT

Given the increasing use of quadrotor vehicle applications, this project seeks to identify critical trade-offs with respect to modeling, control and vehicle design. With this goal, we focus on a very generic/standard quadrotor configuration. A two control nonlinear 3DOF (degree of freedom) model for the vehicles longitudinal dynamics is used as the basis for all developments. The model is used to investigate how the static and dynamic properties of the vehicle change as function of the flight condition as well as mass and geometry. This analysis is used to make control-centric recommendations with respect to vehicle design. While the two-input two-output system is decoupled at hover, it becomes coupled with forward speed. Comprehensive trade-offs are provided using a classical lead lag control architecture.

## TABLE OF CONTENTS

	Page
LIST OF FIGURES .....	iv
LIST OF TABLES .....	viii
1 INTRODUCTION AND OVERVIEW .....	1
1.1 Historical Perspective .....	1
1.2 Modern Day Quadrotor .....	7
2 NON-LINEAR MODEL OF THE QUADROTOR .....	12
2.1 Introduction .....	12
2.2 Assumptions .....	12
2.3 Reference Frames .....	12
2.4 Kinematics .....	13
2.5 Dynamics .....	17
2.5.1 Forces .....	17
2.5.2 Moments .....	18
2.5.3 Moment of Inertia .....	21
2.5.4 Newton-Euler equations .....	23
2.5.5 Euler-Lagrange Equations .....	23
2.6 Summary and Conclusions .....	27
3 LINEAR MODELS .....	28
3.1 Introduction .....	28
3.2 Linearisation .....	28
3.3 Longitudinal Models .....	31
3.4 Impact of flight condition .....	32
3.4.1 Vertical Flight .....	32
3.4.2 Forward Flight .....	40

CHAPTER	Page
3.4.3 Forward and Vertical Flight .....	52
3.5 Impact of Mass and Length.....	58
3.5.1 Impact of mass change .....	59
3.5.2 Impact of Length change .....	65
4 Control Design .....	71
4.1 Longitudinal mode Controller Design.....	71
4.1.1 Controller design for transfer function from Thrust to $\dot{z}$ .....	72
4.1.2 Controller design for transfer function from $\tau_{theta}$ to $\dot{x}$ .....	72
4.1.3 Sensitivity .....	74
4.1.4 Complimentary Sensitivity.....	77
4.1.5 Reference to control action .....	80
4.1.6 Disturbance to output .....	83
4.1.7 % Overshoot .....	86
4.1.8 Settling Time .....	89
4.2 Controller simulation.....	91
4.2.1 Linear Simulation .....	97
4.3 Summary and Conclusions .....	99
5 SUMMARY AND DIRECTIONS FOR FUTURE RESEARCH .....	100
5.1 Summary .....	100
5.2 Directions for Future Research .....	100
REFERENCES .....	101
APPENDIX	

## LIST OF FIGURES

Figure	Page
1.1 Leonardo da Vinci's Aerial Screw .....	1
1.2 Sir George Cayley's helicopter design .....	2
1.3 Enrico Forlanini's helicopter design .....	3
1.4 Louis Berguet Gyroplane No.1 .....	4
1.5 Paul Cornu Twin Rotor Helicopter .....	5
1.6 Bothezat Four Rotor Design .....	6
1.7 ConvertaWings's Model A helicopter .....	7
1.8 Mesicopter battery powered prototype .....	8
1.9 X4 Flyer Mark II .....	9
1.10 STARMAC platform .....	10
1.11 Quadrotors in hover in the flying Machine Arena .....	11
1.12 Swarm of Nano Quadrotors .....	11
2.1 Inertial and Body reference frame for a Quadrotor.....	17
2.2 Roll moment about the earth x axis .....	19
2.3 Pitch moment about the earth y axis .....	20
2.4 Yaw movement about the earth z axis .....	21
2.5 Schematic for inertia calculation .....	22
3.1 Variation of Thrust with flight condition.....	34
3.2 Variation of Tautheta with flight condition.....	35
3.3 Gain(1,1) element variation with flight condition .....	36
3.4 Gain(2,2) variation with flight condition .....	37
3.5 Frequency Response magnitude and phase plot for element (1,1) for vertical flight condition .....	38

CHAPTER	Page
3.6 Frequency Response magnitude and phase plot for element(2,2) for vertical flight condition .....	39
3.7 Analytical and numeric validation of Thrust .....	41
3.8 $\tau_\theta$ variation with forward flight .....	42
3.9 Comparison of Gain(1,1) analytic and numeric .....	43
3.10 Comparison of Gain(1,2) analytic and numeric .....	44
3.11 Comparison of Gain(2,1) analytic and numeric .....	45
3.12 Comparison of Gain(2,2) analytic and numeric .....	46
3.13 Frequency Response magnitude & phase plot for element (1,1): forward flight condition .....	47
3.14 Frequency Response magnitude & phase plot for element (1,2): forward flight .....	48
3.15 Frequency Response magnitude & phase plot for element (2,1) : forward flight condition .....	49
3.16 Frequency Response magnitude & phase plot for element (2,2): forward flight condition .....	50
3.17 Thrust Variation .....	52
3.18 Variation of $\tau_\theta$ .....	53
3.19 Variation of $\tau_\theta$ .....	54
3.20 Variation of Gain(1,1) .....	55
3.21 Variation of Gain(1,2) .....	56
3.22 variation of Gain(2,1) .....	57
3.23 Variation of Gain(2,2) with the flight condition 4 .....	58
3.24 Variation of Thrust for with mass=1.5 kg and forward velocity .....	59

CHAPTER	Page
3.25 Variation of Thrust with mass=3 kg and forward velocity .....	60
3.26 Variation of Gain(1,1) with the mass .....	61
3.27 Variation of Gain(1,2) with the mass .....	62
3.28 Variation of Gain(2,1) with the mass .....	63
3.29 Variation of Gain(2,2) with the mass .....	64
3.30 System poles variation with mass .....	65
3.31 Variation of gain(1,1) with length .....	66
3.32 Variation of gain(1,2) with length .....	67
3.33 Variation of gain(2,1) with length .....	68
3.34 Variation of gain(2,2) with length .....	69
3.35 System poles variation with length .....	70
4.1 Visualization of Standard Negative Feedback Loop .....	71
4.2 Sensitivity ( $\zeta$ vs $\omega_g$ ) for PM=45 deg .....	74
4.3 Sensitivity ( $\zeta$ vs $\omega_g$ ) for PM=60 deg .....	75
4.4 Sensitivity ( $\zeta$ vs $\omega_g$ ) for PM=70 deg .....	76
4.5 Reference to output ( $\zeta$ vs $\omega_g$ ) for PM 45 deg .....	77
4.6 Reference to output ( $\zeta$ vs $\omega_g$ ) for PM 60 deg .....	78
4.7 Reference to output ( $\zeta$ vs $\omega_g$ ) for PM 70 deg .....	79
4.8 Reference to control action ( $\zeta$ vs $\omega_g$ ) for PM 45 deg.....	80
4.9 Reference to control action ( $\zeta$ vs $\omega_g$ ) for PM 60 deg.....	81
4.10 Reference to control action ( $\zeta$ vs $\omega_g$ ) for PM 70 deg.....	82
4.11 Input disturbances to output ( $\zeta$ vs $\omega_g$ ) for PM 45 deg.....	83
4.12 Input disturbances to output ( $\zeta$ vs $\omega_g$ ) for PM 60 deg .....	84
4.13 Input disturbances to output ( $\zeta$ vs $\omega_g$ ) for PM 70 deg .....	85

CHAPTER	Page
4.14 % $M_p$ ( $\zeta$ vs $\omega_g$ ) for PM 45 deg .....	86
4.15 % $M_p$ ( $\zeta$ vs $\omega_g$ ) for PM 60 deg .....	87
4.16 % $M_p$ ( $\zeta$ vs $\omega_g$ ) for PM 70 deg .....	88
4.17 $T_s$ ( $\zeta$ vs $\omega_g$ ) for PM 45 deg.....	89
4.18 $T_s$ ( $\zeta$ vs $\omega_g$ ) for PM 60 deg.....	90
4.19 Nominal Plant :P .....	91
4.20 Controller .....	92
4.21 Open Loop : L .....	93
4.22 Sensitivity : $ S_o $ .....	94
4.23 Complimentary Sensitivity : $ T_o $ .....	95
4.24 Reference to Control Action : $ KS $ .....	96
4.25 Input Disturbance to Output : $ PS $ .....	97
4.26 Step response: Hover Controller .....	98
4.27 Step response: $\dot{x} = 1$ m/s.....	99

## LIST OF TABLES

Table	Page
3.1 Nominal Parameters .....	33
3.2 Variation of Bode magnitude with flight condition .....	50

# Chapter 1

## INTRODUCTION AND OVERVIEW

### 1.1 Historical Perspective

Quadrotor as the name suggests consists of four main rotors that are mounted on a frame that is usually X in shape. Two motors rotate counterclockwise and remaining two rotate clockwise. For understanding the current configuration, we have to understand the development of rotary wing vehicle design throughout history.

Rotary wing vehicles have been around since the beginning of 19th century. But the concept of rotary wing vehicles has been around since the times of Leonardo da Vinci. The Figure 1.1 shows the construction of the Leonardo da Vinci's helix or the Aerial Screw.

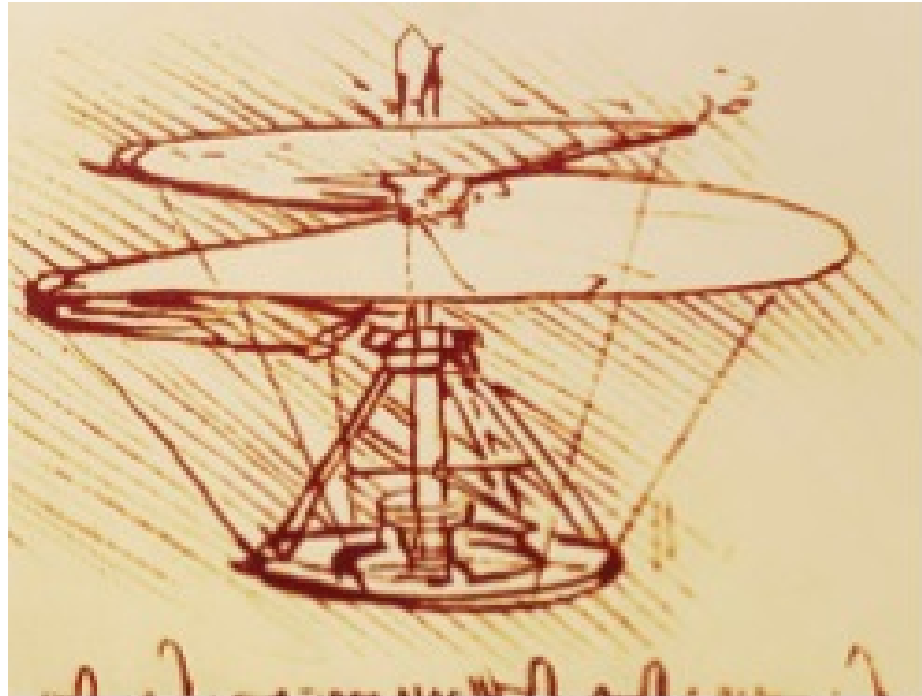


**Figure 1.1:** Leonardo da Vinci's Aerial Screw

In the early 1800, Sir George Cayley designed models that were capable of vertical flight but they could not work because of the lack of an appropriate propulsion system [3] Cayley's design used two counter-rotating rotors as shown in the Figure 1.2

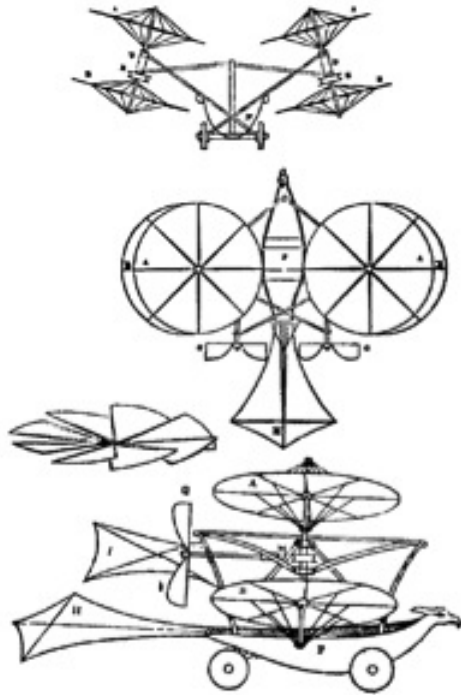


**Figure 1.2:** Sir George Cayley's helicopter design

In 1878, an Italian professor Enrico Forlanini overcame the problem of propulsion system by using super-heated steam. His model was able to achieve a height of forty feet but could not sustain flight for longer duration. Steam engine had a very low power to weight ratio. The Figure 1.3 shows his design.

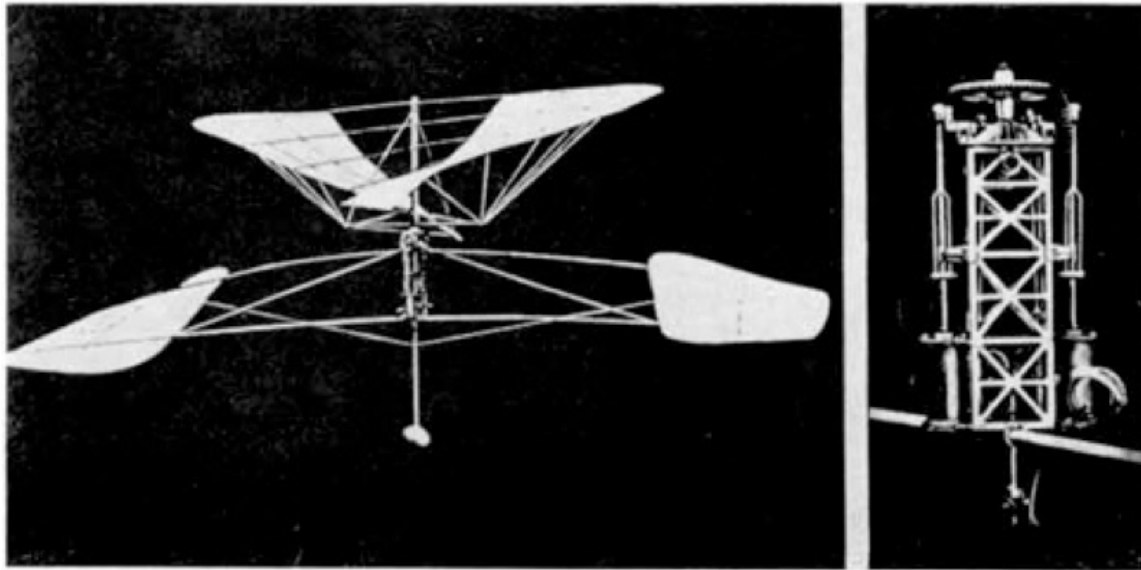


**Figure 1.3:** Enrico Forlanini’s helicopter design

In 1880, Thomas Alva Edison sought to solve the propulsion problem by the use of electric motors. He was successful in generating 160 pounds of lift but could not produce more powerful electric motors with the technology of the day.

At the start of the 20th century the problem of propulsion was solved by the invention of the internal combustion engines. These engines were able to provide much more power to weight ratio than the steam engines of the 19th century.

In 1907, Louis Breguet designed and built Gyroplane No.1, which was able to reach a height of two feet and remain airborne for two minutes. His design, as depicted in Figure 1.4 was probably the earliest known design of a Quadrotor.

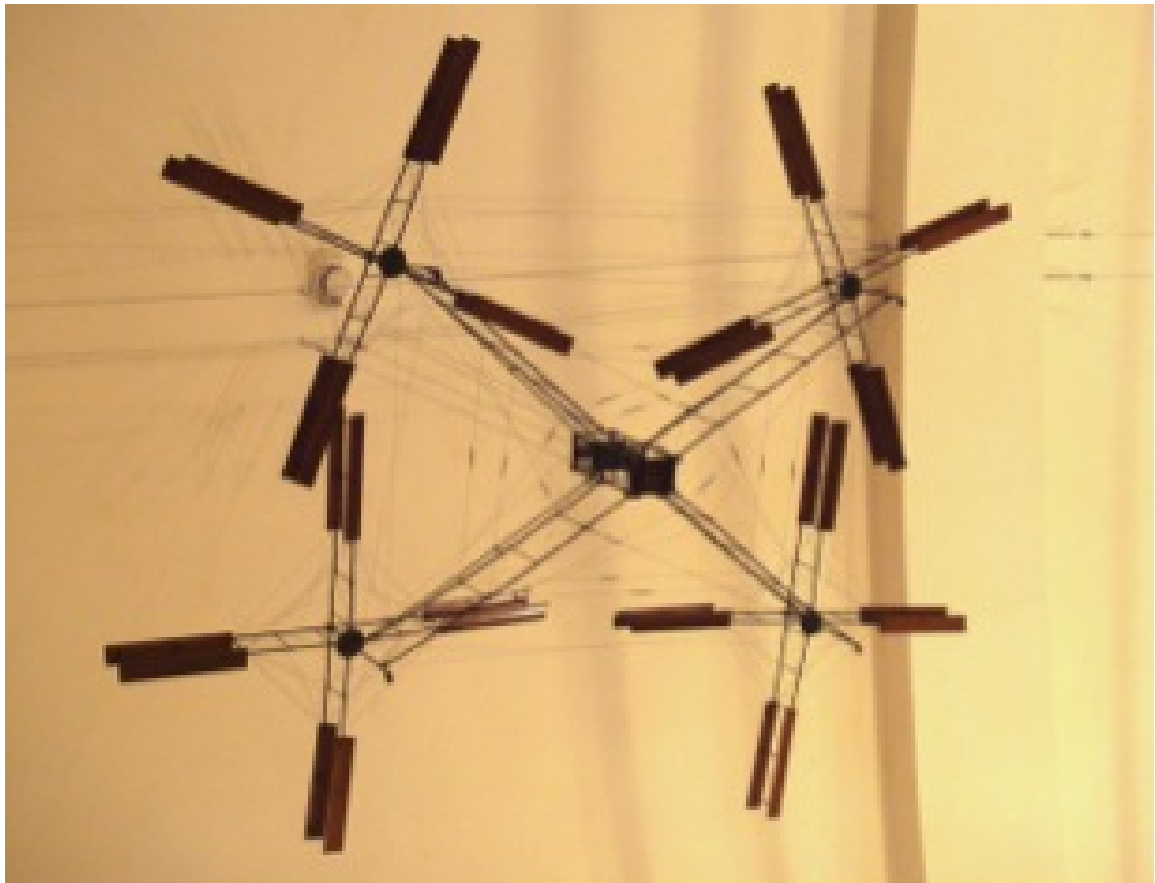


**Figure 1.4:** Louis Berguet Gyroplane No.1

In the same year, Paul Cornu also achieved vertical flight with his twin rotors design (Figure 1.5).



**Figure 1.5:** Paul Cornu Twin Rotor Helicopter

In 1921, the U.S Army undertook its first vertical flight program under the direction of a Russian engineer George de Bothezat. The design as shown in Figure 1.6 is very similar to the modern day Quadrotor with its symmetrically placed rotors on the end of *X* shaped frame. The body consists of a truss structure made up of intersecting beams

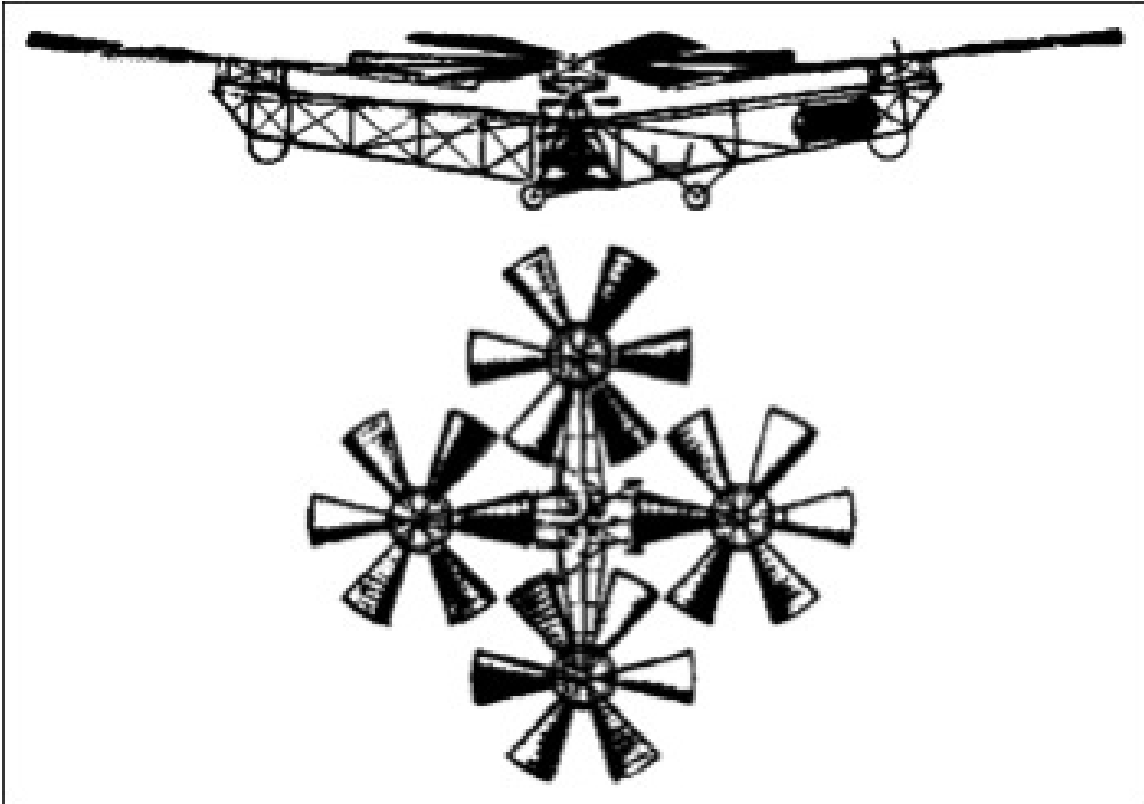


**Figure 1.6:** Bothezat Four Rotor Design

In 1922, Etienne Oehmichen an engineer in France built the first working prototype of the Quadrotor. This machine featured the familiar X design adopted in the modern Quadrotor. Since a single 120HP engine powered all four rotors it was not possible to control the attitude or orientation of the craft by varying the speed for individual rotors. Using four additional small propellers solved this problem.

The design for the Quadrotor existed since 1900. But all of the designs till now lacked a method to control the rotorcraft. It was not until 1956 that the next stage in the Quadrotor development emerged. Convertawingss Model A Quadrotor eliminated the need for the extra four propellers in Oehmichens design and used wings for lift in forward flight. It was powered by two engines and was controlled by varying the power from each engine. This control methodology is now the primary scheme for controlling the modern Quadrotor.



**Figure 1.7:** ConvertaWings's Model A helicopter

## 1.2 Modern Day Quadrotor

Advancements in material sciences led to decreasing the weight of the quadrotor. The development of compact and powerful electric Li-PO batteries also aided in making the aircraft compact and light.

Mesicopter [8] project, at Stanford University aimed at fabricating quadrotors on the scale of 1 to 10 centimeters. This project also discussed the effects of scaling on the structural quality and aerodynamic properties among others.

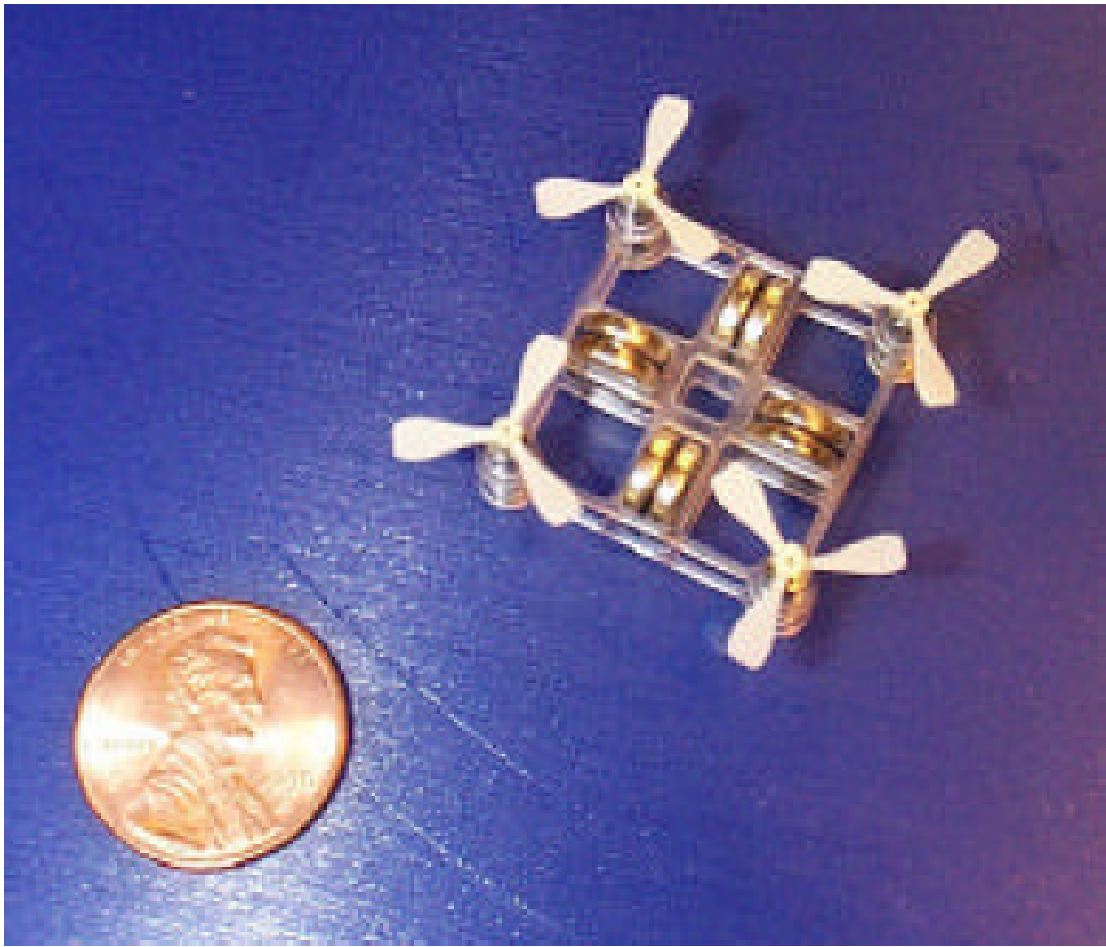


**Figure 1.8:** Mesicopter battery powered prototype

The OS4 project at the Autonomous Systems Laboratory at EPFL focuses on developing micro Vertical Take Off and Landing (VTOL) for the purpose of indoor navigation.

X4 Flyer project Australian National University aimed at developing quadrotors that were rugged and could carry heavier payloads upto 1kg and substantial flight duration [12] .

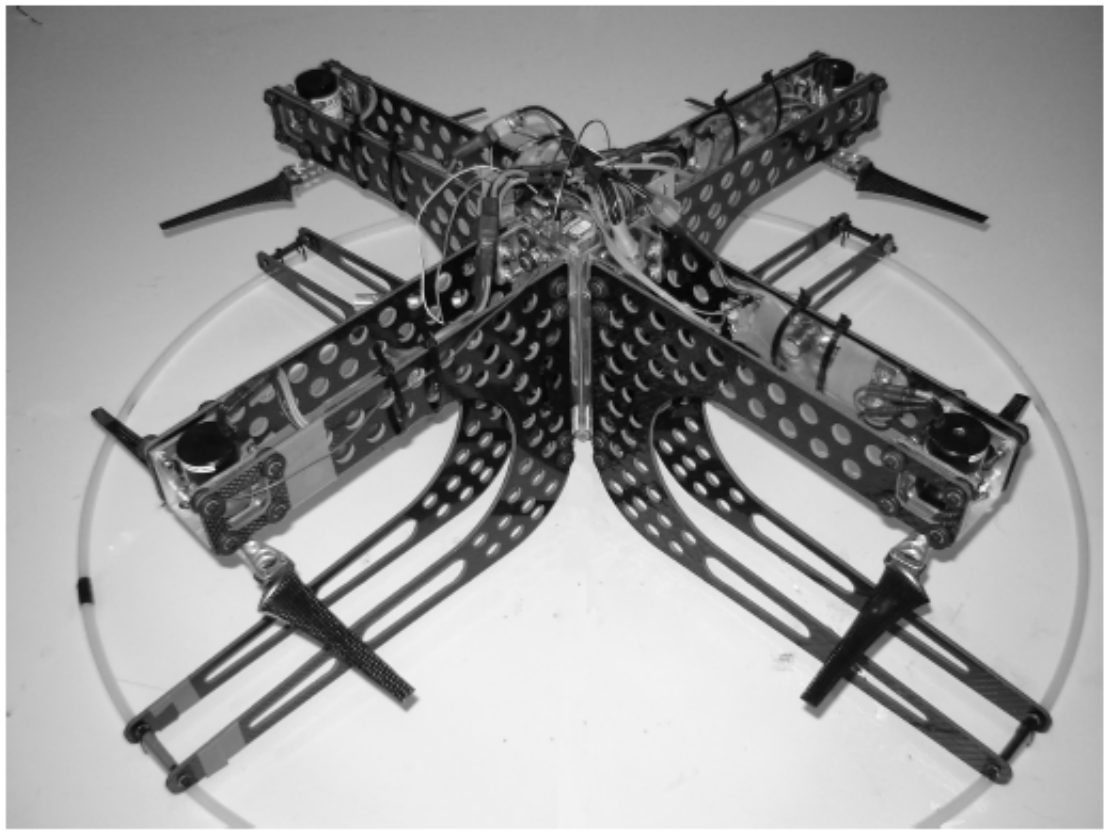


**Figure 1.9:** X4 Flyer Mark II

Another project at Stanford University, Stanford Testbed of Autonomous Rotorcraft for Multi-Agent Control (*STARMAC*) aimed at developing techniques of making multiple quadrotors perform tasks like autonomous collision and obstacle avoidance, formation flight etc.



**Figure 1.10:** STARMAC platform

Another research team at ETH Zurich is working on making quadrotors that perform artistically complex tasks in real time. The figure shows three of the quadrotors in hover at the Flying Machine Arena.



**Figure 1.11:** Quadrotors in hover in the flying Machine Arena

Another team at University of Pennsylvania is working with swarm of nano quadrotors.



**Figure 1.12:** Swarm of Nano Quadrotors

## Chapter 2

### NON-LINEAR MODEL OF THE QUADROTOR

#### 2.1 Introduction

In this chapter, the formulation of *6-DOF* non-linear model is discussed. It will also discuss the ideas of reference frames and their transformations.

#### 2.2 Assumptions

- The aircraft is assumed to be a rigid body.
- The propellers are assumed to be rigid.
- The quadrotor frame is symmetrical.
- Mass center of the quad rotor coincides with the center of the rigid frame.
- The inertia of the motor is assumed to be small and neglected.
- The Earth is assumed to be flat.

#### 2.3 Reference Frames

Before beginning the model development for the quadrotor it is necessary to understand the different reference frames and their co-ordinate transformations. For Unmanned Aerial Systems, two frames of reference are important.

- Inertial reference frame.
- Body fixed frame.

Due to the flat earth assumption, we can take a frame of reference attached to the surface of the earth as the Inertial reference frame since the accelerations of this frame associated with respect to the earth are negligible as compared to the accelerations produced by the aircraft [9].

It is necessary to use different co-ordinate transformations for representing the position and the orientation of the quadrotor due to the following reasons.[1]

- The system inputs and the aerodynamic forces act on the body frame.
- Sensors like gyroscopes, accelerometers measure quantities relative to the body frame. On the other hand GPS measures position with respect to the inertial frame.
- Many of the missions for the UAV like loitering around a particular area, mapping a particular terrain are specified in the inertial frame of reference.

Due to the above reasons, the model development has been carried out in the inertial frame of reference.

## 2.4 Kinematics

The attitude of the quadrotor is represented by  $\phi, \theta, \psi$ .  $\phi$  represents the roll angle of the quadrotor about the inertial x axis.  $\theta$  represents the pitch angle of the quadrotor about the inertial y axis.  $\psi$  represents the yaw angle about the inertial z axis. As shown in [luukkonen2011modelling]. Let  $\xi = [x, y, z]^T$  represent the position of the quadrotor in the inertial frame. Let  $\eta = [\phi, \theta, \psi]^T$  represent the angular position of the quadrotor in the inertial frame. Let  $\nu = [p, q, r]^T$  represent the body angular velocities. Let  $V_B = [v_{xB} v_{yB} v_{zB}]^T$  represent the linear velocities in the body frame.

Also let  $q = [\xi \eta]^T$  represent the linear and angular position vectors.

In aerospace application there are several ways of obtaining the direction cosine matrix to transform the body frame co-ordinates to the inertial co-ordinates by permuting between the *Roll-Pitch-Yaw* angles. The rotation matrix from the earth to the body frame is obtained by performing successively three rotations and in the prescribed order[15].

- Rotate about the z axis *positive Yaw*( $\psi$ ).

$$R_\psi = \begin{bmatrix} \cos(\psi) & \sin(\psi) & 0 \\ -\sin(\psi) & \cos(\psi) & 0 \\ 0 & 0 & 1 \end{bmatrix} \quad (2.1)$$

- Rotate about the new y-axis *positive Pitch*( $\theta$ ).

$$R_\theta = \begin{bmatrix} \cos(\theta) & 0 & -\sin(\theta) \\ 0 & 1 & 0 \\ \sin(\theta) & 0 & \cos(\theta) \end{bmatrix} \quad (2.2)$$

- Rotate about the new x axis *positive Roll*( $\phi$ ).

$$R_\phi = \begin{bmatrix} 1 & 0 & 0 \\ 0 & \cos(\phi) & \sin(\phi) \\ 0 & -\sin(\phi) & \cos(\phi) \end{bmatrix} \quad (2.3)$$

Thus the resulting rotation matrix represent the transformation using the Euler angles  $\psi, \theta, \phi$  from the earth frame to the body frame.

$$\begin{bmatrix} x_{Body} \\ y_{Body} \\ z_{Body} \end{bmatrix} = R_\phi R_\theta R_\psi \begin{bmatrix} x_{Earth} \\ y_{Earth} \\ z_{Earth} \end{bmatrix} \quad (2.4)$$

$$R_{Earth}^{Body} = \begin{bmatrix} \cos(\theta) \cos(\psi) & \cos(\theta) \sin(\psi) & -\sin(\theta) \\ \sin(\phi) \sin(\theta) \cos(\psi) - \cos(\phi) \sin(\psi) & \sin(\phi) \sin(\theta) \sin(\psi) + \cos(\phi) \cos(\psi) & \sin(\phi) \cos(\theta) \\ \cos(\phi) \sin(\theta) \cos(\psi) + \sin(\phi) \sin(\psi) & \cos(\phi) \sin(\theta) \sin(\psi) - \sin(\phi) \cos(\psi) & \cos(\phi) \cos(\theta) \end{bmatrix} \quad (2.5)$$

The above rotation matrix is an orthonormal matrix. Then the transformation to obtain the Earth frame quantities can be obtained by taking the transpose of the equation 2.5.

$$R_{Body}^{Earth} = {R_{Earth}^{Body}}^T \quad (2.6)$$

The resulting matrix is shown below

$$R_{Body}^{Earth} = \begin{bmatrix} \cos(\psi) \cos(\theta) & \cos(\psi) \sin(\theta) \sin(\phi) - \sin(\psi) \cos(\phi) & \cos(\psi) \sin(\theta) \cos(\phi) + \sin(\psi) \sin(\phi) \\ \sin(\psi) \cos(\theta) & \sin(\psi) \sin(\theta) \sin(\phi) + \cos(\psi) \cos(\phi) & \sin(\psi) \sin(\theta) \cos(\phi) - \cos(\psi) \sin(\phi) \\ -\sin(\theta) & \cos(\theta) \sin(\phi) & \cos(\theta) \cos(\phi) \end{bmatrix} \quad (2.7)$$

Thus

$$\begin{bmatrix} x_{Earth} \\ y_{Earth} \\ z_{Earth} \end{bmatrix} = R_{Body}^{Earth} \begin{bmatrix} x_{Body} \\ y_{Body} \\ z_{Body} \end{bmatrix} \quad (2.8)$$

From [5] the Euler rates can be used to determine the attitude of the quadrotor. The relation between the euler rates and the body frame angular velocities is obtained as follows

$$\Omega_{Earth}^{Body} = \dot{\phi} + R_\phi \dot{\theta} + R_\phi R_\theta \dot{\psi} = \Omega \dot{\eta} \quad (2.9)$$

where

$$\Omega = \begin{bmatrix} 1 & 0 & -\sin(\theta) \\ 0 & \cos(\phi) & \sin(\phi) \cos(\theta) \\ 0 & -\sin(\phi) & \cos(\phi) \cos(\theta) \end{bmatrix} \quad (2.10)$$

The Euler rates are obtained from [15] as

$$\begin{bmatrix} \dot{\phi} \\ \dot{\theta} \\ \dot{\psi} \end{bmatrix} = \Omega^{-1} \begin{bmatrix} p \\ q \\ r \end{bmatrix} \quad (2.11)$$

where

$$\Omega^{-1} = \begin{bmatrix} 1 & \tan(\theta) \sin(\phi) & \tan(\theta) \cos(\phi) \\ 0 & \cos(\phi) & -\sin(\phi) \\ 0 & \frac{\sin(\phi)}{\cos(\theta)} & \frac{\cos(\phi)}{\cos(\theta)} \end{bmatrix} \quad (2.12)$$

## 2.5 Dynamics

Quadrotor is an under-actuated system since it has only four control inputs and six degrees of freedom. The figure shows the different control inputs and the frames of reference for a quadrotor [9]

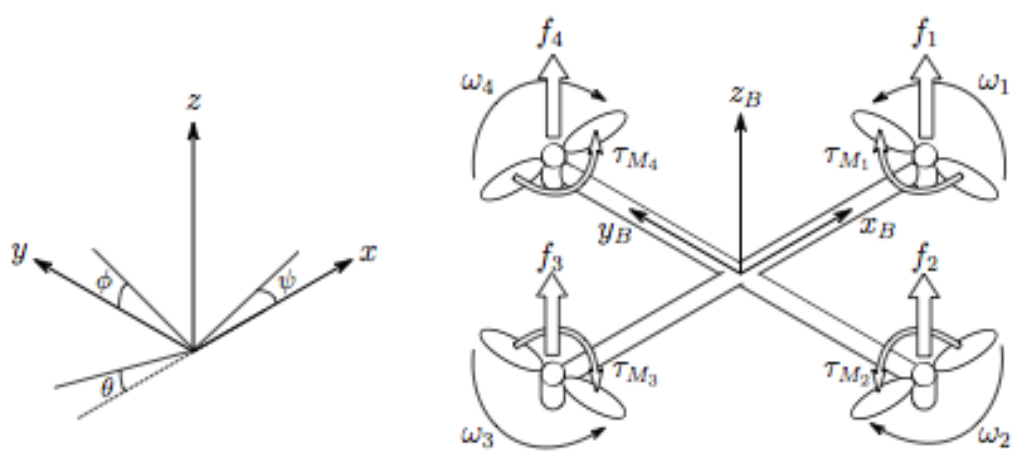


**Figure 2.1:** Inertial and Body reference frame for a Quadrotor

### 2.5.1 Forces

The angular velocity of the rotor  $\omega_i$  produces a force  $f_i$  in the direction of rotor axis.

$$f_i = k\omega_i^2 \quad (2.13)$$

where  $i=1,2,3,4$  where  $k$  is the lift constant of the propeller. The thrust  $\mathbf{T}$  is produced by the combined effect of the forces produced by individual motors in the direction of the body  $z$  axis

$$\mathbf{T} = \sum_{i=1}^4 f_i = k \sum_{i=1}^4 \omega_i^2 \quad (2.14)$$

Then the thrust vector in the body frame is represented by

$$T_B = \begin{bmatrix} 0 \\ 0 \\ T \end{bmatrix} \quad (2.15)$$

### 2.5.2 Moments

The moments are produced by creating a differential thrust across the two motors on the same arm of the quadrotor. The moments provide the input necessary for the quadrotor to move longitudinally or laterally.

- Roll Moment

For moving in the positive yaxis direction the angular velocity of motor#4 (left) and motor#2 (right) are varied2.2.

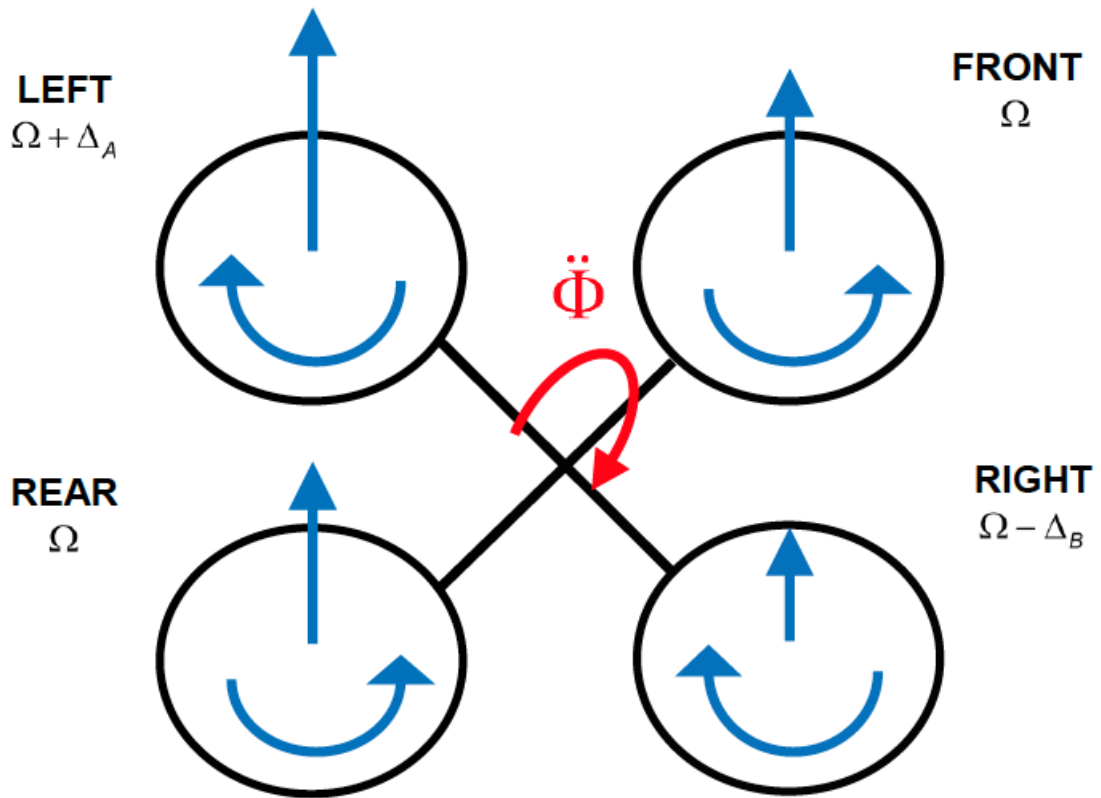


**Figure 2.2:** Roll moment about the earth x axis

The torque required to generate this moment is produced by increasing the angular speed of the motor#4 (left) and decreasing the angular speed of the motor#2 (right) as shown in equation2.16.

$$\tau_\phi = lk(\omega_4^2 - \omega_2^2) \quad (2.16)$$

- Pitch Moment

For moving in the positive x direction, the angular velocity of motor# 3 (Rear motor) is increased and that of motor# 1(Front motor) is decreased by the same amount as shown in the figure2.3

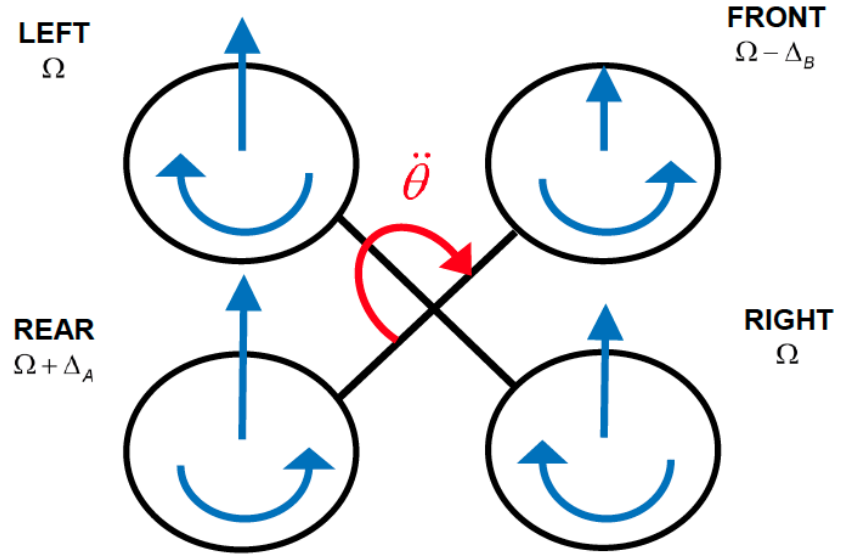


Figure 3-4. Pitch movement

**Figure 2.3:** Pitch moment about the earth y axis

Thus the torque required can be calculated from the equation??

$$\tau_\theta = lk(\omega_3^2 - \omega_1^2) \quad (2.17)$$

- Yaw Moment

For making the quadrotor yaw to a particular orientation the angular velocities of a set of opposite rotors are varied simultaneously and by the same amount. For producing a positive yaw the angular velocities of the motor #1 and motor #3 are increased while that of motor #2 and motor #4 are decreased by the same amount as shown in the figure 2.4

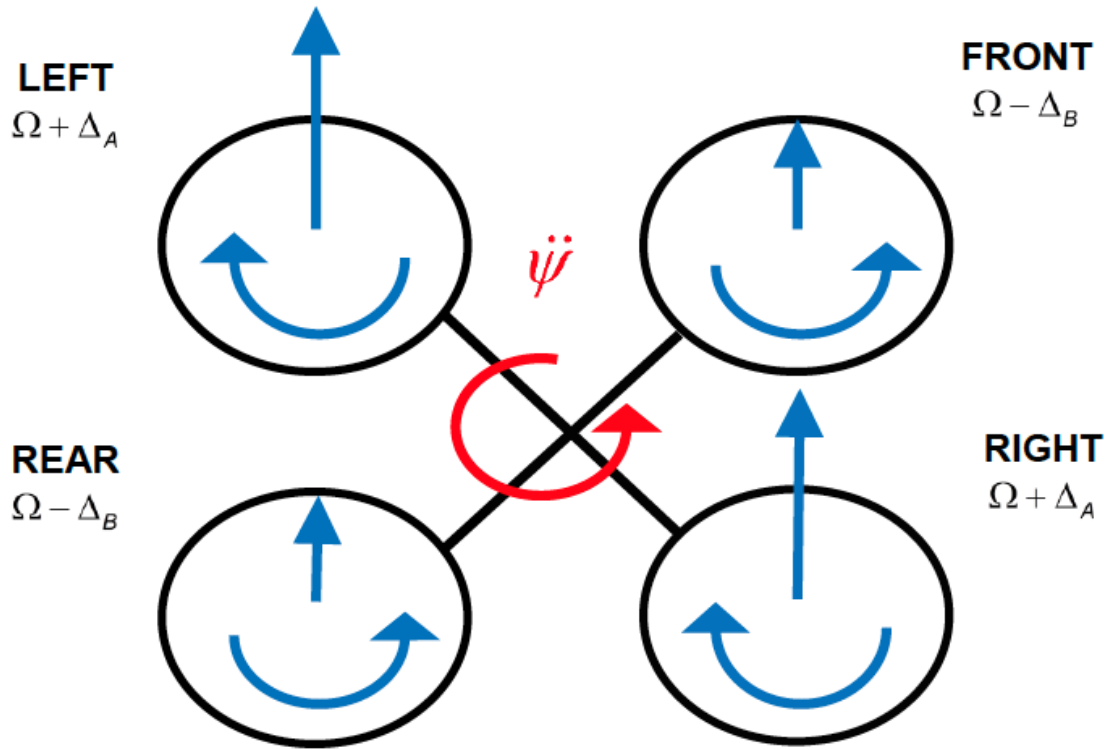


**Figure 2.4:** Yaw movement about the earth z axis

The torque required to produce this yaw movement is given by equation 2.18

$$\tau_\psi = b(\omega_1^2 + \omega_3^2 - \omega_2^2 - \omega_4^2) \quad (2.18)$$

### 2.5.3 Moment of Inertia

The quadrotor is a symmetric structure with the four arms aligned with the body x and y axes. From [9] the inertia matrix is diagonal with  $I_{xx} = I_{yy}$ . The inertia matrix is given by

$$I = \begin{bmatrix} I_{xx} & 0 & 0 \\ 0 & I_{yy} & 0 \\ 0 & 0 & I_{zz} \end{bmatrix} \quad (2.19)$$

The Moment of Inertia for the quadrotor are calculated assuming a spherical mass  $M_s$  at the center or radius  $R$  and point masses  $m_m$  at the end of the arms at a distance of  $l$  from the mass center [1].

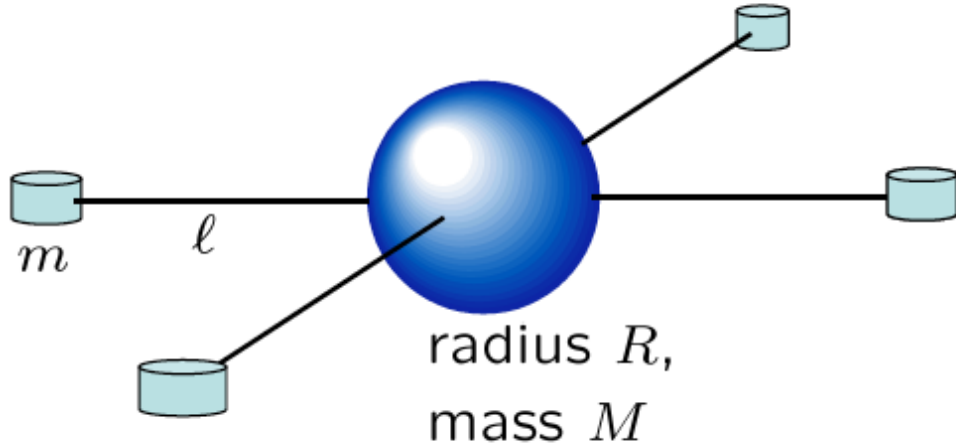


**Figure 2.5:** Schematic for inertia calculation

The moment of Inertia along the body x-axis, y-axis, z-axis are calculated as follows

$$I_{xx} = \frac{2MR^2}{5} + 2ml^2 \quad (2.20)$$

$$I_{yy} = \frac{2MR^2}{5} + 2ml^2 \quad (2.21)$$

$$I_{zz} = \frac{2MR^2}{5} + 4ml^2 \quad (2.22)$$

where  $m$  is the mass of the motor and  $M$  is the mass of the sphere.

### 2.5.4 Newton-Euler equations

Since the quadrotor is assumed to be rigid From [9] ,Newton-Euler equations can be used to represent its dynamics. In the body frame the force required for acceleration of the mass is given by Equation2.23

$$m\dot{V}_B + \nu \times (m\dot{V}_B) = R^T G + T_B \quad (2.23)$$

In the inertial frame the equation becomes

$$m\ddot{\xi} = G + R^T T_B \quad (2.24)$$

Thus

$$\begin{bmatrix} \dot{x} \\ \dot{y} \\ \dot{z} \end{bmatrix} = -g \begin{bmatrix} 0 \\ 0 \\ 1 \end{bmatrix} + \frac{T}{m} \begin{bmatrix} \cos(\psi) \sin(\theta) \cos(\phi) + \sin(\psi) \sin(\phi) \\ \sin(\psi) \sin(\theta) \cos(\phi) - \cos(\psi) \sin(\phi) \\ \cos(\theta) \cos(\phi) \end{bmatrix} \quad (2.25)$$

The angular accelerations in the inertial frame are obtained from the body frame by using 2.12 and its time derivative

$$\ddot{\eta} = \frac{d}{dt} (\Omega^{-1}) \nu + \Omega^{-1} \dot{\nu} \quad (2.26)$$

### 2.5.5 Euler-Lagrange Equations

The Lagrangian  $\mathcal{L}$  is obtained from the addition of the translational energy  $E_{trans}$  and the rotational energy  $E_{rot}$  and subtracting the potential energy  $E_{pot}$  of the system.

$$\mathcal{L}(q, \dot{q}) = E_{trans} + E_{rot} - E_{pot} \quad (2.27)$$

From [4], we see that the Euler Lagrange equations with external forces and torques is given by

$$\begin{bmatrix} f \\ \tau \end{bmatrix} = \frac{d}{dt} \frac{\partial \mathcal{L}}{\partial \dot{q}} - \frac{\partial \mathcal{L}}{\partial q} \quad (2.28)$$

From [9],[13] the translational and the rotational components are independent of each other and thus can be studied separately.

The translational Euler-Lagrange equations are given by

$$f = RT_B = m\ddot{\xi} + mg \begin{bmatrix} 0 \\ 0 \\ 1 \end{bmatrix} \quad (2.29)$$

The moment of inertia in the inertial frame is obtained from [13], [9] , [4]

$$\mathbf{J} = \Omega^T I \Omega \quad (2.30)$$

$$= \begin{bmatrix} I_{xx} & 0 & -I_{xx} \sin(\theta) \\ 0 & I_{yy} \cos(\phi)^2 + I_{zz} \sin(\phi)^2 & (I_{yy} - I_{zz}) \cos(\phi) \sin(\phi) \cos(\theta) \\ -I_{xx} \sin(\theta) & (I_{yy} - I_{zz}) \cos(\phi) \sin(\phi) \cos(\theta) & I_{xx} \sin(\theta)^2 + I_{yy} \sin(\phi)^2 \cos(\theta)^2 + I_{zz} \cos(\phi)^2 \cos(\theta)^2 \end{bmatrix} \quad (2.31)$$

Then the rotational energy is given by [9],[13],[4] and Equation (2.31), (2.30)

$$E_{rot} = \frac{1}{2}\nu^T I \nu = \frac{1}{2}\dot{\eta}^T J \dot{\eta} \quad (2.32)$$

The Euler-Lagrange equation for the angular motion is given by

$$\tau = \tau_b = \mathbf{J}\ddot{\eta} + \frac{d}{dt}(\mathbf{J})\dot{\eta} - \frac{1}{2}\frac{\partial}{\partial \eta}(\dot{\eta}^T J \dot{\eta}) = \mathbf{J}\ddot{\eta} + \mathbf{C}(\eta, \dot{\eta})\dot{\eta} \quad (2.33)$$

where  $\mathbf{C}(\eta, \dot{\eta})$  is the Coriolis term that accounts for the gyroscopic and the centripetal terms. Now

$$\mathbf{C}(\eta, \dot{\eta}) = \begin{bmatrix} C_{11} & C_{12} & C_{13} \\ C_{21} & C_{22} & C_{23} \\ C_{31} & C_{32} & C_{33} \end{bmatrix} \quad (2.34)$$

From [9], [13]

$$C11 = 0 \quad (2.35)$$

$$\begin{aligned} C12 &= (I_{yy} - I_{zz})(\dot{\theta} \cos(\phi) \sin(\phi) + \dot{\psi} \sin(\phi)^2 \cos(\theta)) + (I_{zz} - I_{yy})\dot{\psi} \cos(\phi)^2 \cos(\theta) \\ &- I_{xx}\dot{\psi} \cos(\theta) \end{aligned} \quad (2.36)$$

$$C13 = (I_{zz} - I_{yy})\dot{\psi} \cos(\phi) \sin(\phi) \cos(\theta)^2 \quad (2.37)$$

$$\begin{aligned} C21 &= (I_{zz} - I_{yy})(\dot{\theta} \cos(\phi) \sin(\phi) + \dot{\psi} \sin(\phi)^2 \cos(\theta)) + (I_{yy} - I_{zz})\dot{\psi} \cos(\phi)^2 \cos(\theta) \\ &+ I_{xx}\dot{\psi} \cos(\theta) \end{aligned} \quad (2.38)$$

$$C22 = (I_{zz} - I_{yy})\dot{\phi} \cos(\phi) \sin(\phi) \quad (2.39)$$

$$\begin{aligned} C23 &= -I_{xx}\dot{\psi} \sin(\theta) \cos(\theta) + I_{yy}\dot{\psi} \sin(\phi)^2 \cos(\theta) \sin(\theta) \\ &+ I_{zz}\dot{\psi} \cos(\phi)^2 \sin(\theta) \cos(\theta) \end{aligned} \quad (2.40)$$

$$C31 = (I_{yy} - I_{zz})\dot{\psi} \cos(\theta)^2 \sin(\phi) \cos(\phi) - I_{xx}\dot{\theta} \cos(\theta) \quad (2.41)$$

$$\begin{aligned} C32 &= (I_{zz} - I_{yy})(\dot{\theta} \cos(\phi) \sin(\phi) \sin(\theta) + \dot{\phi} \sin(\phi)^2 \cos(\theta)) \\ &+ (I_{yy} - I_{zz})\dot{\phi} \cos(\phi)^2 \cos(\theta) + I_{xx}\dot{\psi} \sin(\theta) \cos(\theta) - I_{yy}\dot{\psi} \sin(\phi)^2 \sin(\theta) \cos(\theta) \\ &- I_{zz}\dot{\psi} \cos(\phi)^2 \sin(\theta) \cos(\theta) \end{aligned} \quad (2.42)$$

$$\begin{aligned} C33 &= (I_{yy} - I_{zz})\dot{\phi} \cos(\phi) \sin(\phi) \cos(\theta)^2 - I_{yy}\dot{\theta} \sin(\phi)^2 \cos(\theta) \sin(\theta) \\ &- I_{zz}\dot{\theta} \cos(\phi)^2 \cos(\theta) \sin(\theta) + I_{xx}\dot{\theta} \cos(\theta) \sin(\theta) \end{aligned} \quad (2.43)$$

From equation 2.33 we obtain the equations of motion for the angular component.

$$\ddot{\eta} = \mathbf{J}^{-1}(\tau_B - \mathbf{C}(\eta, \dot{\eta})\dot{\eta}) \quad (2.44)$$

To account for the aerodynamic resistance[9],[2], [16] the parameters  $A_x$ ,  $A_y$ ,  $A_z$  are added as the drag coefficients in the form of a diagonal matrix to the translational

velocities eqn2.29 Then the Equation2.25 become

$$\begin{bmatrix} \ddot{x} \\ \ddot{y} \\ \ddot{z} \end{bmatrix} = -g \begin{bmatrix} 0 \\ 0 \\ 1 \end{bmatrix} + \frac{T}{m} \begin{bmatrix} \cos(\psi) \sin(\theta) \cos(\phi) + \sin(\psi) \sin(\phi) \\ \sin(\psi) \sin(\theta) \cos(\phi) - \cos(\psi) \sin(\phi) \\ \cos(\theta) \cos(\phi) \end{bmatrix} - \frac{1}{m} \begin{bmatrix} A_x & 0 & 0 \\ 0 & A_y & 0 \\ 0 & 0 & A_z \end{bmatrix} \begin{bmatrix} \dot{x} \\ \dot{y} \\ \dot{z} \end{bmatrix} \quad (2.45)$$

Other aerodynamic effects also affect the system like blade flapping, non zero angle of attack for the propeller etc. These effects have been studied in [6], and [7]. Some of these effects impact only at high velocities and aggressive maneuvers. For the purpose of this research their impact is assumed to be negligible and the effects are not modeled.

## 2.6 Summary and Conclusions

This chapter described the procedure to obtain the dynamic nonlinear model of the system using EulerLagrange approach. It stated the assumptions for developing the model. It also discussed the different frames of reference and their transformation. The succeeding chapter will talk about deriving linear system models.

## Chapter 3

### LINEAR MODELS

#### 3.1 Introduction

In the previous chapter, 6-DOF nonlinear model was obtained. This chapter will discuss linearisation and obtain linear models for different flight conditions.

#### 3.2 Linearisation

A non-linear system of equations can be symbolically be represented by

$$\dot{X} = f(X, U) \quad (3.1)$$

where  $X$  represents the state vector and  $U$  represents the control or the input vector.  $f$  is a nonlinear function of state and control variables. This equation summarizes the non-linear coupled differential equations obtained from chapter 1.

Let  $\dot{X} = 0$  Then

$$f(X_{eq}, U_{eq}) = 0 \quad (3.2)$$

where  $X_{eq}$  and  $U_{eq}$  are the solutions of  $f$  that satisfy the above equation. These are also called as the *equilibrium values*. Stationary flight implies that the net forces and moments acting on the body of the aircraft are zero. Thus, translational and angular accelerations are also zero. Then the solutions of variables that satisfy stationary flight condition are called as the *trim values* or *equilibrium values*. The resulting linear equation can be represented in the state space form as

$$\delta \dot{X} = A\delta X + B\delta U \quad (3.3)$$

where A is called as the characteristic matrix and B is called as the input matrix which are defined as

$$A := \frac{\partial f}{\partial X} \Big|_{X=X_{eq}, U=U_{eq}} \quad (3.4)$$

$$B := \frac{\partial f}{\partial U} \Big|_{X=X_{eq}, U=U_{eq}} \quad (3.5)$$

The state vector  $\mathbf{X}$  consists of  $\eta, \dot{\eta}, \xi, \dot{\xi}$  as follows  $[x, \dot{x}, y, \dot{y}, z, \dot{z}, \phi, \dot{\phi}, \theta, \dot{\theta}, \psi, \dot{\psi}]$

The input vector  $\mathbf{U}$  consists of system inputs as follows  $[T, \tau_\phi, \tau_\theta, \tau_\psi]$

The characteristic matrix consists of the stability derivatives of the aircraft which are represented in the Equation3.6

$$A = \left[ \begin{array}{cccccccccc} 0 & 1 & 0 & 0 & 0 & 0 & 0 & 0 & 0 & 0 \\ 0 & 0 & & & & & & & & \\ 0 & X_{\dot{x}} & 0 & 0 & 0 & 0 & X_{\phi} & 0 & X_{\theta} & 0 \\ X_{\psi} & 0 & & & & & & & & \\ 0 & 0 & 0 & 1 & 0 & 0 & 0 & 0 & 0 & 0 \\ 0 & 0 & & & & & & & & \\ 0 & 0 & 0 & Y_{\dot{y}} & 0 & 0 & Y_{\phi} & 0 & Y_{\theta} & 0 \\ Y_{\psi} & 0 & & & & & & & & \\ 0 & 0 & 0 & 0 & 0 & 1 & 0 & 0 & 0 & 0 \\ 0 & 0 & & & & & & & & \\ 0 & 0 & 0 & 0 & 0 & Z_{\dot{z}} & Z_{\phi} & 0 & Z_{\theta} & 0 \\ Z_{\psi} & 0 & & & & & & & & \\ 0 & 0 & 0 & 0 & 0 & 0 & 0 & 0 & 1 & 0 \\ 0 & 0 & & & & & & & & \\ 0 & 0 & 0 & 0 & 0 & 0 & \Phi_{\phi} & \Phi_{\dot{\phi}} & \Phi_{\theta} & \Phi_{\dot{\theta}} \\ \Phi_{\psi} & \Phi_{\dot{\psi}} & & & & & & & & \\ 0 & 0 & 0 & 0 & 0 & 0 & 0 & 0 & 0 & 1 \\ 0 & 0 & & & & & & & & \\ 0 & 0 & 0 & 0 & 0 & 0 & \Theta_{\phi} & \Theta_{\dot{\phi}} & \Theta_{\theta} & \Theta_{\dot{\theta}} \\ \Theta_{\psi} & \Theta_{\dot{\psi}} & & & & & & & & \\ 0 & 0 & 0 & 0 & 0 & 0 & 0 & 0 & 0 & 0 \\ 0 & 1 & & & & & & & & \\ 0 & 0 & 0 & 0 & 0 & 0 & \Psi_{\phi} & \Psi_{\dot{\phi}} & \Psi_{\theta} & \Psi_{\dot{\theta}} \\ \Psi_{\psi} & \Psi_{\dot{\psi}} & & & & & & & & \end{array} \right] \quad (3.6)$$

The input matrix consists of the control derivatives of the aircraft which can be represented by Equation 3.7

$$B = \begin{bmatrix} 0 & 0 & 0 & 0 \\ X_T & 0 & 0 & 0 \\ 0 & 0 & 0 & 0 \\ Y_T & 0 & 0 & 0 \\ 0 & 0 & 0 & 0 \\ Z_T & 0 & 0 & 0 \\ 0 & 0 & 0 & 0 \\ 0 & \Phi_{\tau_\phi} & \Phi_{\tau_\theta} & \Phi_{\tau_\psi} \\ 0 & 0 & 0 & 0 \\ 0 & \Theta_{\tau_\phi} & \Theta_{\tau_\theta} & \Theta_{\tau_\psi} \\ 0 & 0 & 0 & 0 \\ 0 & \Psi_{\tau_\phi} & \Psi_{\tau_\theta} & \Psi_{\tau_\psi} \end{bmatrix} \quad (3.7)$$

### 3.3 Longitudinal Models

The longitudinal motion is constituted by forward velocity caused by the pitch angle ( $\theta$ ) produced by the moment ( $\tau_\theta$ ) and vertical velocity ( $\dot{z}$ ) produced by thrust (T)

The state space representation for the longitudinal motion is as follows.

$$\dot{X}_{Long} = A_{Long}X_{Long} + B_{Long}U_{Long} \quad (3.8)$$

where

$$A_{Long} = \begin{bmatrix} Z_z & 0 & Z_\theta & 0 \\ 0 & X_{\dot{x}} & X_\theta & 0 \\ 0 & 0 & 0 & 1 \\ 0 & 0 & \Theta_\theta & \Theta_{\dot{\theta}} \end{bmatrix} \quad (3.9)$$

$$B_{Long} = \begin{bmatrix} Z_T & 0 \\ X_T & 0 \\ 0 & 0 \\ 0 & \Theta_{\tau_\theta} \end{bmatrix} \quad (3.10)$$

$$X_{long} = \begin{bmatrix} \dot{z} \\ \dot{x} \\ \theta \\ \dot{\theta} \end{bmatrix}^T \quad (3.11)$$

$$U_{Long} = \begin{bmatrix} T \\ \tau_\theta \end{bmatrix}^T \quad (3.12)$$

The nominal parameters for the system are chosen from [9].

### 3.4 Impact of flight condition

#### 3.4.1 Vertical Flight

The analytic expression for thrust for the vertical flight condition when  $X_{dot}=0$  is given by

$$T_{eq} = mg + A_z \dot{z}_{eq} \quad (3.13)$$

Parameter	Value	Unit
$m$	0.468	kg
$I_{xx}$	4.856e-3	kg.m <sup>2</sup>
$I_{yy}$	4.856e-3	kg.m <sup>2</sup>
$I_{zz}$	8.801e-3	kg.m <sup>2</sup>
$A_x$	0.25	
$A_y$	0.25	
$A_z$	0.25	
g	9.81	m/sec <sup>2</sup>
l	0.225	m

**Table 3.1:** Nominal Parameters

The Figure(3.1) shows the dependency of Thrust with the flight condition both numerically and analytically.

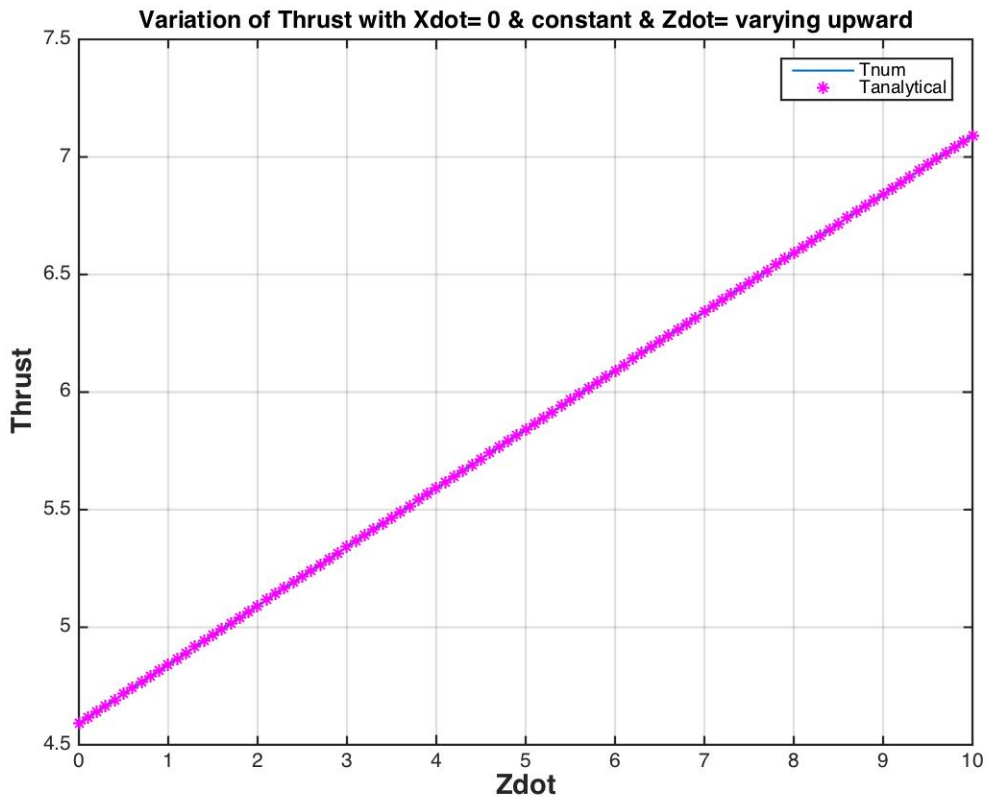


**Figure 3.1:** Variation of Thrust with flight condition

The variation of  $\tau_\theta$  with flight condition is shown in the following figure.

For moving vertically, the plant transfer function gets decoupled and we obtain a diagonal 2X2 matrix as shown in Eqn(3.14)

$$\begin{bmatrix} \frac{g_{11}}{s+a} & 0 \\ 0 & \frac{g_{22}}{s^2(s+a)} \end{bmatrix} \quad (3.14)$$

The analytic expression for gain(1,1) obtained by the equilibrium analysis is as follows.

$$g_{11} = \frac{1}{m} \left[ \frac{mg + A_z \dot{z}_{eq}}{mg + A_z \dot{z}_{eq}} \right] = \frac{1}{m} \quad (3.15)$$

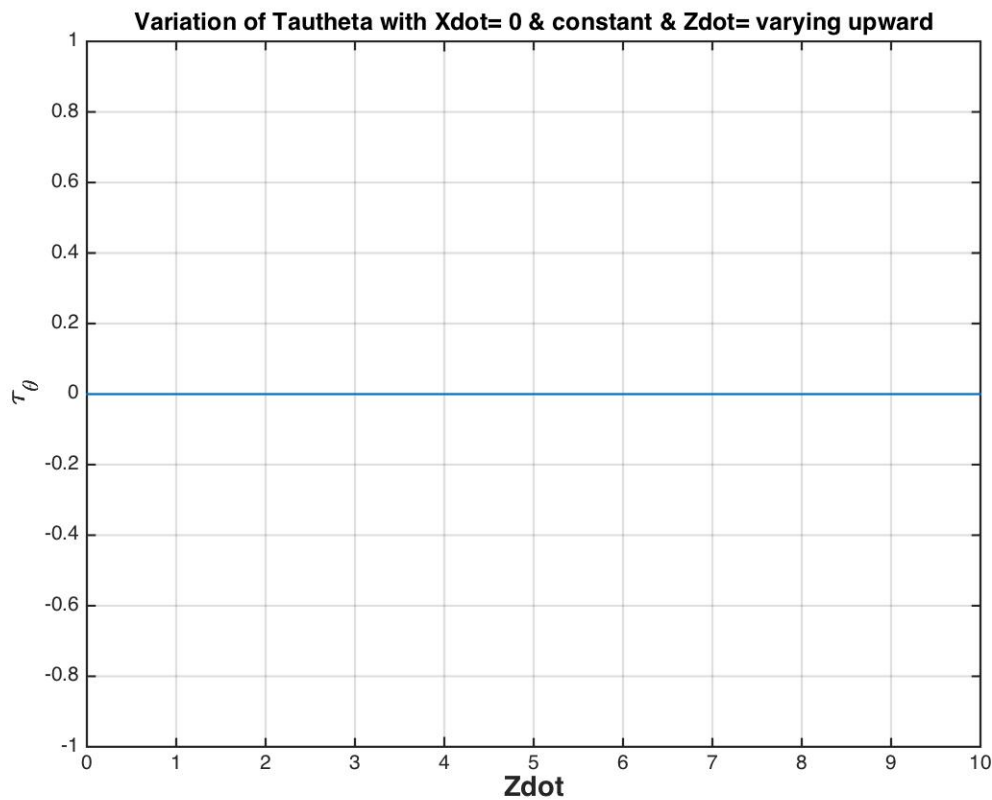


**Figure 3.2:** Variation of Tautheta with flight condition

The Figure(3.3) validates the eqn(3.15)

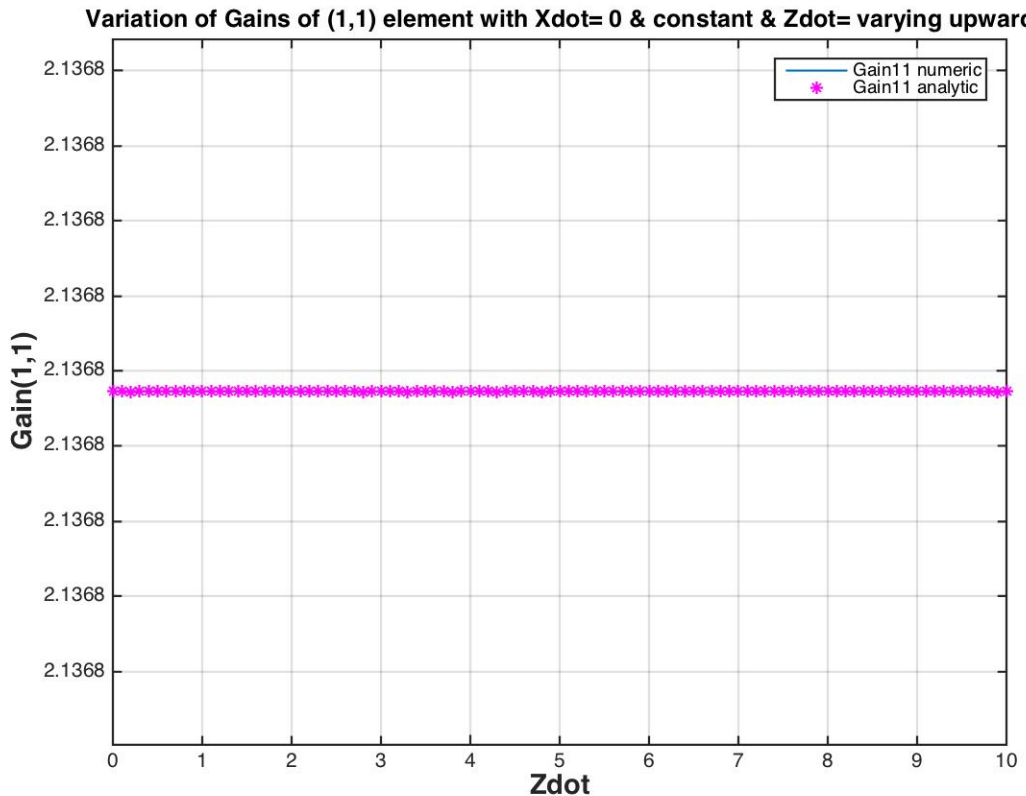


**Figure 3.3:** Gain(1,1) element variation with flight condition

Similarly, the analytic expression for gain(2,2) obtained by equilibrium analysis is described in Eqn(3.16)

$$g_{22} = \frac{mg + A_z z_{eq}}{mI_{yy}} \quad (3.16)$$

Figure(3.4) shows the validation with numeric computation.

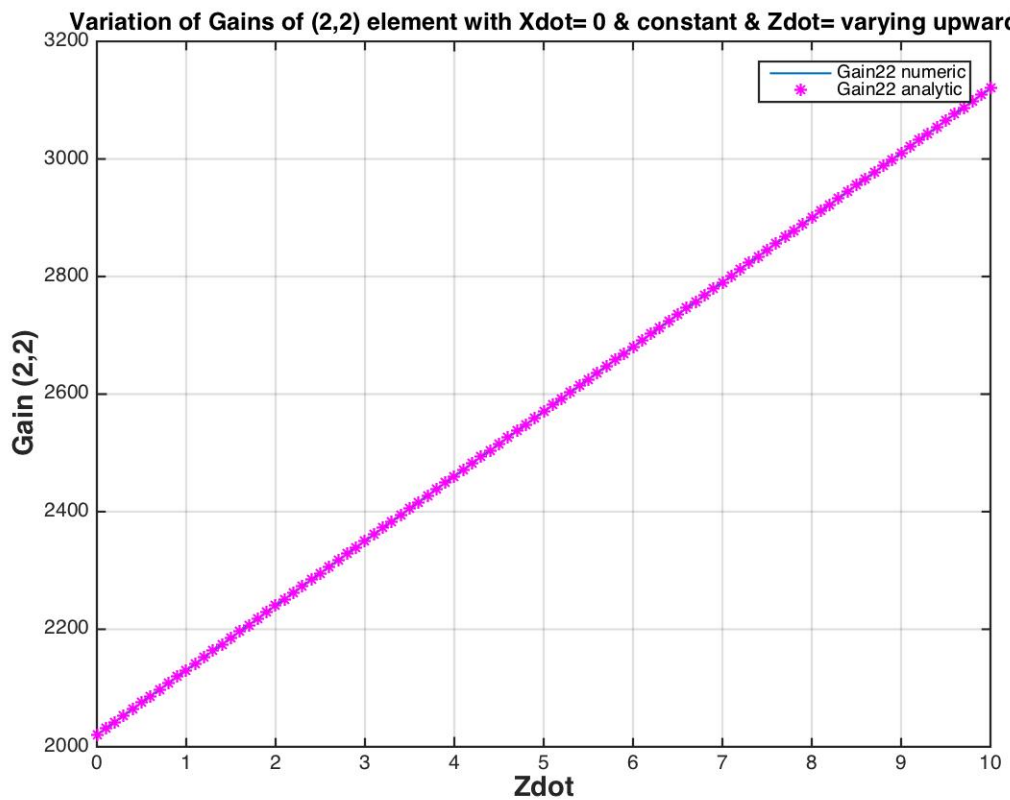


**Figure 3.4:** Gain(2,2) variation with flight condition

### Bode Plots

This section discusses the frequency response of the plant for the vertical flight condition.

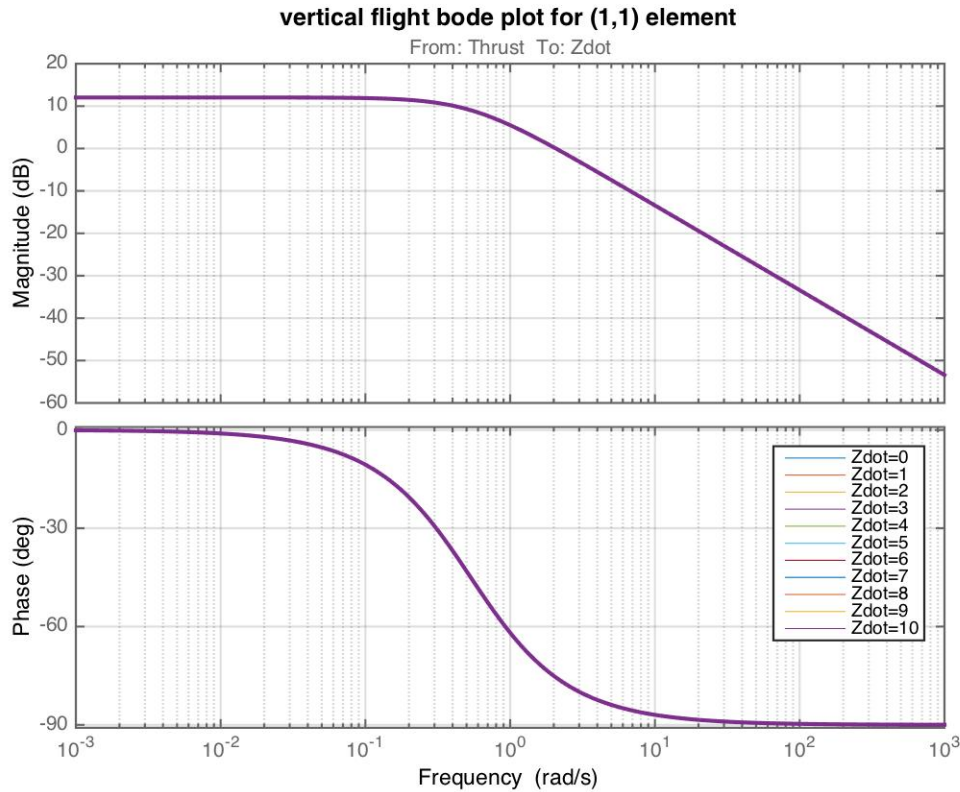


**Figure 3.5:** Frequency Response magnitude and phase plot for element (1,1) for vertical flight condition

Figure(3.5) shows the frequency response for the transfer function from  $\dot{z}$  to Thrust for the vertically climbing condition.

- From the magnitude plot we see that at low frequencies the magnitude remains constant at about  $\approx 12$ dB for all vertical climb flight conditions and decreases with a slope of  $-20$ dB/dec for higher frequencies.
- From the phase plot we see that low frequencies the phase remains at  $0^\circ$  and decreases to  $-90^\circ$  at high frequencies.

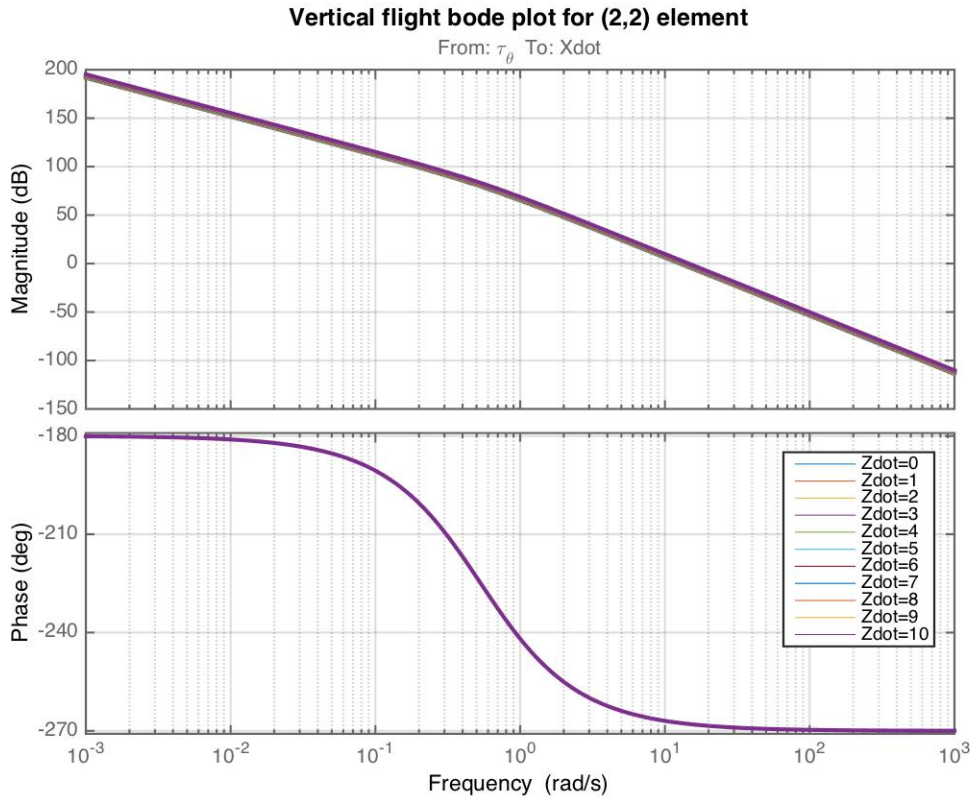


**Figure 3.6:** Frequency Response magnitude and phase plot for element(2,2) for vertical flight condition

Figure(3.6) shows the frequency response for the transfer function from  $\dot{x}$  to  $\tau_\theta$ .

- From the magnitude plot we see that, at low frequencies the magnitude is large because of the presence of two integrators and decreases with a slope of -40dB/dec. At high frequencies, the magnitude continues to decrease with a slope of -60dB/dec.
- From the phase plot we see that, at low frequencies the phase is  $-180^\circ$  because of the negative gain as seen from Fig(3.16) and it becomes  $-270^\circ$  at high frequencies.

### 3.4.2 Forward Flight

For the longitudinal mode, the plant  $P(s)$  is a 2x2 transfer function matrix with inputs 1 and 2 as  $T$  and  $\tau_\theta$  and outputs 1 and 2 as  $\dot{z}$  and  $\dot{x}$  respectively.

$$P(s) = \begin{bmatrix} \frac{g_{11}}{s+a} & \frac{g_{12}}{s^2(s+a)} \\ \frac{g_{21}}{s+a} & \frac{g_{22}}{s^2(s+a)} \end{bmatrix} \quad (3.17)$$

The value of the pole at  $s = -a$  depends upon only the drag coefficients and the mass in x and z direction. They have been modeled as constant and equal to one another, i.e.

$$a = \frac{A_x}{m} = \frac{A_z}{m} \quad (3.18)$$

The dependency of equilibrium Thrust  $T$  on the forward flight condition with  $\dot{z} = 0$  is expressed in Eqn(3.19).

$$T_{eq} = \sqrt{(A_x \dot{x}_{eq})^2 + (mg)^2} \quad (3.19)$$

The Figure(3.7) shows the validation of the numeric and the analytic solutions for Thrust

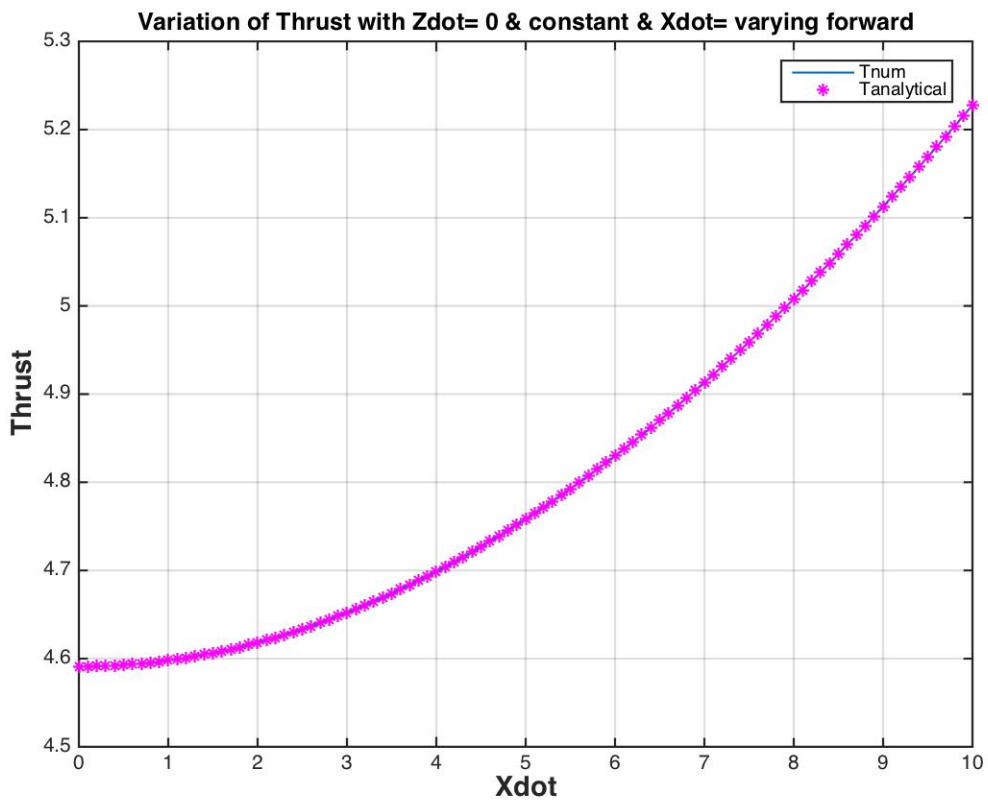


**Figure 3.7:** Analytical and numeric validation of Thrust

Figure(3.8) shows the dependency of equilibrium  $\tau_\theta$  on forward flight condition.

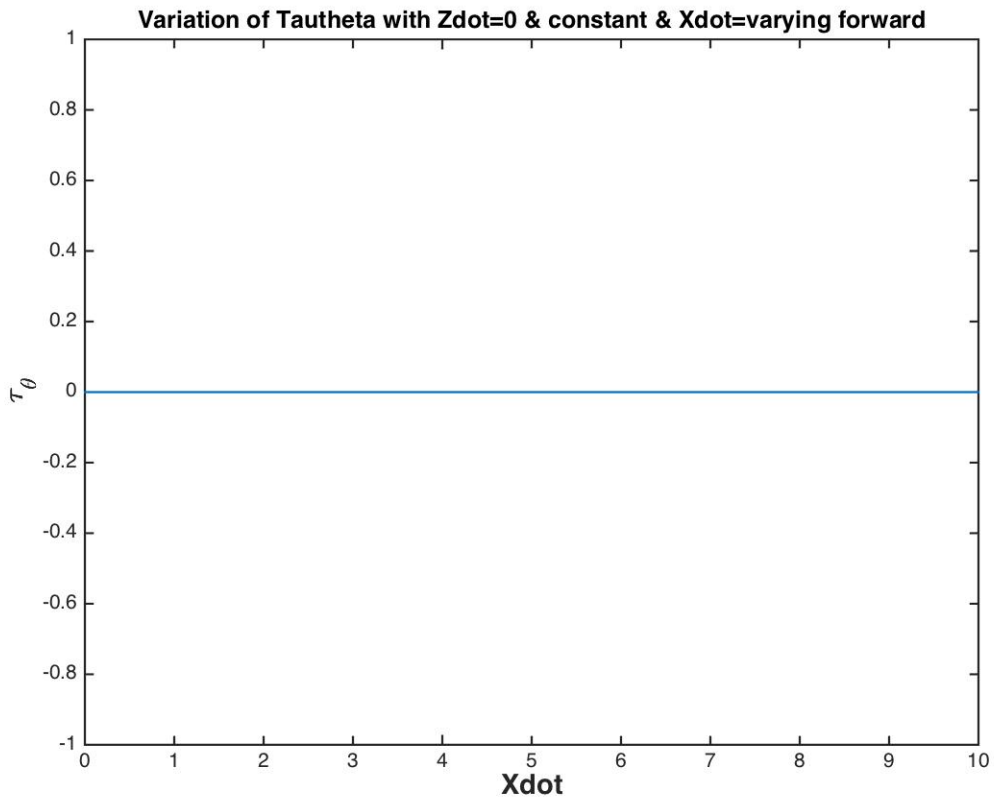


**Figure 3.8:**  $\tau_\theta$  variation with forward flight

The dependency of the plant transfer function gains on the forward flight condition is as follows

$$g_{11} = \text{gain}(1, 1) = \frac{g}{\sqrt{(A_x \dot{x}_{eq})^2 + (mg)^2}} \quad (3.20)$$

The Figure(3.9) illustrates the validation of the analytic and the numeric solutions.

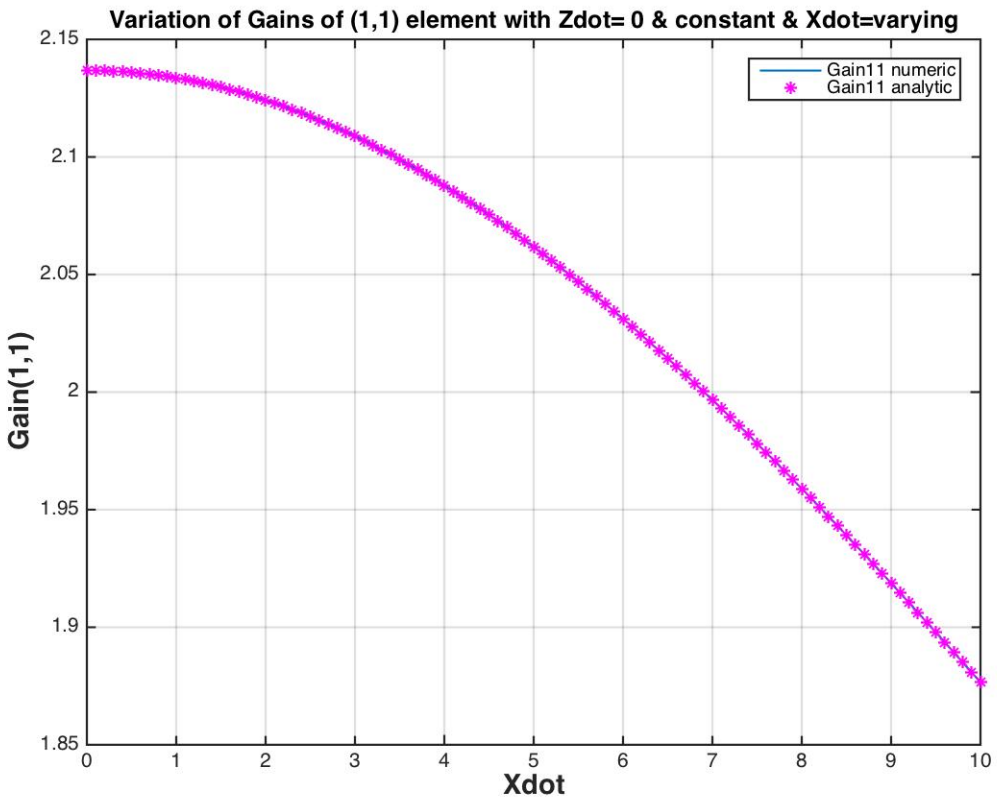


**Figure 3.9:** Comparison of Gain(1,1) analytic and numeric

$$g_{12} = \text{gain}(1, 2) = -\frac{A_x}{mI_{yy}} \dot{x}_{eq} \quad (3.21)$$

The dependency of gain (1,2) element with forward flight condition and its numeric validation is illustrated in Figure(3.10).



**Figure 3.10:** Comparison of Gain(1,2) analytic and numeric

$$g_{21} = \text{gain}(2, 1) = \frac{\frac{A_x \dot{x}_{eq}}{m}}{\sqrt{(A_x \dot{x}_{eq})^2 + (mg)^2}} \quad (3.22)$$



**Figure 3.11:** Comparison of Gain(2,1) analytic and numeric

Figure(3.11) shows the dependency of gain(2,1) on the forward flight condition and its numeric validation.

$$g_{22} = \text{gain}(2, 2) = \frac{g}{I_{yy}} \quad (3.23)$$

Figure(3.12) shows the dependency of gain(2,2) on forward flight condition and its numeric validation with the analytic solution.

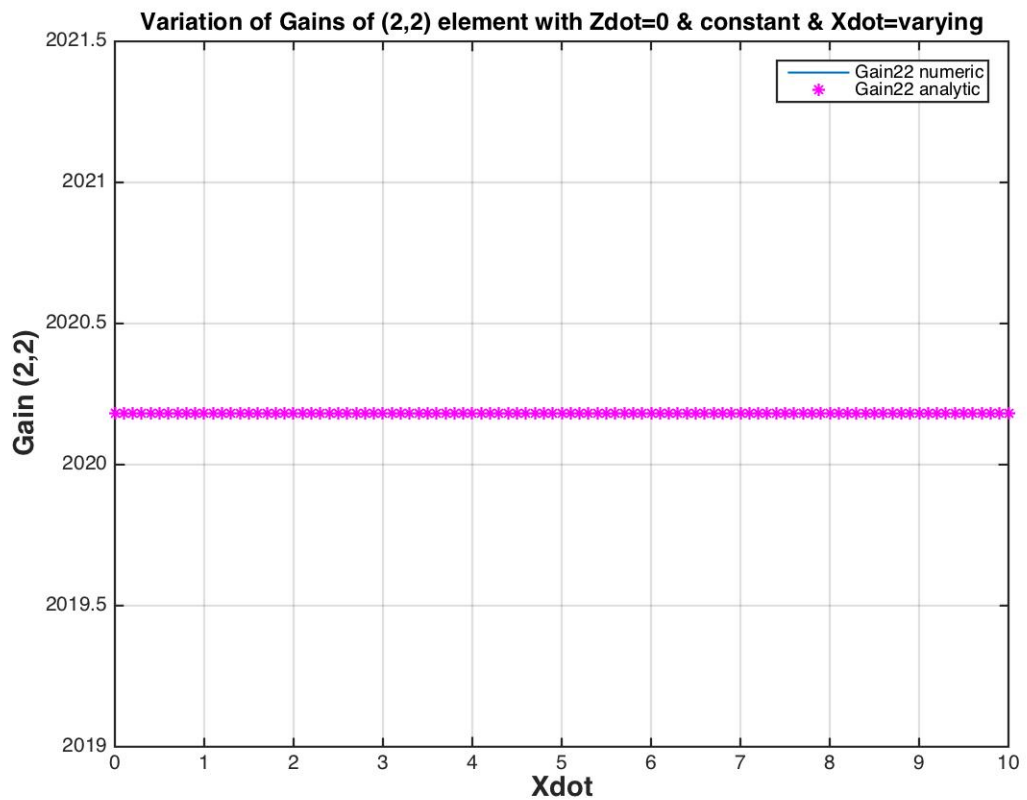


**Figure 3.12:** Comparison of Gain(2,2) analytic and numeric

## Bode Plots

This section will discuss the frequency response of the plant for the forward flight condition.

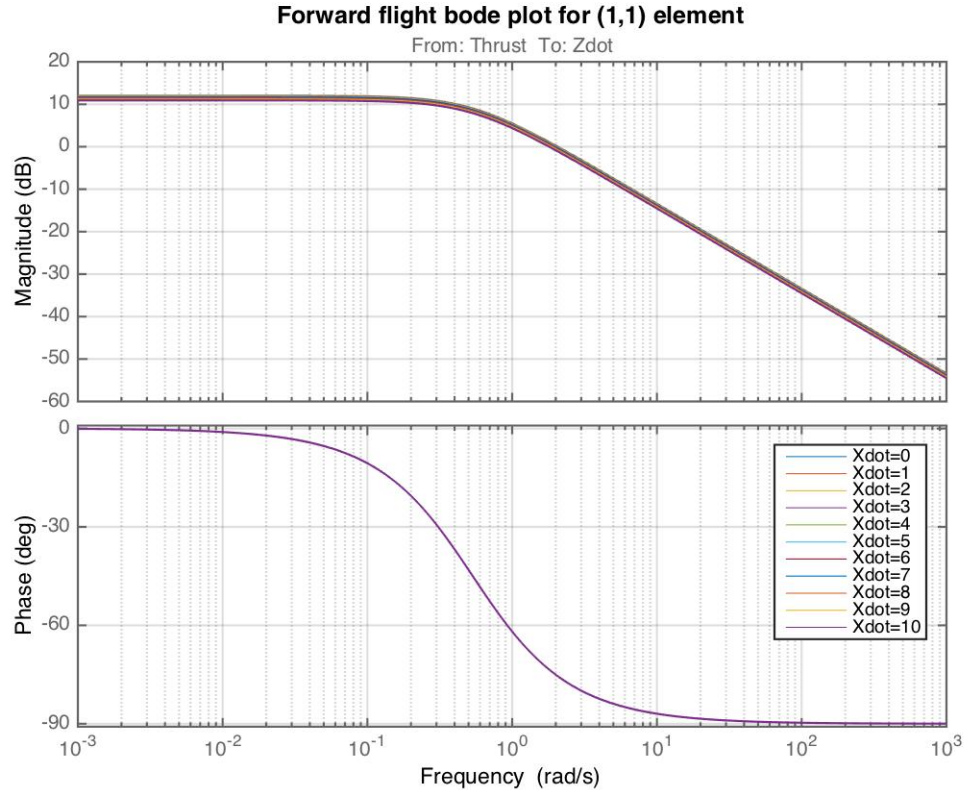


**Figure 3.13:** Frequency Response magnitude & phase plot for element (1,1): forward flight condition

Figure(3.13) shows the frequency response for the transfer function from  $\dot{z}$  to Thrust with the forward flight condition.

- From the magnitude plot we see that at low frequencies, the magnitude is almost constant for all forward flight conditions ( $\approx 12\text{dB}$ ) and decreases with a slope of  $-20 \text{ dB/dec}$ .
- From the phase plot we see that at low frequencies the phase is  $0^\circ$  and becomes

$-90^\circ$  at high frequencies.

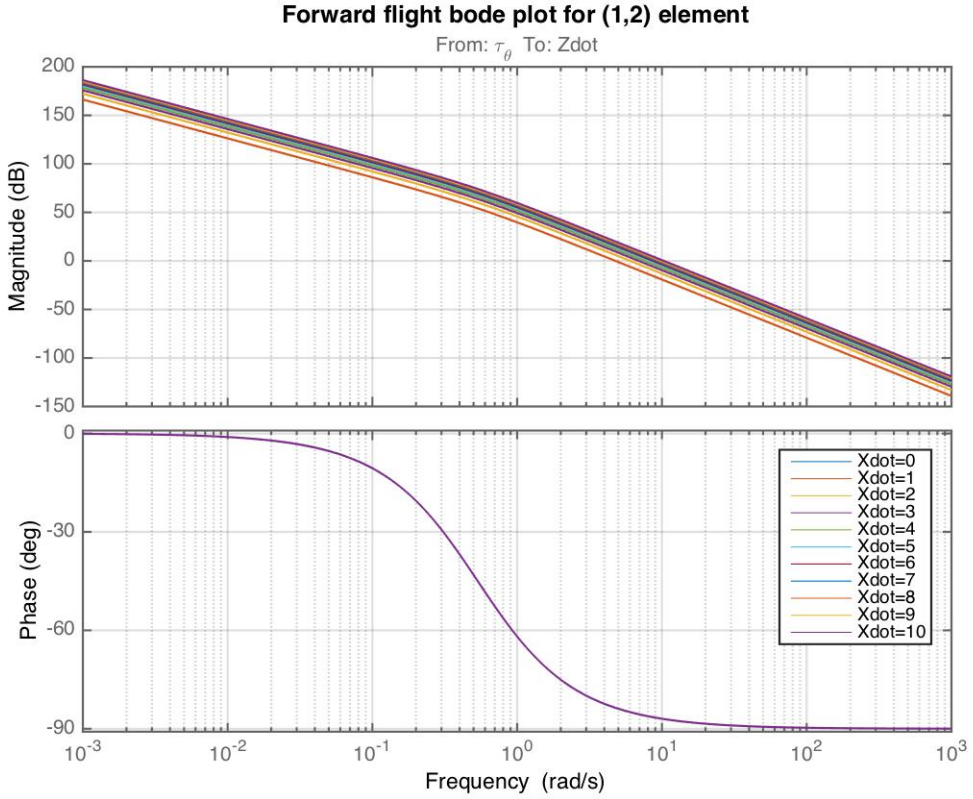


**Figure 3.14:** Frequency Response magnitude & phase plot for element (1,2): forward flight

Figure(3.14) shows the bode magnitude and phase plots for the transfer function from  $\dot{z}$  to  $\tau_\theta$  with the forward flight condition.

- From the magnitude plot we see that , at low frequencies the magnitude is infinite because of the presence of two integrators and decreases with a slope of  $-40\text{dB/dec}$ . At high frequencies, the magnitude decreases with a slope of  $-60\text{dB/dec}$ .
- From the phase plot, at low frequencies the phase is  $0^\circ$  and decreases to  $-90^\circ$  at high frequencies.

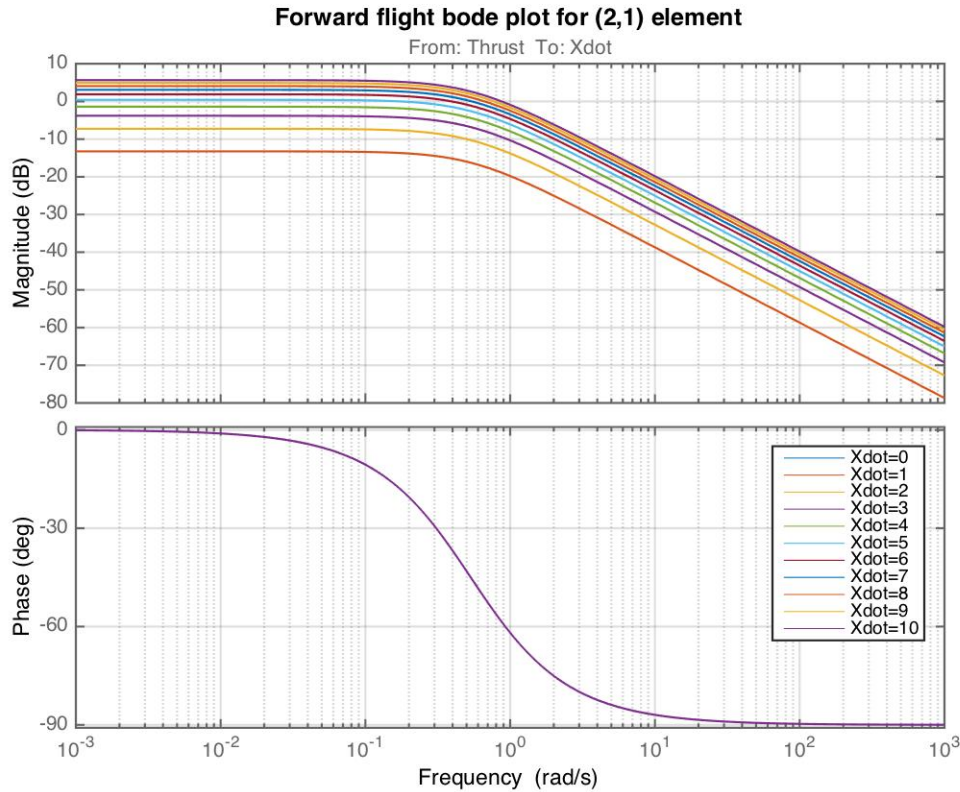


**Figure 3.15:** Frequency Response magnitude & phase plot for element (2,1) : forward flight condition

Figure(3.15) shows the bode magnitude and phase for the transfer function from  $\dot{x}$  to Thrust with the forward flight condition. We see that

- From the bode magnitude plot we see that, at low frequencies there is an appreciable change in the peaks of the frequency response as the forward flight condition changes. The peak values are listed in the table(3.4.2). At high frequencies the magnitude rolls off with a slope of  $-20\text{dB/dec}$ .
- From the bode phase plot we can see that, at low frequencies the phase is  $0^\circ$  and decreases to  $-90^\circ$  at high frequencies.

$\dot{x}$	Mag in dB
$\dot{x} = 0$	-13.3 dB
$\dot{x} = 2$	-7.27 dB
$\dot{x} = 4$	-1.4 dB
$\dot{x} = 6$	1.66 dB
$\dot{x} = 8$	4.07 dB
$\dot{x} = 10$	5.63 dB

**Table 3.2:** Variation of Bode magnitude with flight condition

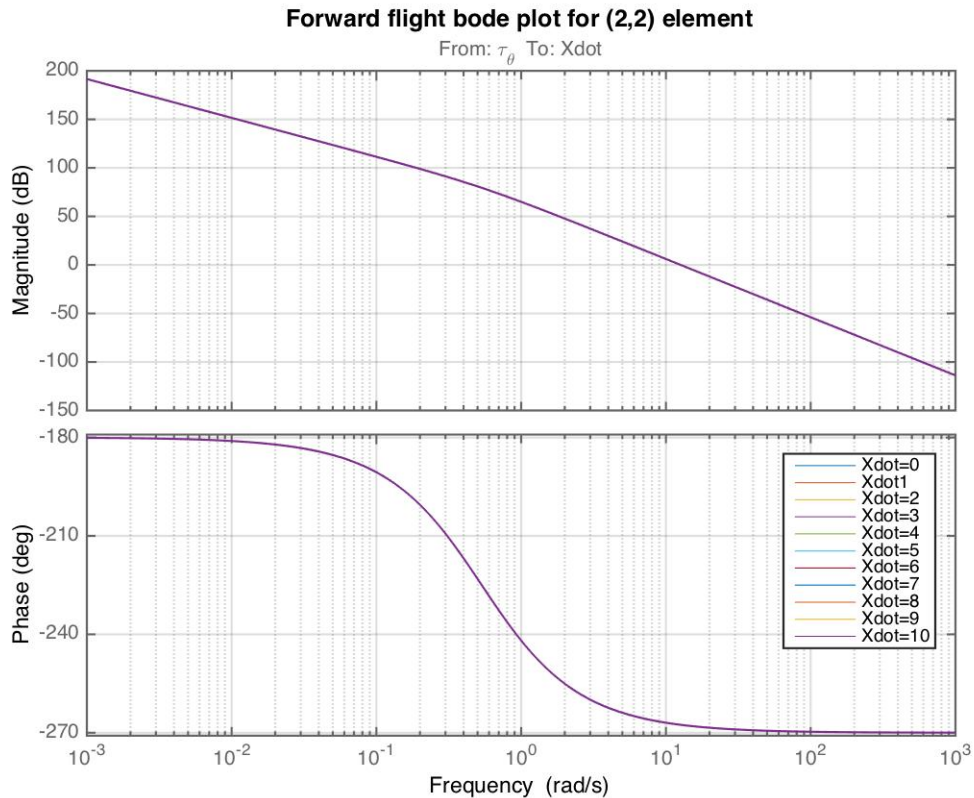


**Figure 3.16:** Frequency Response magnitude & phase plot for element (2,2): forward flight condition

Figure(3.16) shows the frequency response for the transfer function from  $\dot{x}$  to  $\tau_\theta$ .

- From the magnitude plot, at low frequencies the magnitude is large due to the presence of two integrators and decreases with a slope of -40dB/dec. At high frequencies, magnitude decreases with a slope of -60dB/dec.
- From the phase plot, at low frequencies the phase is  $-180^\circ$  and decreases to  $-270^\circ$  at high frequencies.

### 3.4.3 Forward and Vertical Flight

This scenario discusses quadrotor flight when it moves forward and continues to climb. Equilibrium analysis for this scenario is performed on the similar lines as previous flight condition. The change in the equilibrium thrust ( $T_{eq}$ )t with change in the flight condition is illustrated in Figure(3.17)

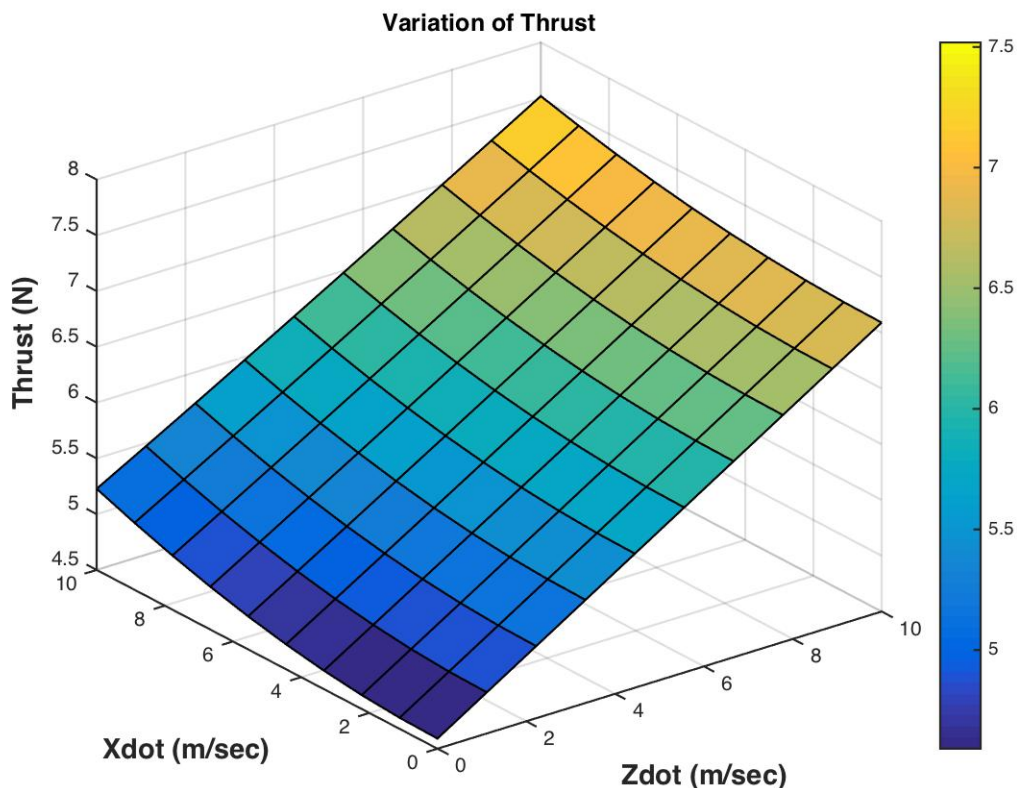


**Figure 3.17:** Thrust Variation

- Thrust variation is more drastic in  $\dot{z}$  direction as compared to the  $\dot{x}$ .

The variation of the equilibrium moment is illustrated in Fig(3.18)

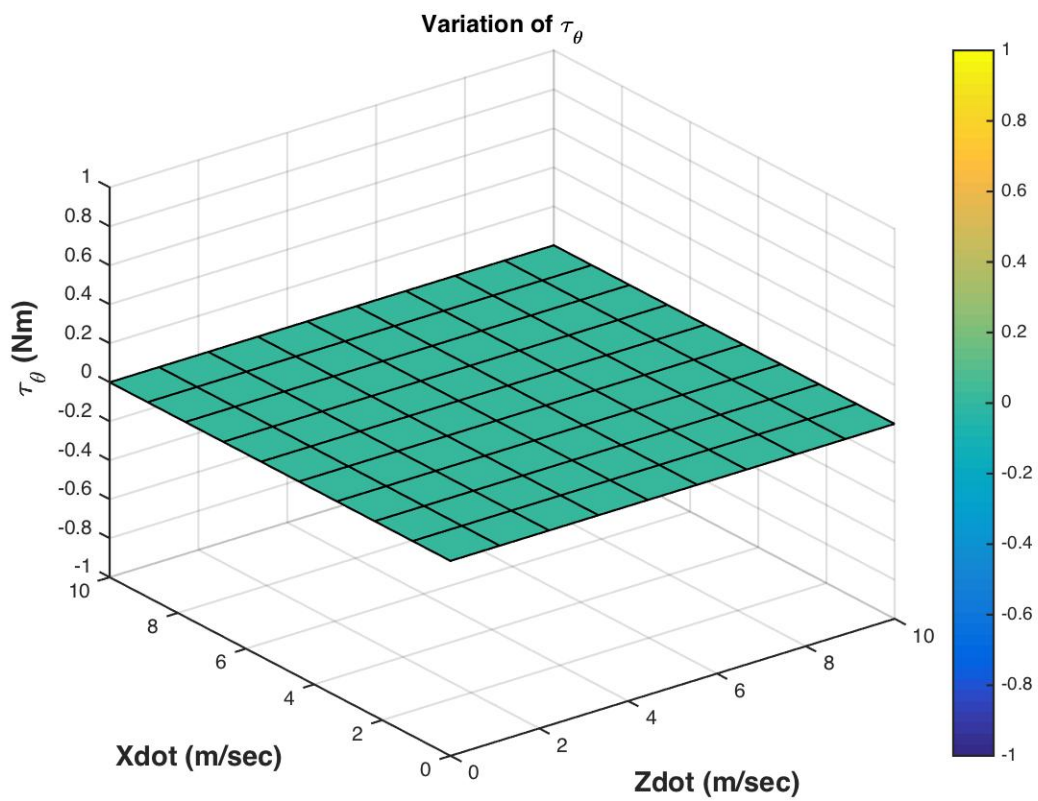


**Figure 3.18:** Variation of  $\tau_\theta$

The equilibrium angle  $\theta$  required for this flight condition is given by Eqn(3.24)

$$\theta_{eq} = \arctan\left(\frac{A_x \dot{x}_{eq}}{mg + A_z \dot{z}_{eq}}\right) \quad (3.24)$$

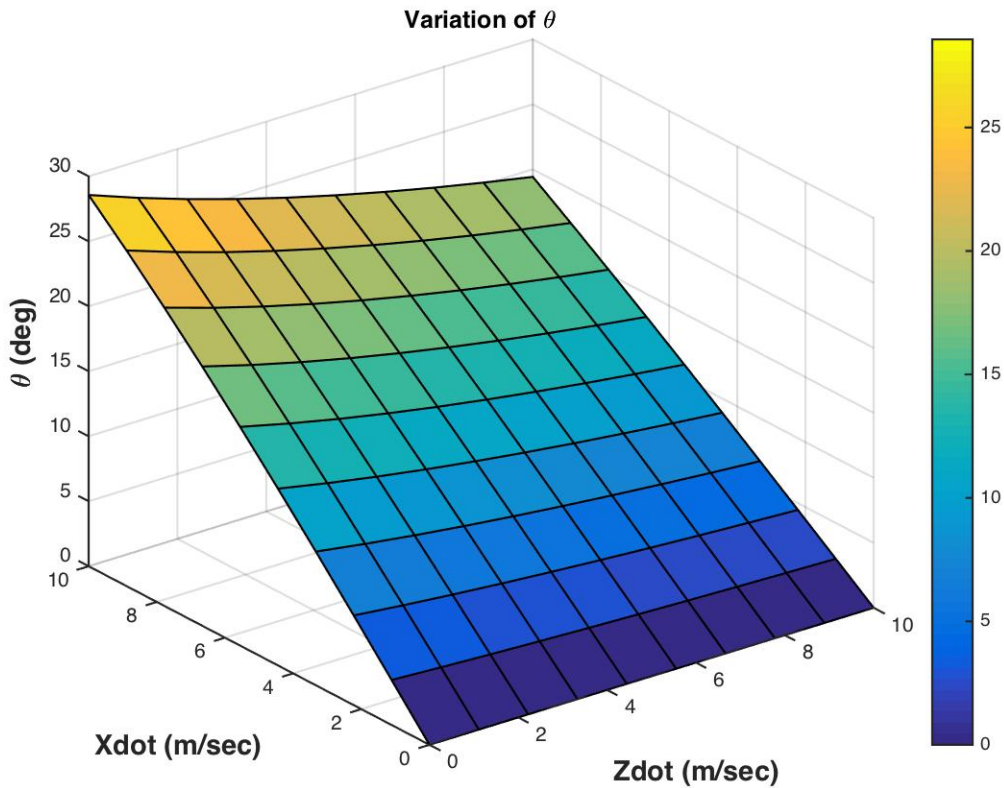


**Figure 3.19:** Variation of  $\tau_\theta$

From the fig(3.19) we see that

- $\theta_{eq}$  varies gradually with vertical velocity only when it also has forward motion.
- Forward flight velocity has significant dependency on  $\theta_{eq}$ .

The effect of forward flight and vertical climb on the transfer function gains is discussed below

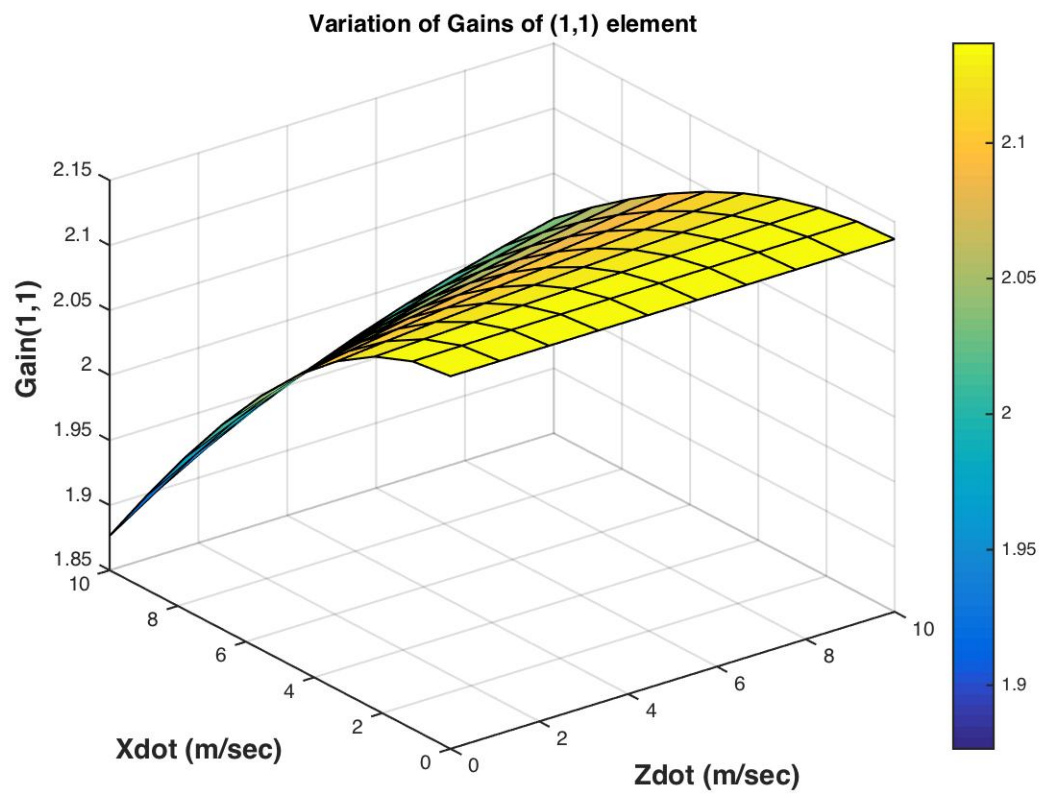


**Figure 3.20:** Variation of Gain(1,1)

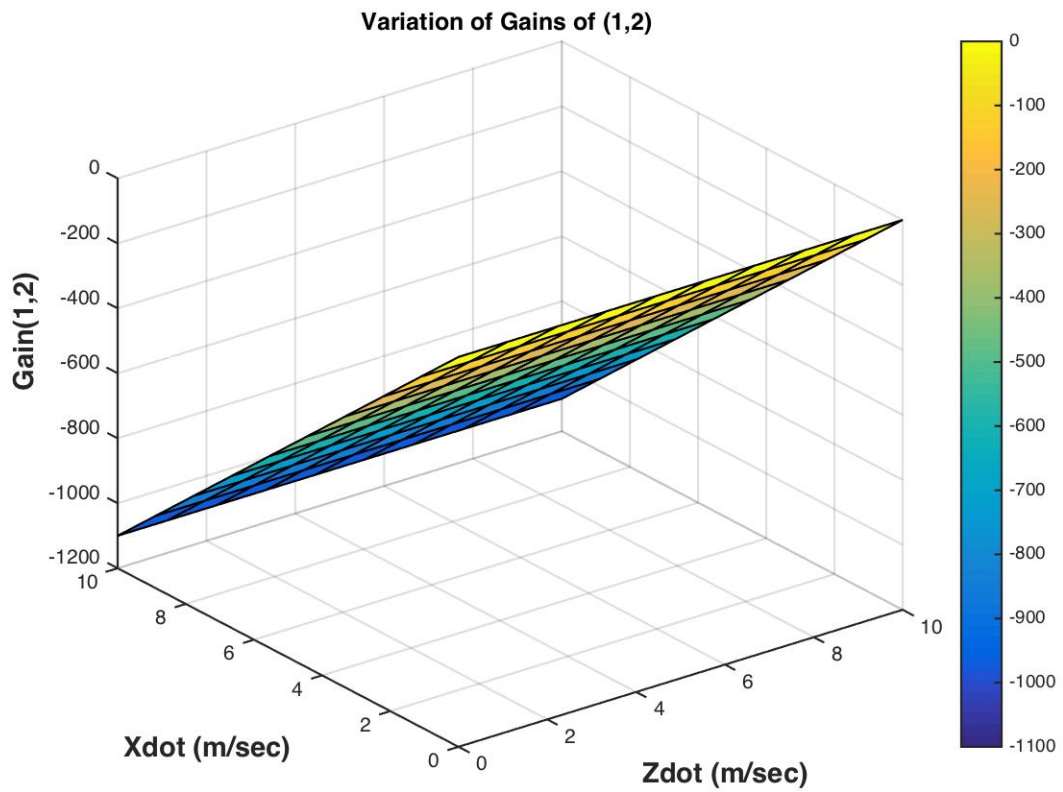


**Figure 3.21:** Variation of Gain(1,2)

From the fig(3.21) we observe that

- Gain is independent of climb velocity.
- Gain varies proportionally with forward velocity.

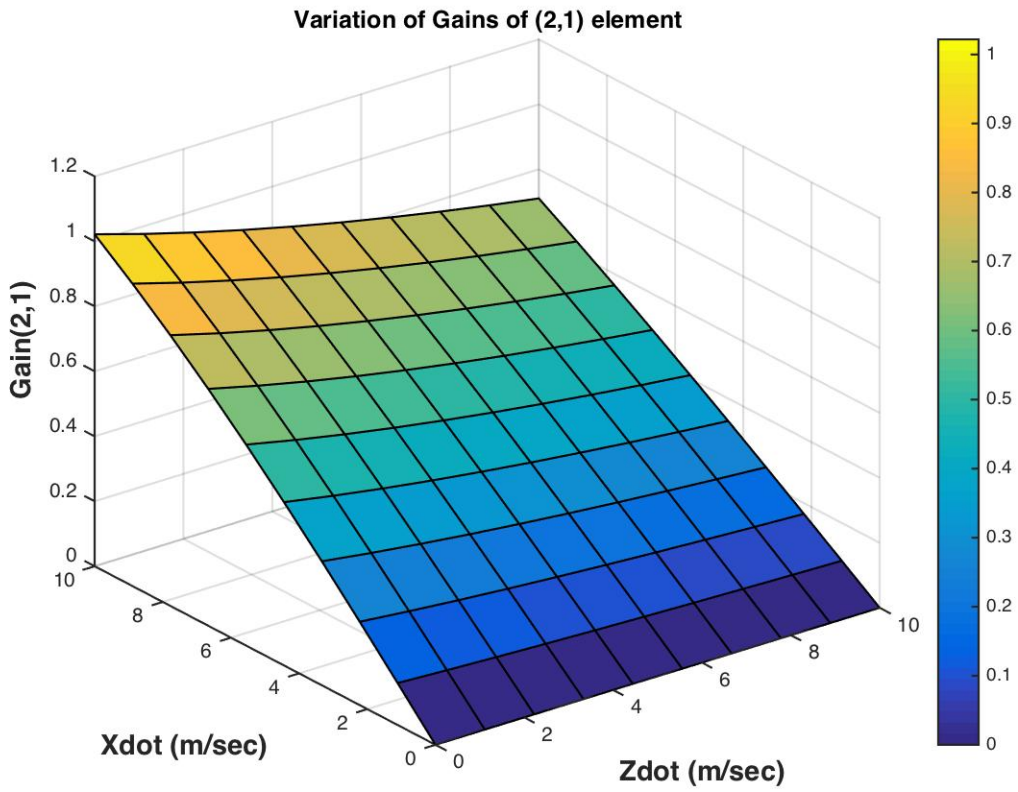


**Figure 3.22:** variation of Gain(2,1)

From the fig(3.22) we can conclude that

- Gain is independent of vertical climb velocity.
- At hover, it is zero thus ensuring that the model is decoupled.

From the fig(3.23) we can conclude that

- Gain is significantly affected by the vertical climb velocity.
- Gain remains relatively unaffected by forward velocity.

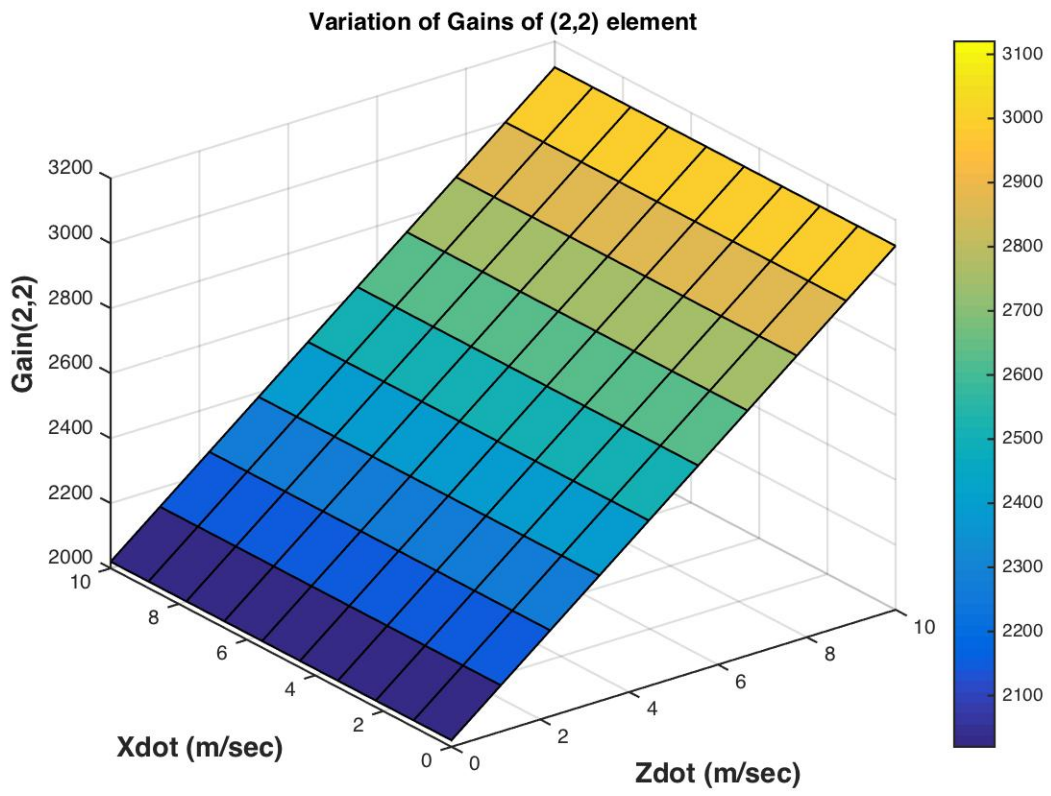


**Figure 3.23:** Variation of Gain(2,2) with the flight condition 4

### 3.5 Impact of Mass and Length

This section will discuss the effect of the physical parameters like mass and length on the quadrotor dynamics.

### 3.5.1 Impact of mass change

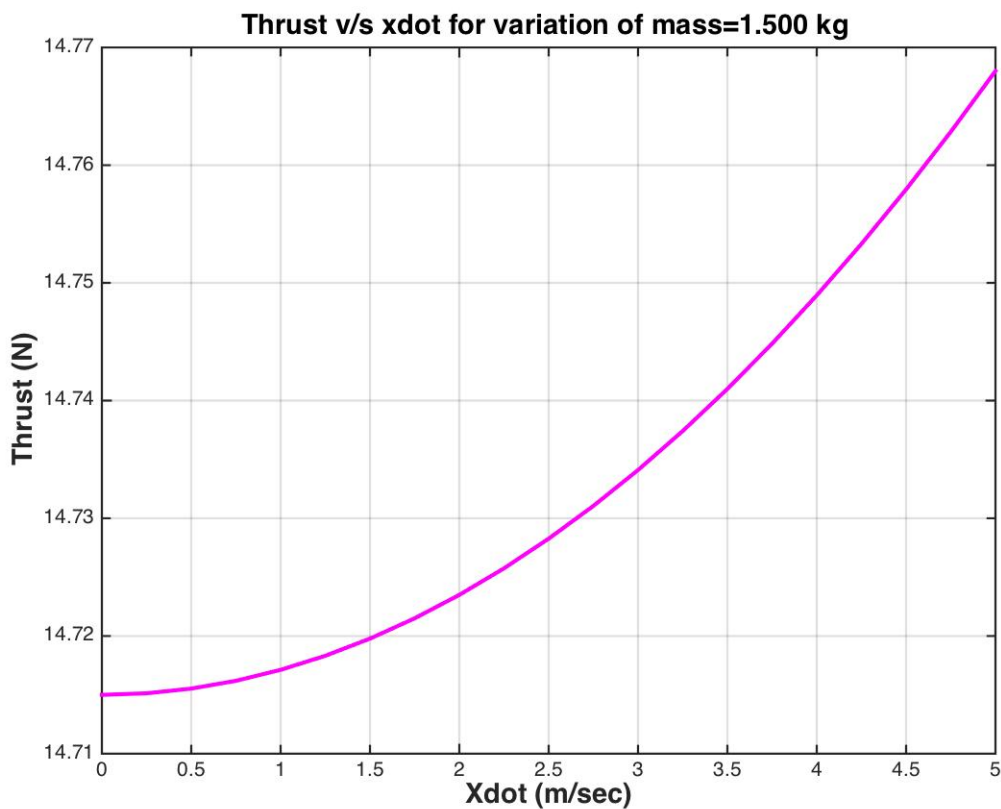


**Figure 3.24:** Variation of Thrust for with mass=1.5 kg and forward velocity

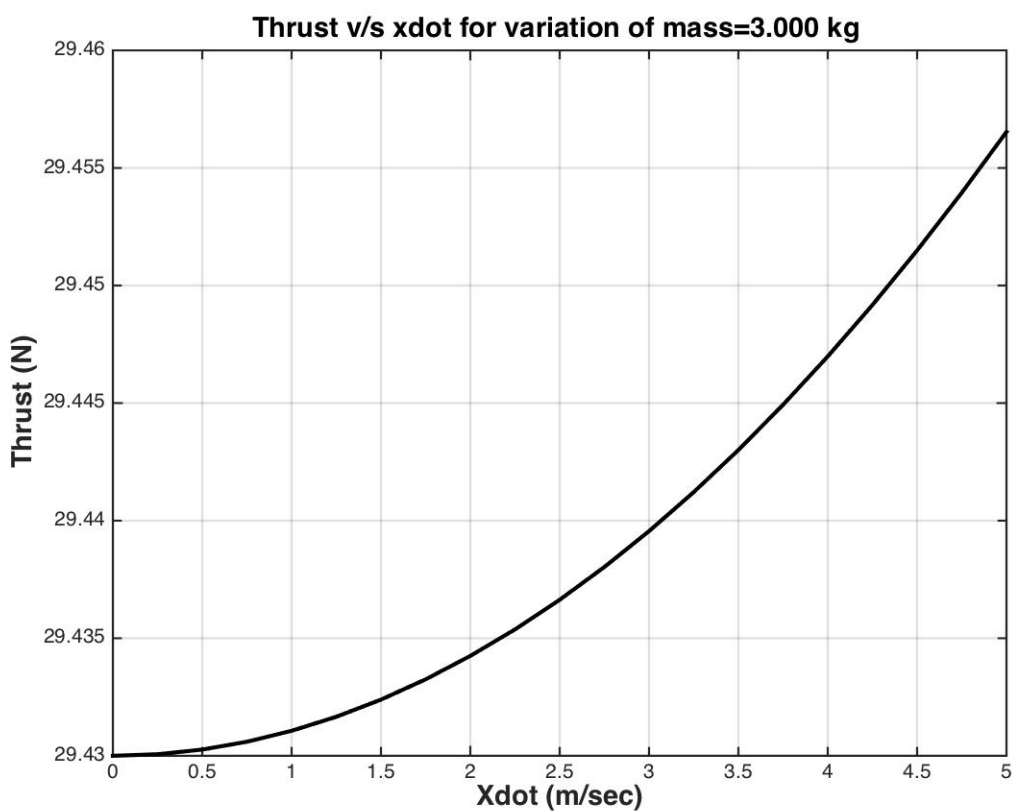


**Figure 3.25:** Variation of Thrust with mass=3 kg and forward velocity

- The effect of mass is on Thrust is more significant at low forward flight speeds.

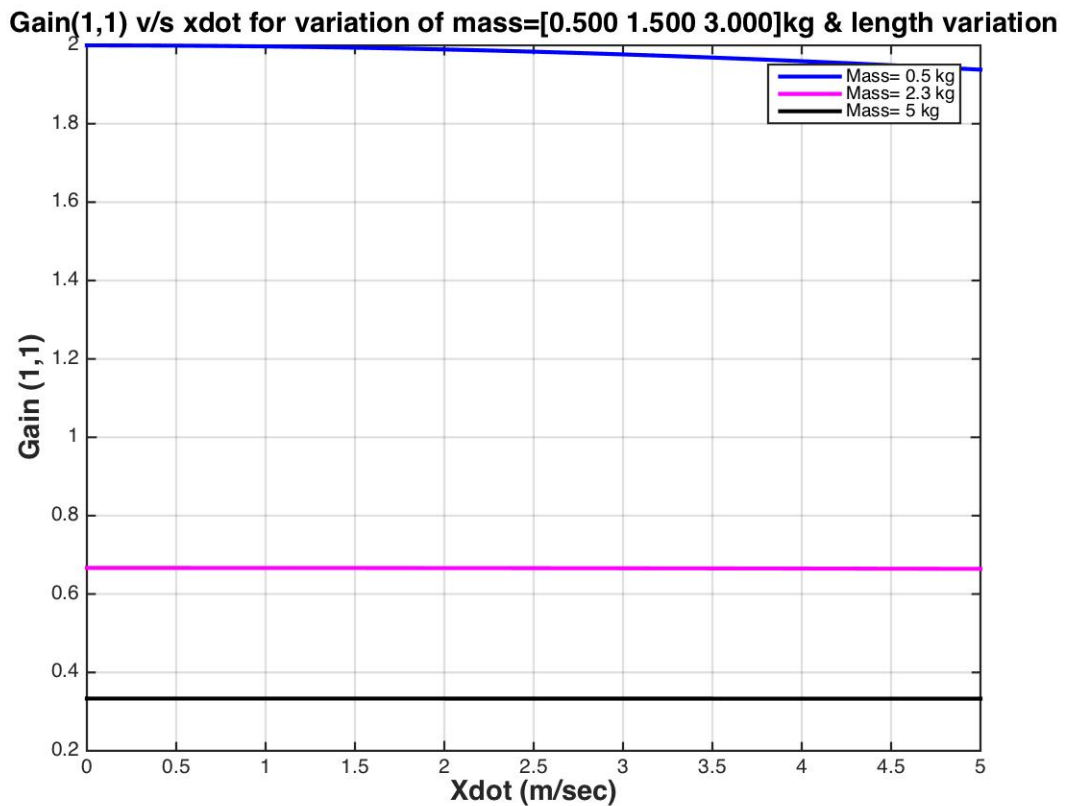


**Figure 3.26:** Variation of Gain(1,1) with the mass

- Mass increase causes the gain to decrease significantly and is more significant at low forward flight speeds.

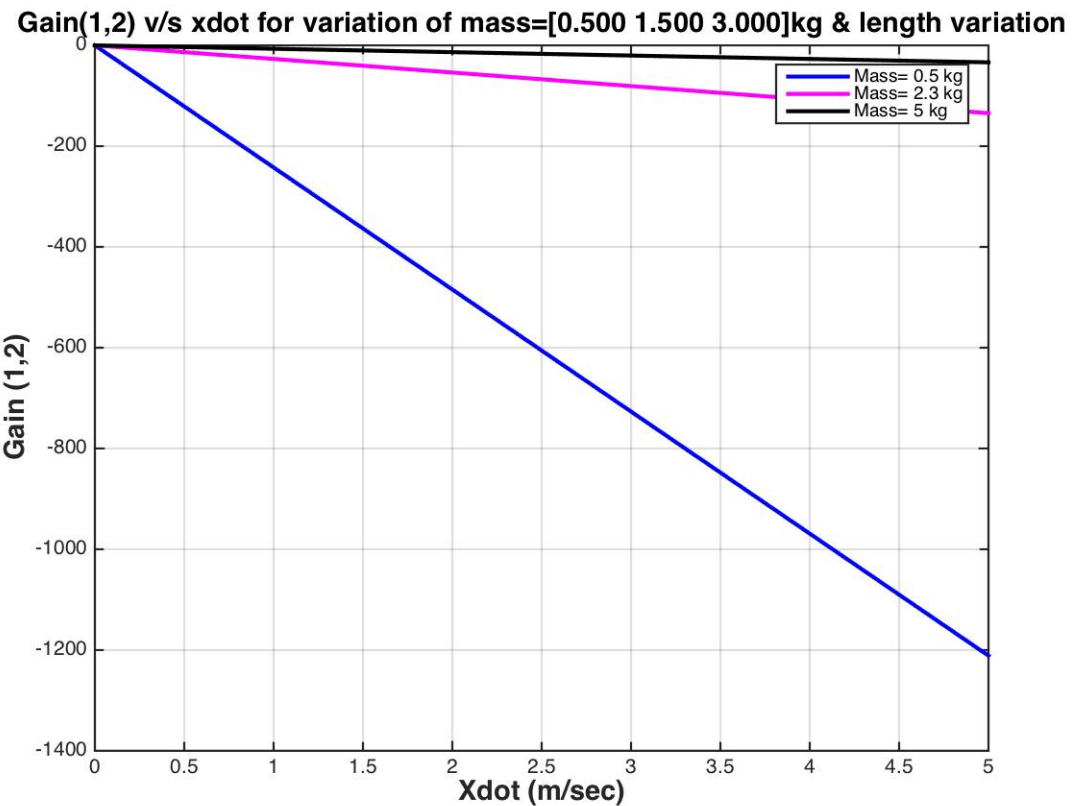


**Figure 3.27:** Variation of Gain(1,2) with the mass

- Mass increase causes the gain to decrease and its effect is more significant with high flight velocities.

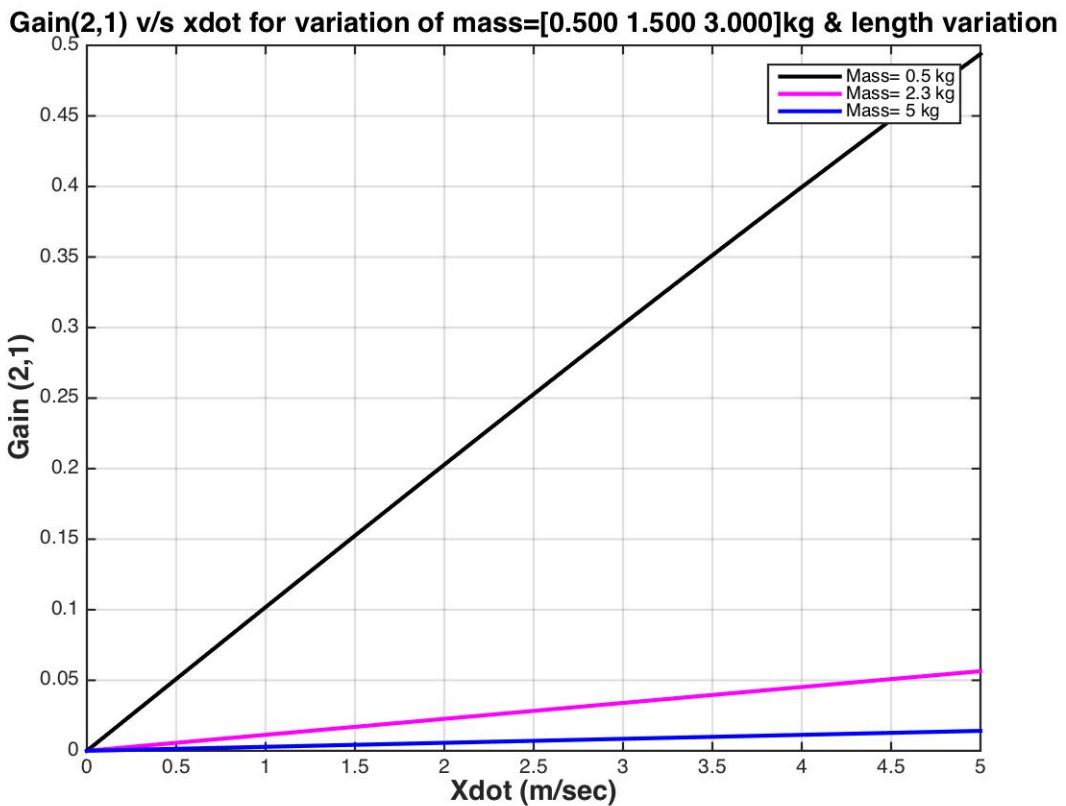


**Figure 3.28:** Variation of Gain(2,1) with the mass

- Mass increase causes the gain to increase very gradually but its effect is more significant with high forward velocities.

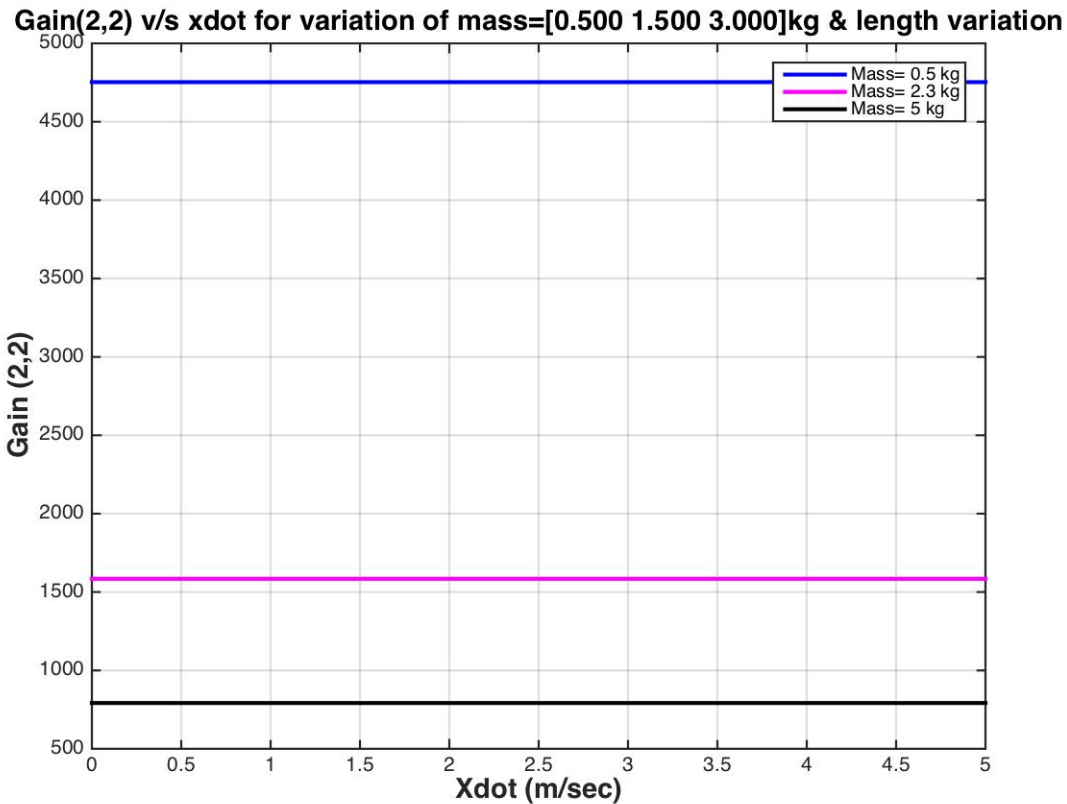


**Figure 3.29:** Variation of Gain(2,2) with the mass

- Mass increase causes the gain to increase significantly but it remains unchanged with forward velocities.

In summary:

- From the analytical expression (3.20) we can see that the effect of mass is not significant as is verified by the figure(3.26)
- From the analytical expression (3.21), gain(1,2) is inversely proportional to the mass verified by the figure(3.27)
- From the analytical expression (3.22) we see that the gain(2,1) is inversely proportional to mass as verified in figure(3.28)

- From the analytical expression (3.23) we see that as mass increases the inertia increases and hence the gain.

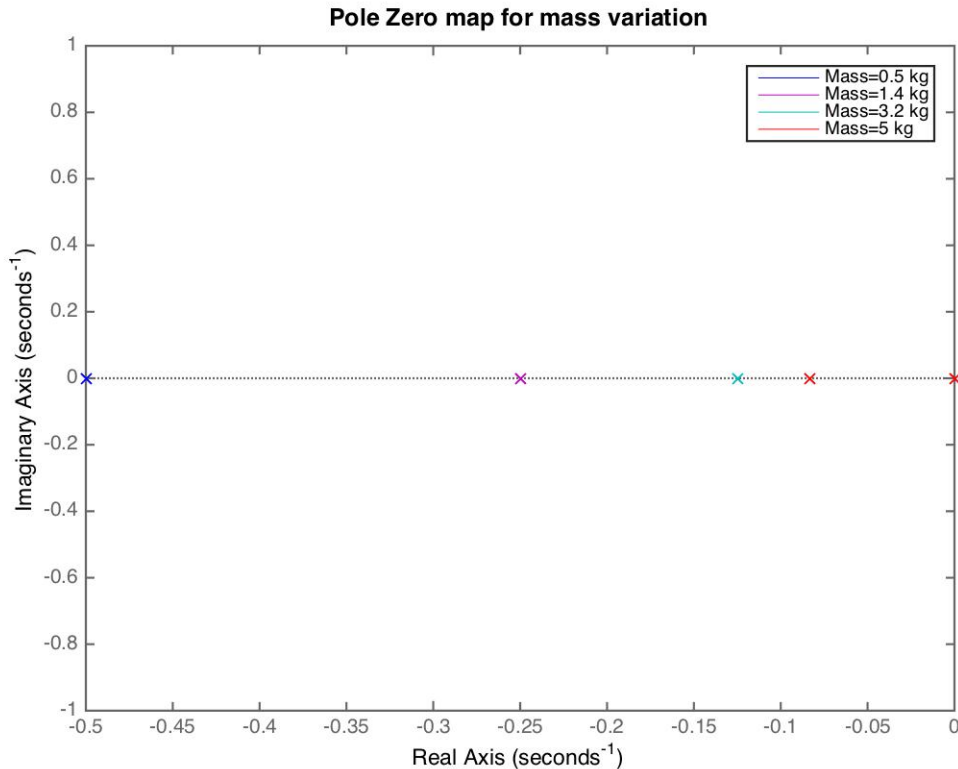


**Figure 3.30:** System poles variation with mass

- As mass increases the poles move towards the origin thereby decreasing the stability of the system.

### 3.5.2 Impact of Length change

Thrust is independent of change in geometry of the system. As a result it remains unchanged with length.

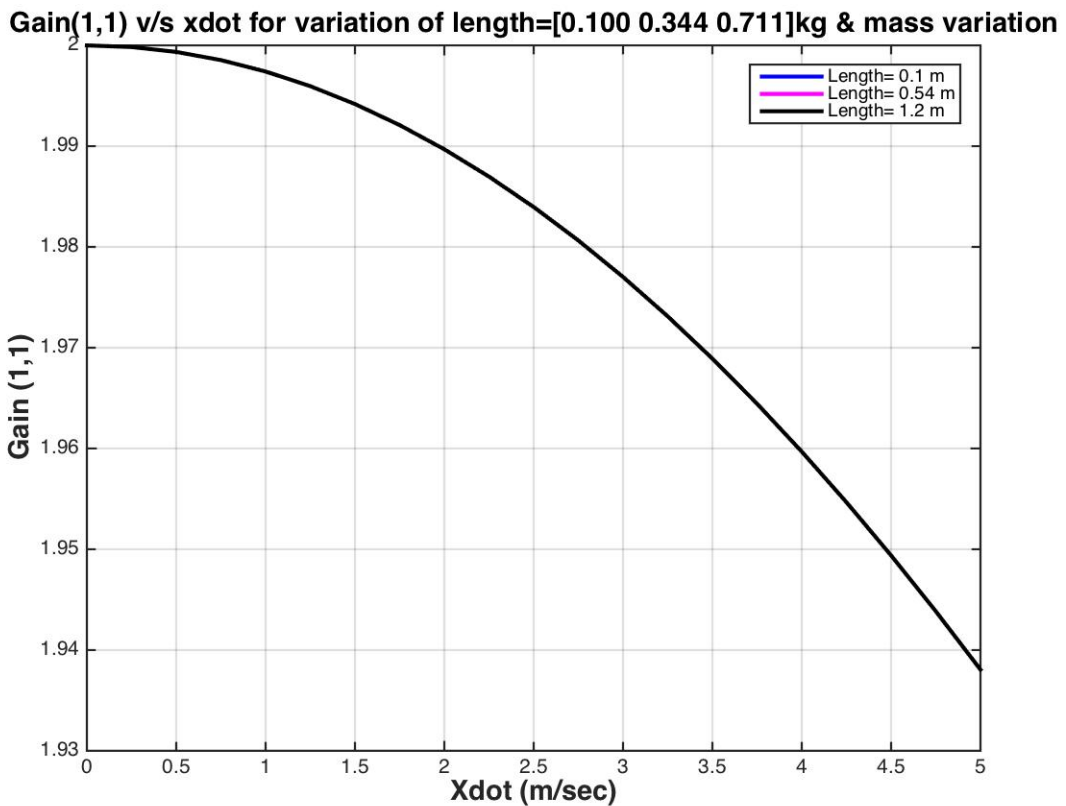


**Figure 3.31:** Variation of gain(1,1) with length

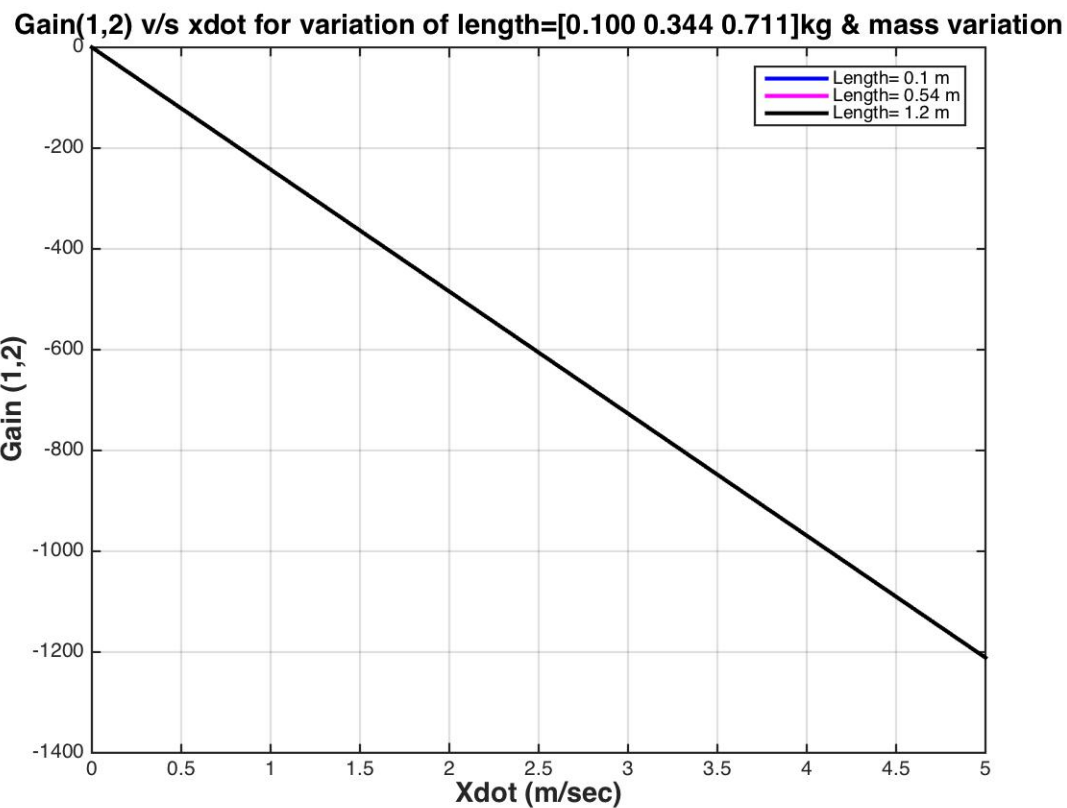


**Figure 3.32:** Variation of gain(1,2) with length

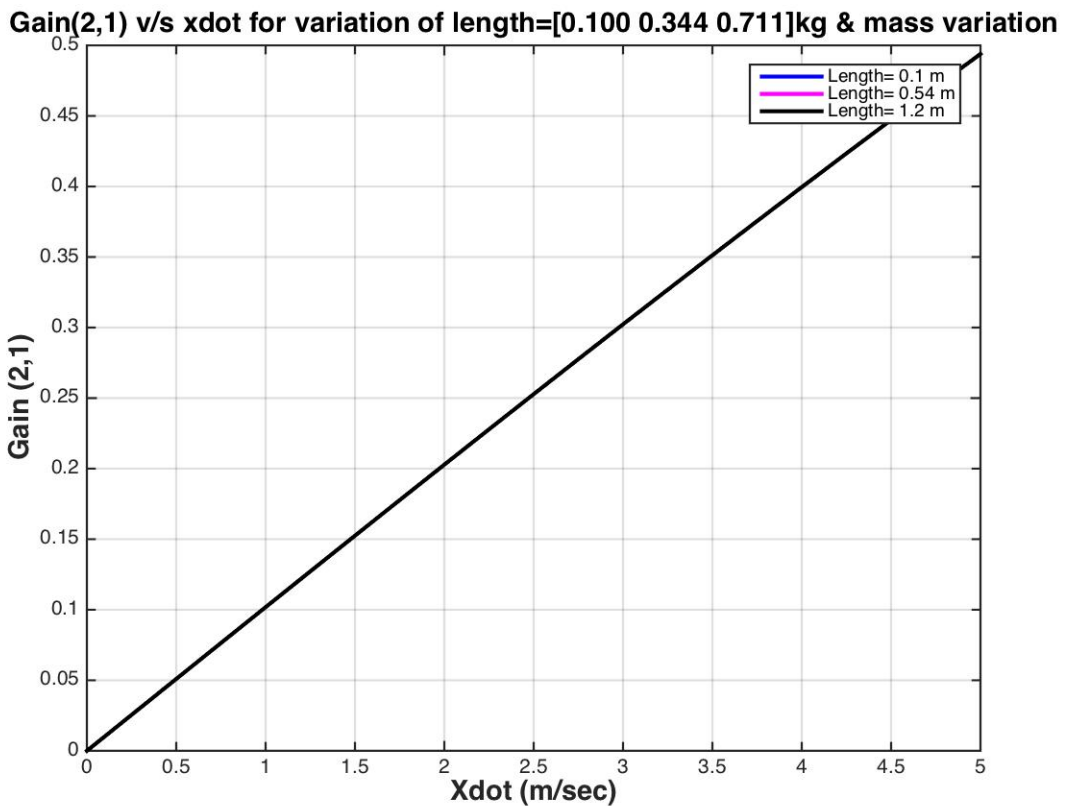


**Figure 3.33:** Variation of gain(2,1) with length

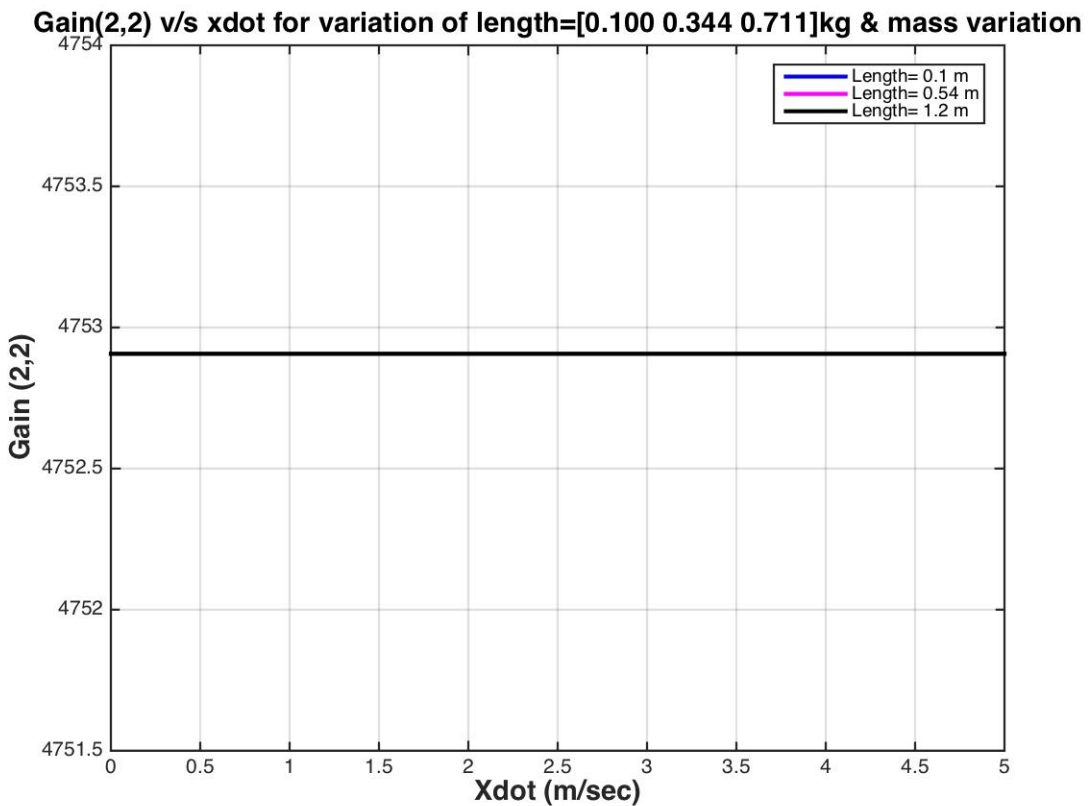


**Figure 3.34:** Variation of gain(2,2) with length

- From fig(3.31)-fig(3.34) we see that length variation does not affect the system properties in forward flight.

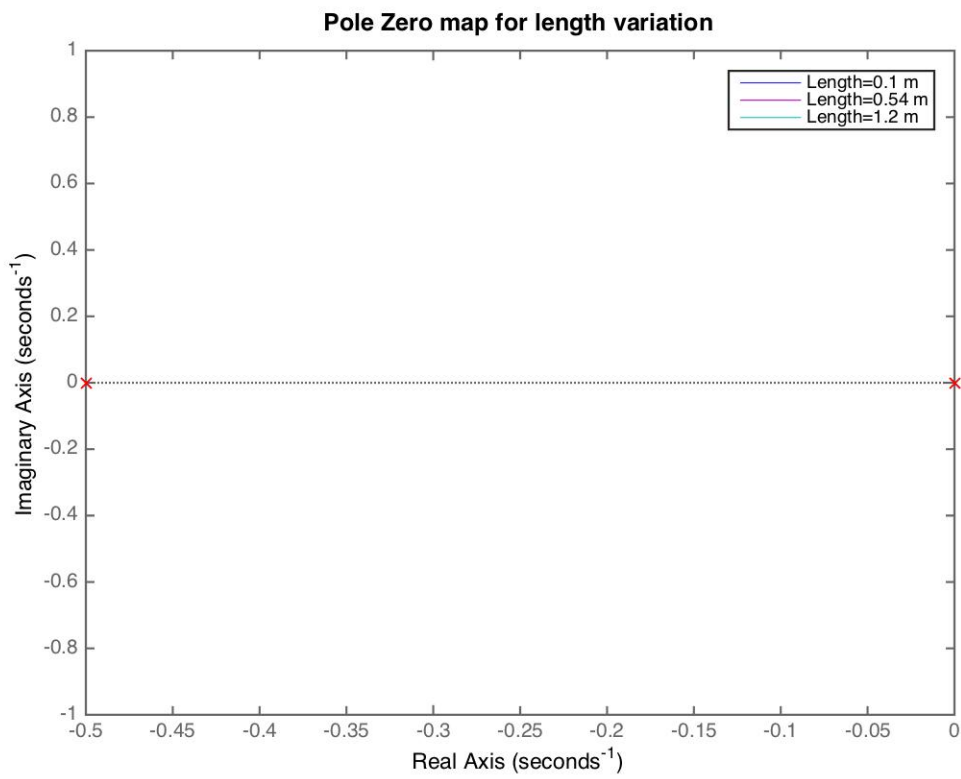


**Figure 3.35:** System poles variation with length

## Chapter 4

### CONTROL DESIGN

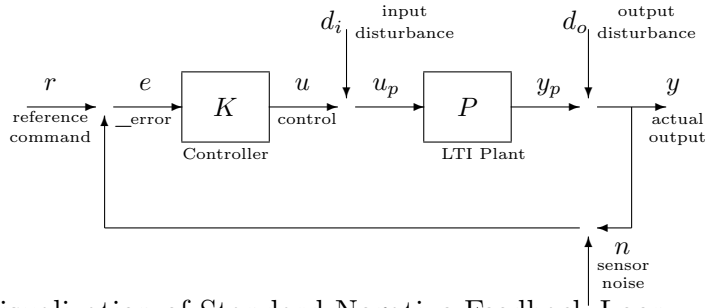


**Figure 4.1:** Visualization of Standard Negative Feedback Loop

#### 4.1 Longitudinal mode Controller Design

In this chapter we will discuss the design of the hover controller. The plant transfer function at hover can be represented by

$$\begin{bmatrix} P_{11} & 0 \\ 0 & P_{22} \end{bmatrix} \quad (4.1)$$

where  $P_{11}$  is the transfer function from Thrust to  $\dot{z}$ .

$$P_{11} = \frac{g_{11}}{(s + a)} \quad (4.2)$$

and  $P_{22}$  is the transfer function from  $\tau_\theta$  to  $\dot{x}$ .

$$P_{22} = \frac{g_{22}}{s^2(s+a)} \quad (4.3)$$

The parameter values are taken from Table(3.3)

#### 4.1.1 Controller design for transfer function from Thrust to $\dot{z}$

The structure of the controller for eqn(4.2) is chosen as

$$K_{11} = \frac{g(s+z)}{s} \quad (4.4)$$

The parameters  $g$  and  $z$  are found out using pole placement. For a settling time of 5 sec and percentage overshoot of less than 10%, we get the desired closed loop poles to  $s = -1 \pm j1$

#### 4.1.2 Controller design for transfer function from $\tau_{theta}$ to $\dot{x}$

The controller for eqn(4.3) is designed using classical concept of lead-lag design.

### Lead Lag Control design

The controller for forward flight was designed with a classical lead-lag architecture. The structure for the controller was adopted from [11],[10] with a pair of complex pole - zero as shown in Eqn(4.5). The lead lag strategy was used as it provides a classical strategy for loop shaping and controller synthesis. From the fig(3.16) we see that there is a phase lag of 180 deg due to the presence of two integrators in the plant. Also, from the *Internal Model Principle* for step input disturbance rejection we need an integrator in the controller. This additional integrator adds a phase lag of 90 deg. Thus

- Single lead lag network would be insufficient to provide the required phase lead.
- The phase lead requirement would result in non-optimal zero locations which could affect the stability of the system.
- A cascaded lead lag network with one pair of complex poles and zeros along with a simple lead lag is chosen as the structure of the controller.

The complex lead-lag network is designed to provide symmetrical phase lead ( $\phi_m$ ) at the desired unity gain crossover frequency( $\omega_m$ )

$$K_{22} = \left[ \frac{s^2 + 2\zeta\omega_z s + \omega_z^2}{s^2 + 2\zeta\omega_p s + \omega_p^2} \right] \sqrt{\frac{p}{z}} \begin{bmatrix} s+z \\ s+p \end{bmatrix} \quad (4.5)$$

where:

$$\omega_z = \omega_g (\zeta \tan(\phi_m) + \sqrt{\zeta^2 \tan(\phi_m)^2 + 1}) \quad (4.6)$$

$$\omega_p = \omega_g (-\zeta \tan(\phi_m) + \sqrt{\zeta^2 \tan(\phi_m)^2 + 1}) \quad (4.7)$$

$$\frac{p}{z} = \frac{1 + \sin(\phi_m)}{1 - \sin(\phi_m)} \quad (4.8)$$

where:

- $\phi_m$  : desired phase lead / Phase Margin at the desired unity gain frequency.
- $\omega_g$ : desired unity gain crossover frequency.
- $z$  : Zero of the single lead- lag compensator.
- $p$  : Pole of the single lead- lag compensator.

The following section discusses the effect of the controller parameters on the closed loop system properties. [14]

#### 4.1.3 Sensitivity

$S$  is the transfer function from the reference to the error.

$$S_o = [I + L_o]^{-1} \quad (4.9)$$

Figures(4.2)-(4.4) show the variation of Sensitivity with the controller parameter

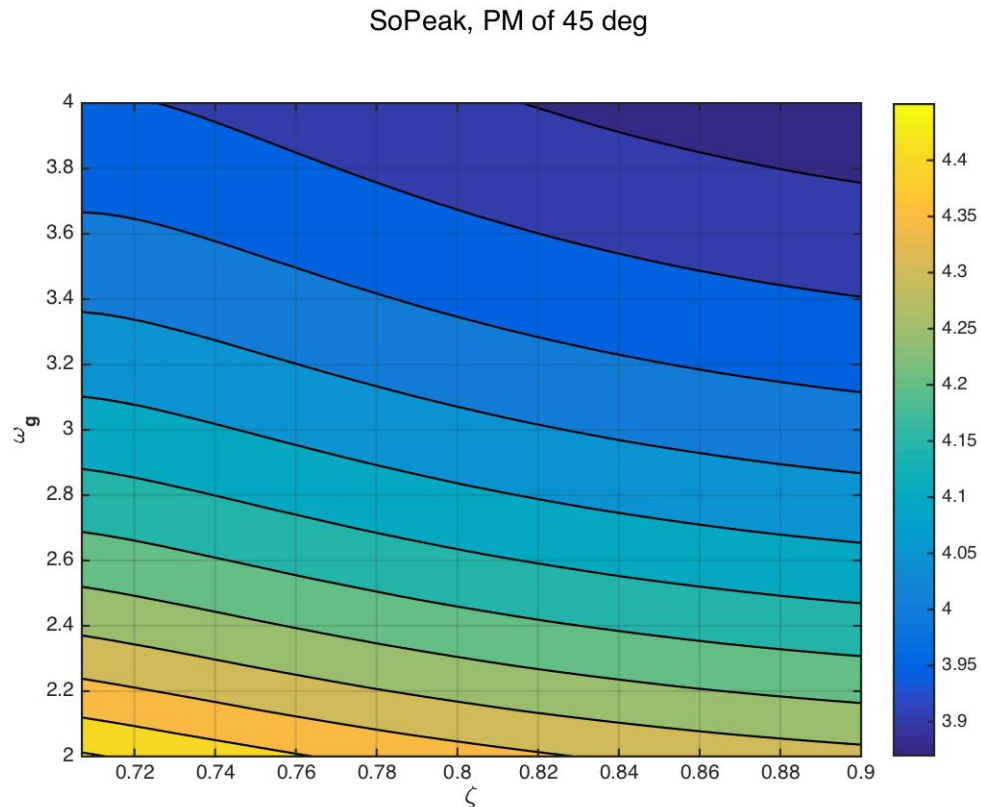


**Figure 4.2:** Sensitivity ( $\zeta$  vs  $\omega_g$ ) for PM=45 deg

- As  $\zeta$  increases  $|S_o|_{peak}$  decreases .
- As  $\omega$  increases  $|S_o|_{peak}$  decreases significantly.

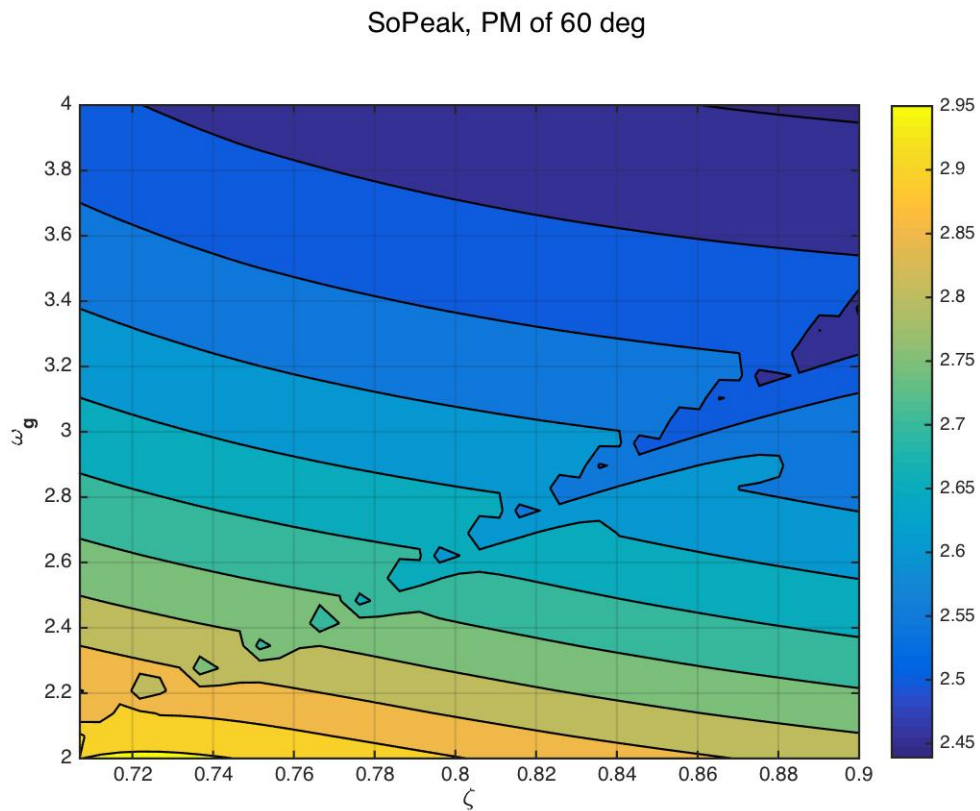


**Figure 4.3:** Sensitivity (  $\zeta$  vs  $\omega_g$  ) for PM=60 deg

- As  $\zeta$  increases  $|S_o|_{peak}$  decreases .
- As  $\omega$  increases  $|S_o|_{peak}$  decreases significantly.

SoPeak, PM of 70 deg

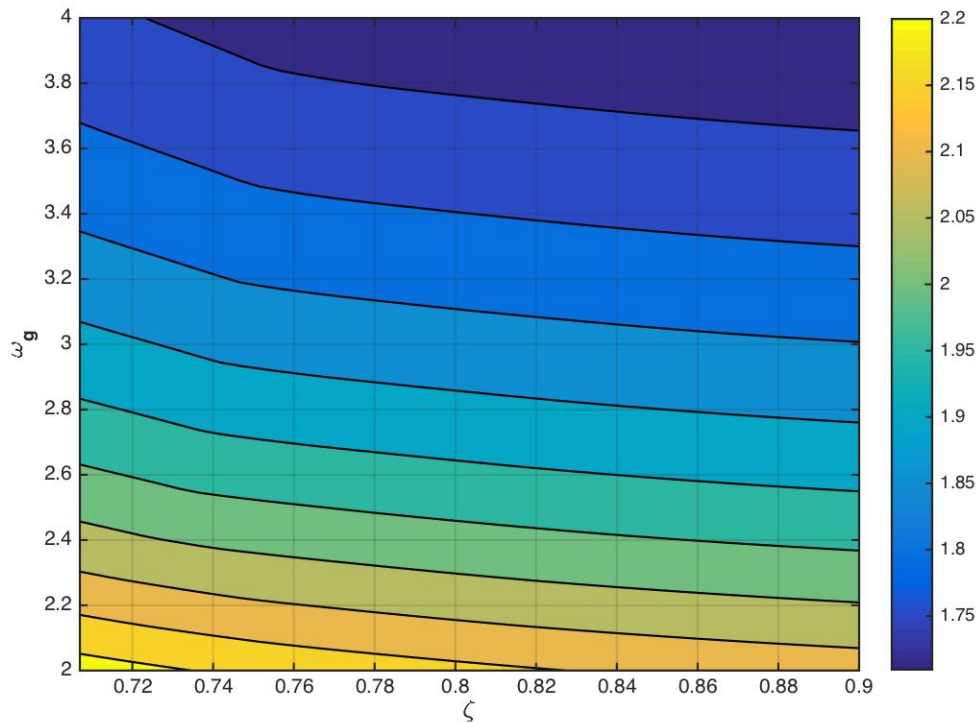


**Figure 4.4:** Sensitivity (  $\zeta$  vs  $\omega_g$  ) for PM=70 deg

- As  $\zeta$  increases  $|S_o|_{peak}$  decreases .
- As  $\omega$  increases  $|S_o|_{peak}$  decreases significantly.

#### 4.1.4 Complimentary Sensitivity

The complimentary sensitivity is the closed loop transfer function from  $r$  to output  $y$

$$T = L[I + L]^{-1} \quad (4.10)$$

Figures from fig(4.5) to fig(4.7) discuss the effect on the Complimentary sensitivity with the variation in the controller parameters

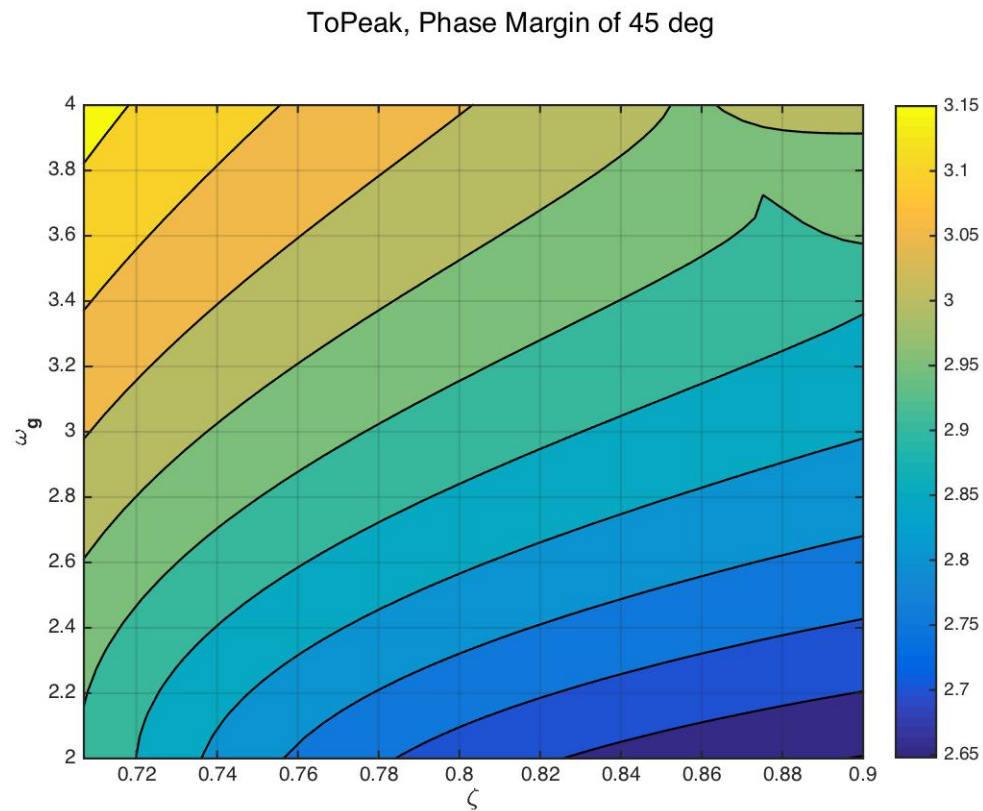


**Figure 4.5:** Reference to output ( $\zeta$  vs  $\omega_g$ ) for PM 45 deg

- As  $\zeta$  increases  $|T_o|_{peak}$  decreases .

- As  $\omega_g$  increases  $|T_o|_{peak}$  decreases significantly.

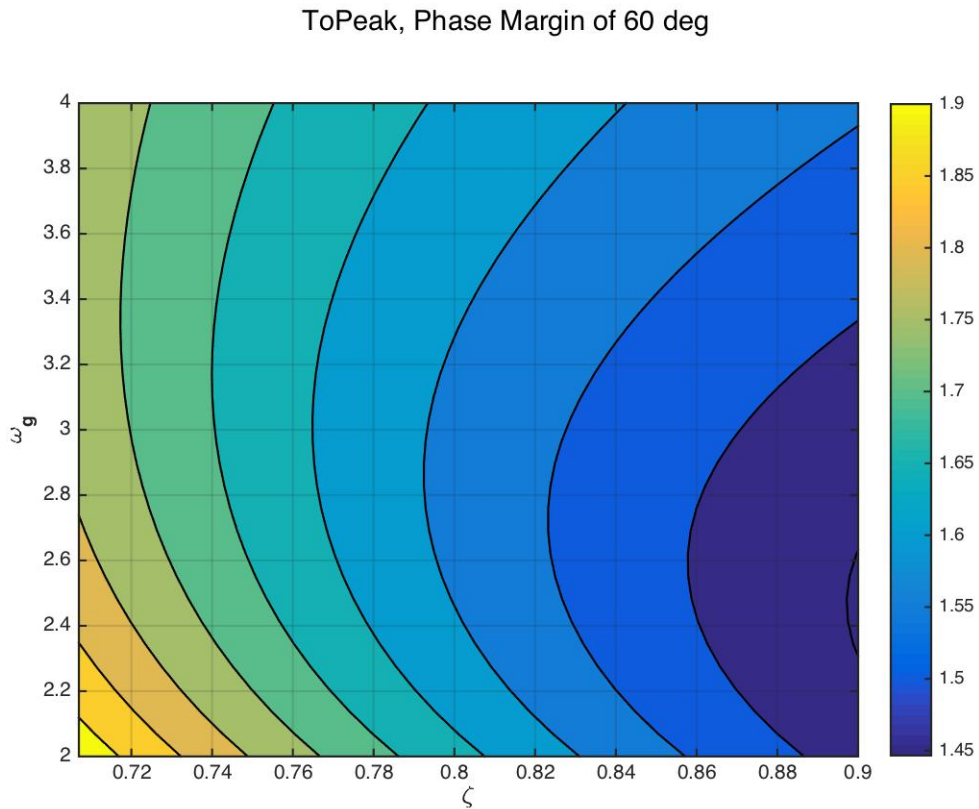


**Figure 4.6:** Reference to output (  $\zeta$  vs  $\omega_g$  ) for PM 60 deg

- As  $\zeta$  increases  $|T_o|_{peak}$  decreases significantly .
- As  $\omega_g$  increases  $|T_o|_{peak}$  decreases initially and again increases with  $\omega_g$ .

ToPeak, Phase Margin of 70 deg

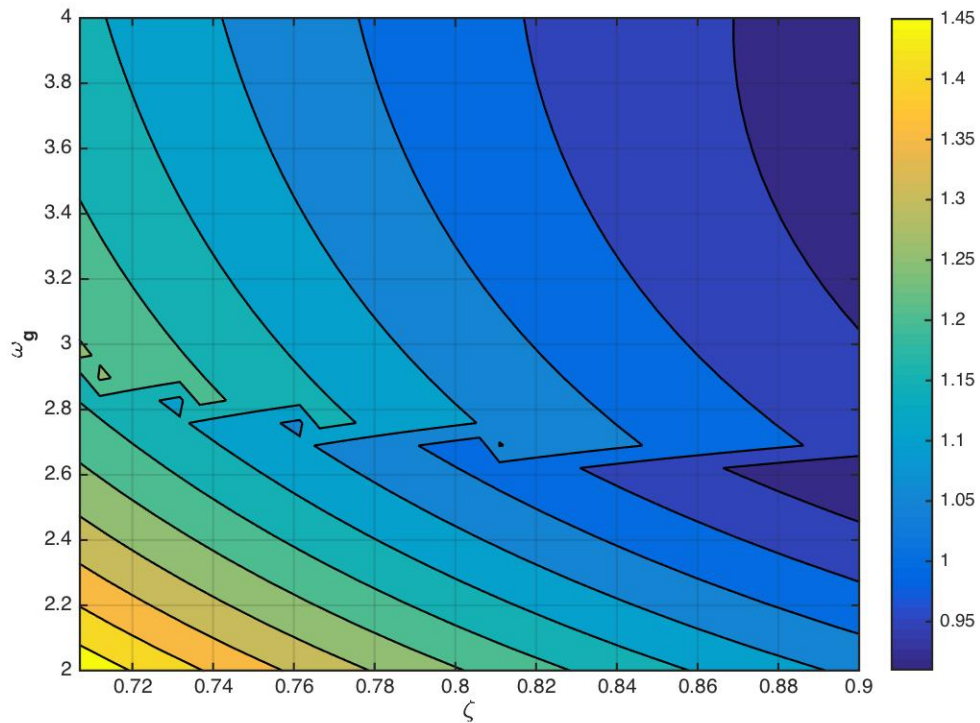


**Figure 4.7:** Reference to output ( $\zeta$  vs  $\omega_g$ ) for PM 70 deg

- As  $\zeta$  increases  $|T_o|_{peak}$  decreases significantly .
- As  $\omega_g$  increases  $|T_o|_{peak}$  decreases gradually.

#### 4.1.5 Reference to control action

The following section discusses the effect of controller parameters on the KS frequency response. The transfer function for the reference to control action is illustrated in eqn(4.1.5)

$$T_{ru} = KS = K[I + PK]^{-1} \quad (4.11)$$

Figures from fig(4.8)-fig(4.10) illustrates the effect.

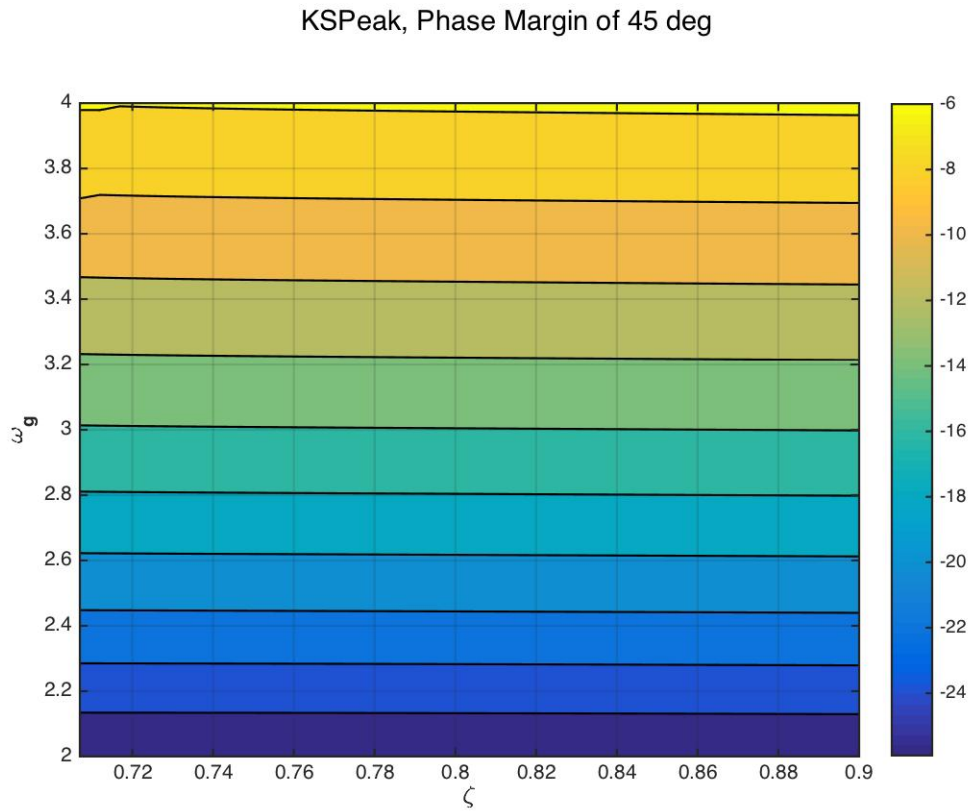


**Figure 4.8:** Reference to control action ( $\zeta$  vs  $\omega_g$ ) for PM 45 deg

- As  $\zeta$  increases  $|KS|_{peak}$  remains unaffected.

- As  $\omega_g$  increases  $|KS|_{peak}$  decreases significantly.

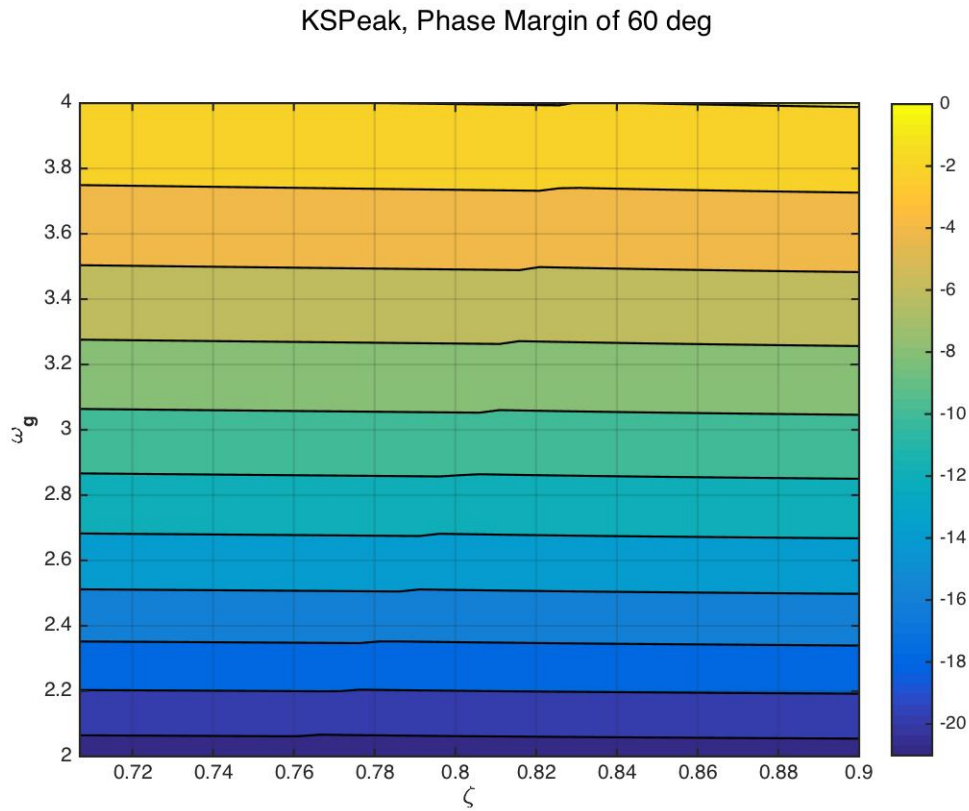


**Figure 4.9:** Reference to control action (  $\zeta$  vs  $\omega_g$  ) for PM 60 deg

- It shows a similar trend as fig(4.8).

KSPeak, Phase Margin of 70 deg

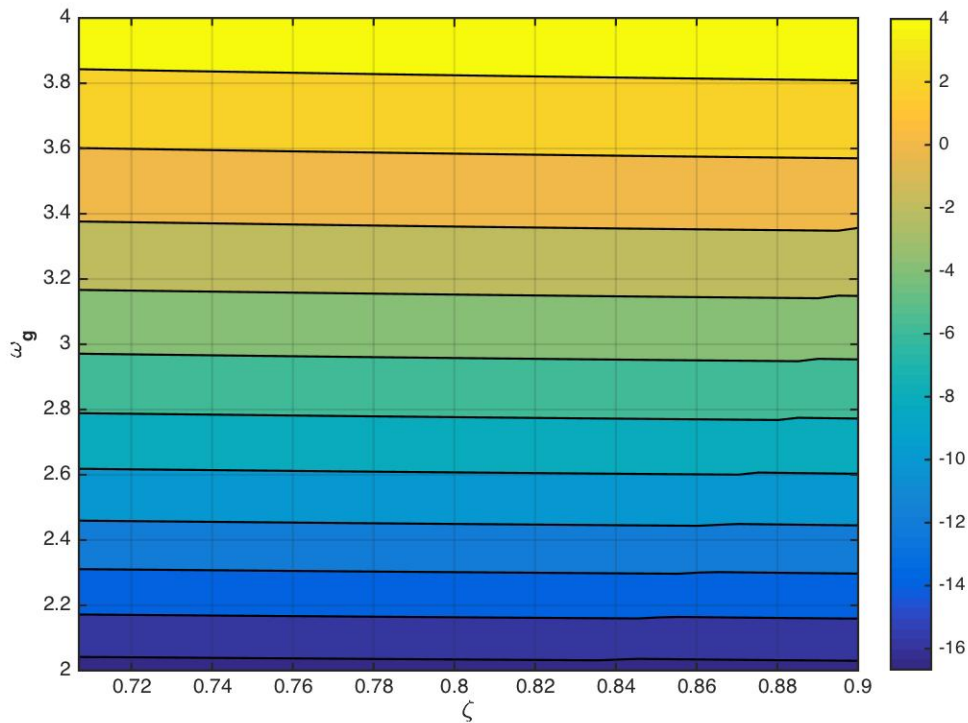


**Figure 4.10:** Reference to control action ( $\zeta$  vs  $\omega_g$ ) for PM 70 deg

- It shows a similar trend as fig(4.8) and fig(4.9)

#### 4.1.6 Disturbance to output

The following section discusses the effect of controller parameter on disturbance rejection. To assess the impact of output disturbances  $d_o$  on output  $y$  consider the following transfer function matrix from  $d_o$  to  $y$

$$T_{d_i y} = PS = P[I + PK]^{-1} \quad (4.12)$$

Figures from fig(4.11) - fig(4.13) illustrate this.

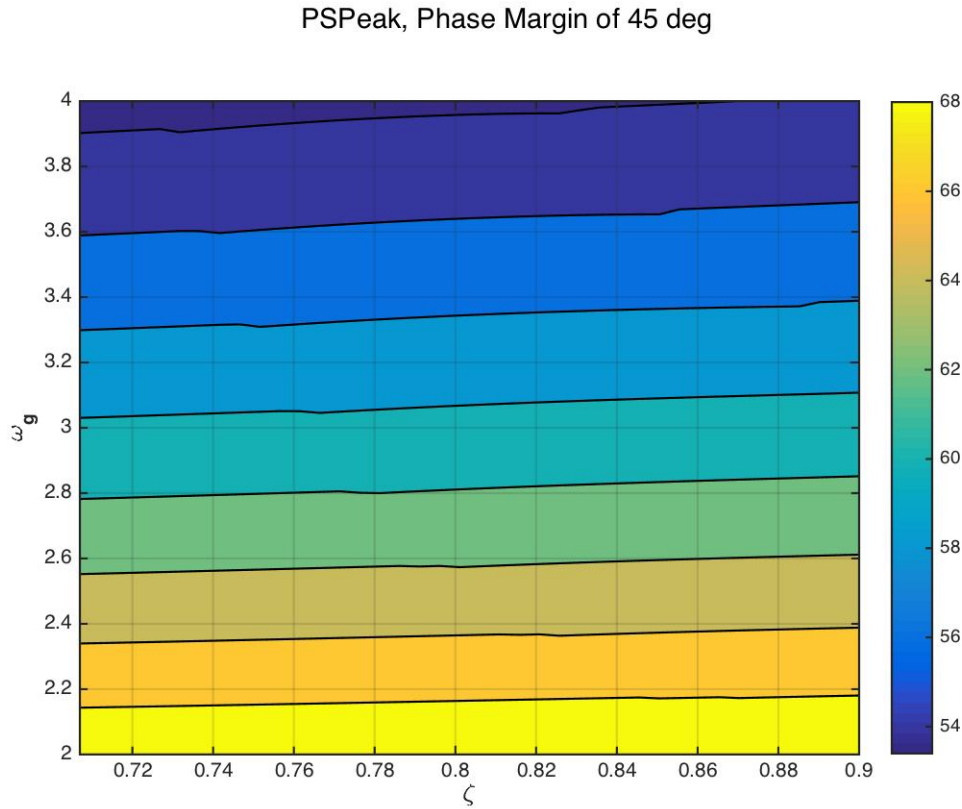


**Figure 4.11:** Input disturbances to output ( $\zeta$  vs  $\omega_g$ ) for PM 45 deg

- As  $\zeta$  increases  $|PS|_{peak}$  remains unaffected.

- As  $\omega_g$  increases  $|PS|_{peak}$  decreases significantly.

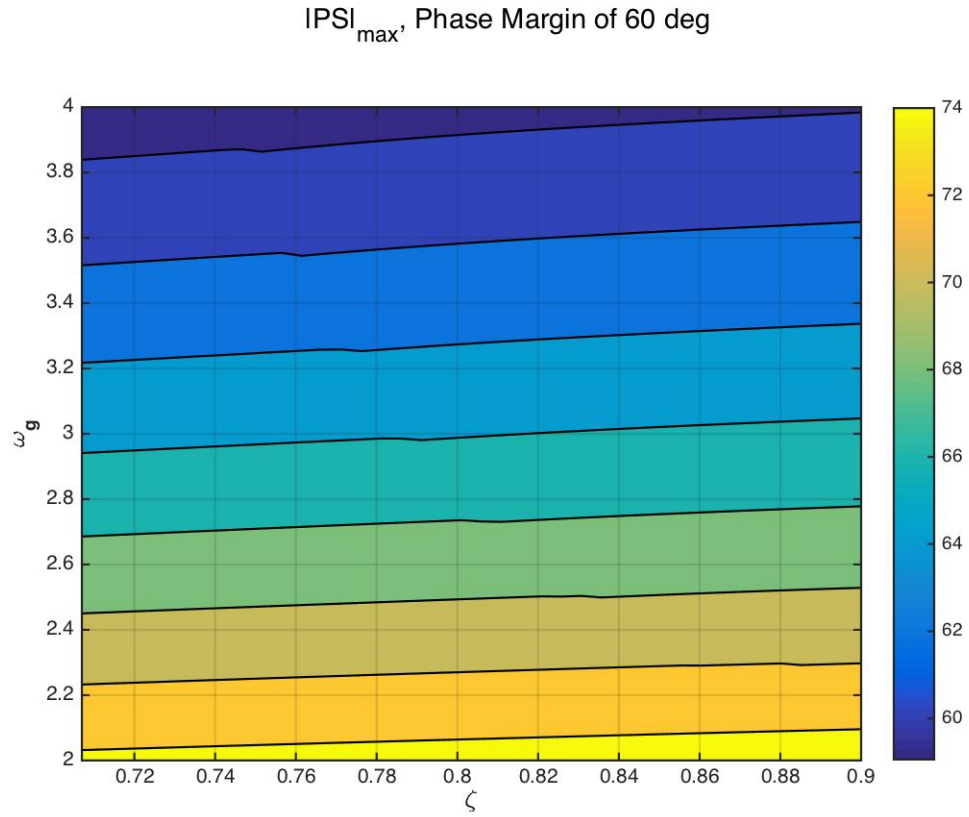


**Figure 4.12:** Input disturbances to output ( $\zeta$  vs  $\omega_g$ ) for PM 60 deg

- As  $\zeta$  increases  $|PS|_{peak}$  remains unaffected.
- As  $\omega_g$  increases  $|PS|_{peak}$  increases significantly.

PSPeak, Phase Margin of 70 deg

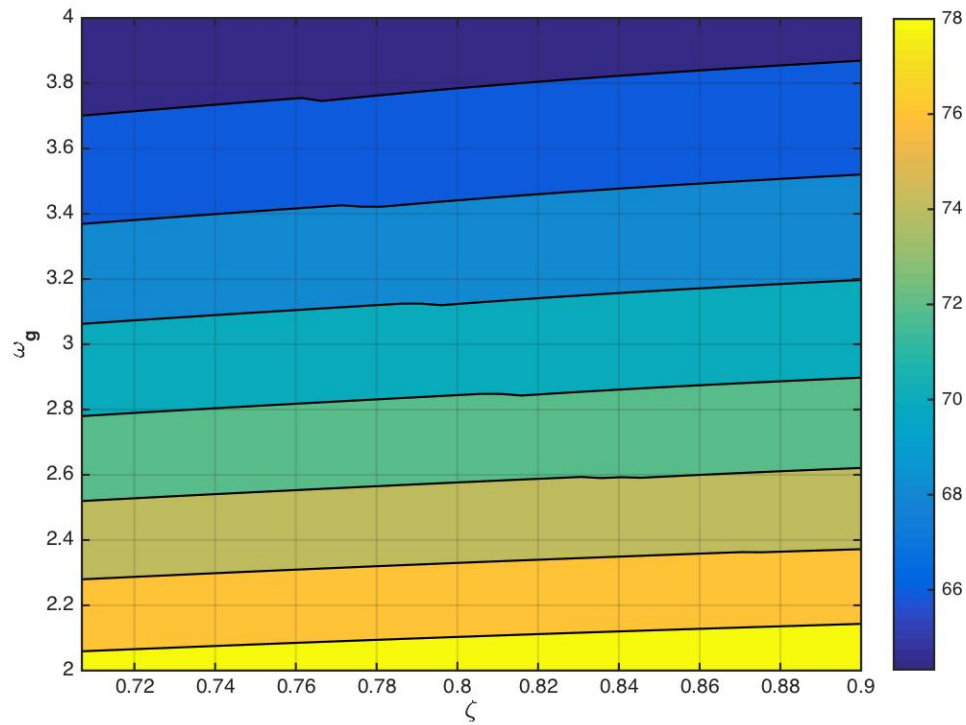


**Figure 4.13:** Input disturbances to output ( $\zeta$  vs  $\omega_g$ ) for PM 70 deg

- As  $\zeta$  increases  $|PS|_{peak}$  remains unaffected.
- As  $\omega_g$  increases  $|PS|_{peak}$  decreases slightly.

#### 4.1.7 % Overshoot

The following section discusses the effect on the Overshoot with variation in the controller parameters. Figures from fig(4.14) to (4.16) show the effect of controller parameters

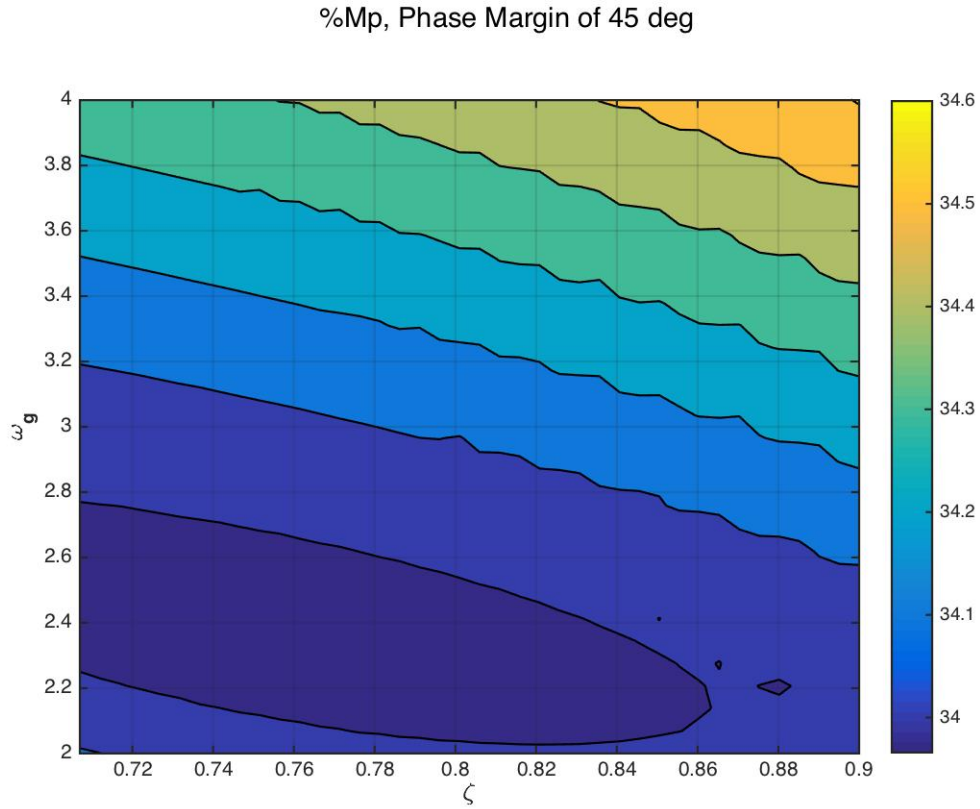


**Figure 4.14:** %  $M_p$  (  $\zeta$  vs  $\omega_g$  ) for PM 45 deg

- As  $\zeta$  increases % Mp remains fairly constant.
- As  $\omega_g$  increases % Mp decreases gradually.

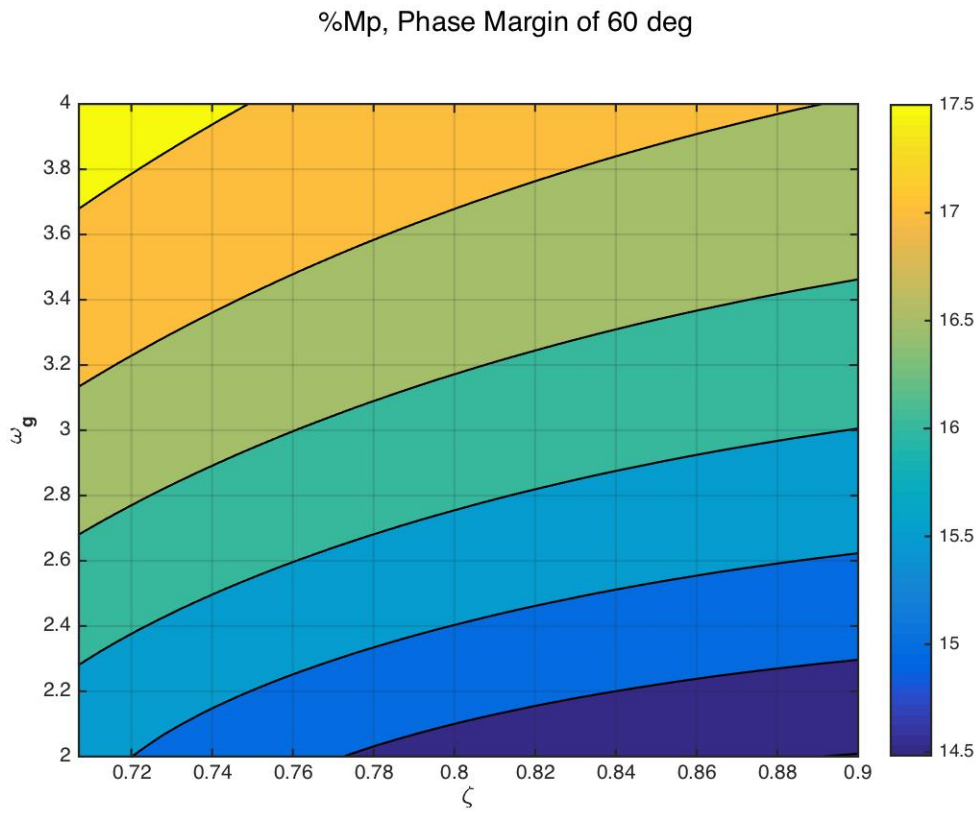


**Figure 4.15:** %  $M_p$  (  $\zeta$  vs  $\omega_g$  ) for PM 60 deg

- As  $\zeta$  increases % Mp decreases gradually.
- As  $\omega_g$  increases % Mp decreases significantly.

%Mp, Phase Margin of 70 deg

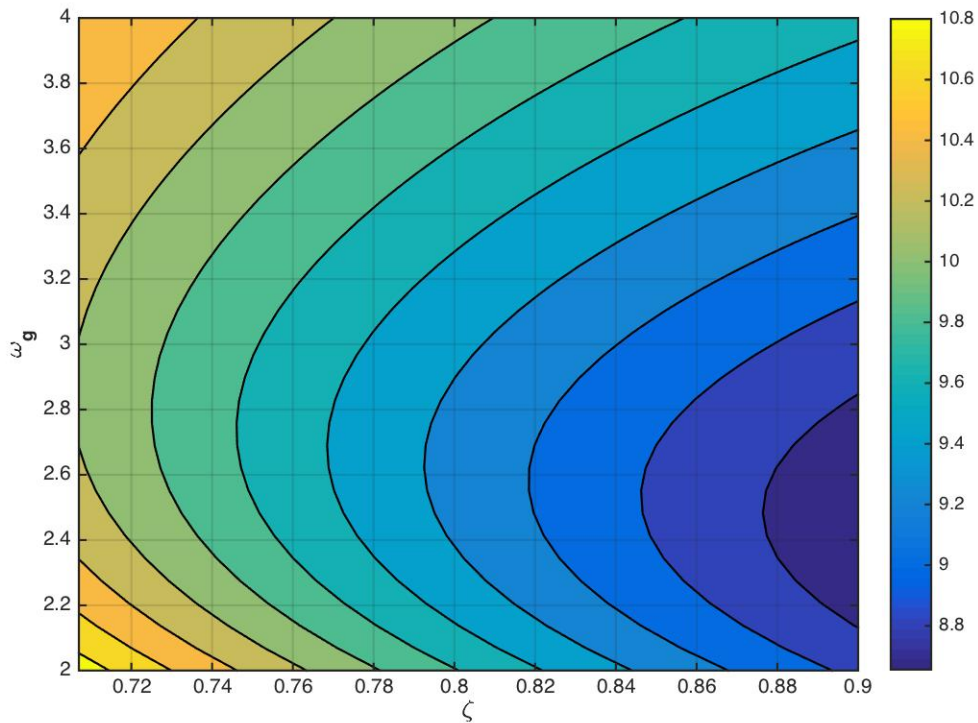


**Figure 4.16:** %  $M_p$  (  $\zeta$  vs  $\omega_g$  ) for PM 70 deg

- As  $\zeta$  increases % Mp decreases significantly.
- As  $\omega_g$  increases % Mp decreases initially and again increases with  $\omega_g$

#### 4.1.8 Settling Time

The following section discusses the effect of controller parameters on the settling time of the system. Figures fig(4.17) and fig(4.18) illustrate the effect of controller parameters.

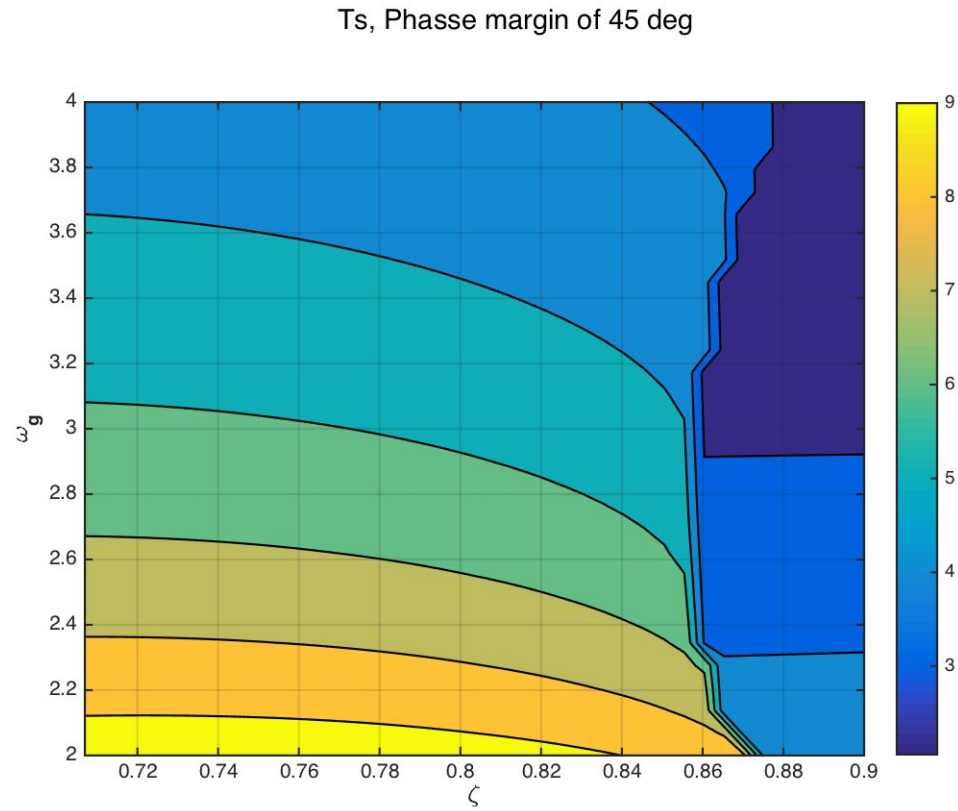


**Figure 4.17:**  $T_s$  (  $\zeta$  vs  $\omega_g$  ) for PM 45 deg

$T_s$ , Phasse margin of 60 deg

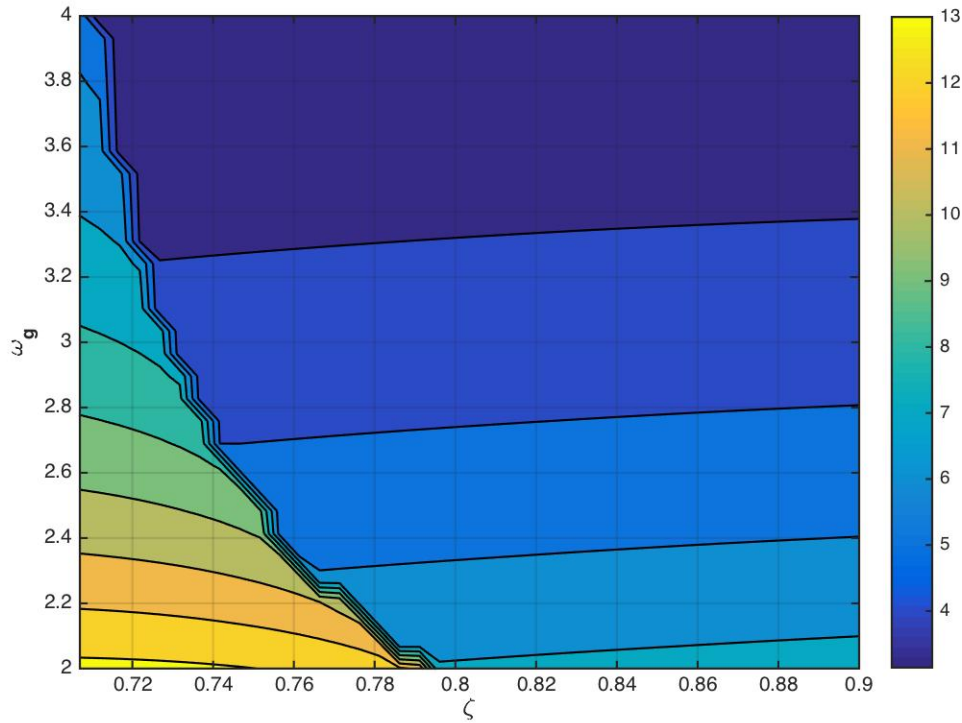


**Figure 4.18:**  $T_s$  ( $\zeta$  vs  $\omega_g$ ) for PM 60 deg

From fig(4.14) - fig(4.16) we see that in order to get a %  $M_p \leq 20\%$  we need a Phase margin of atleast 60 deg From Fig(4.17)-fig(4.18), for having a settling time ( $T_s \leq 6$  sec) we need  $\omega_g \geq 3$  rad/sec.

## 4.2 Controller simulation

The following figures represent the bode magnitude of the system when  $\zeta$  is 0.8 for unity gain crossover frequencies from 2 rad/sec to 16 rad/sec are shown.

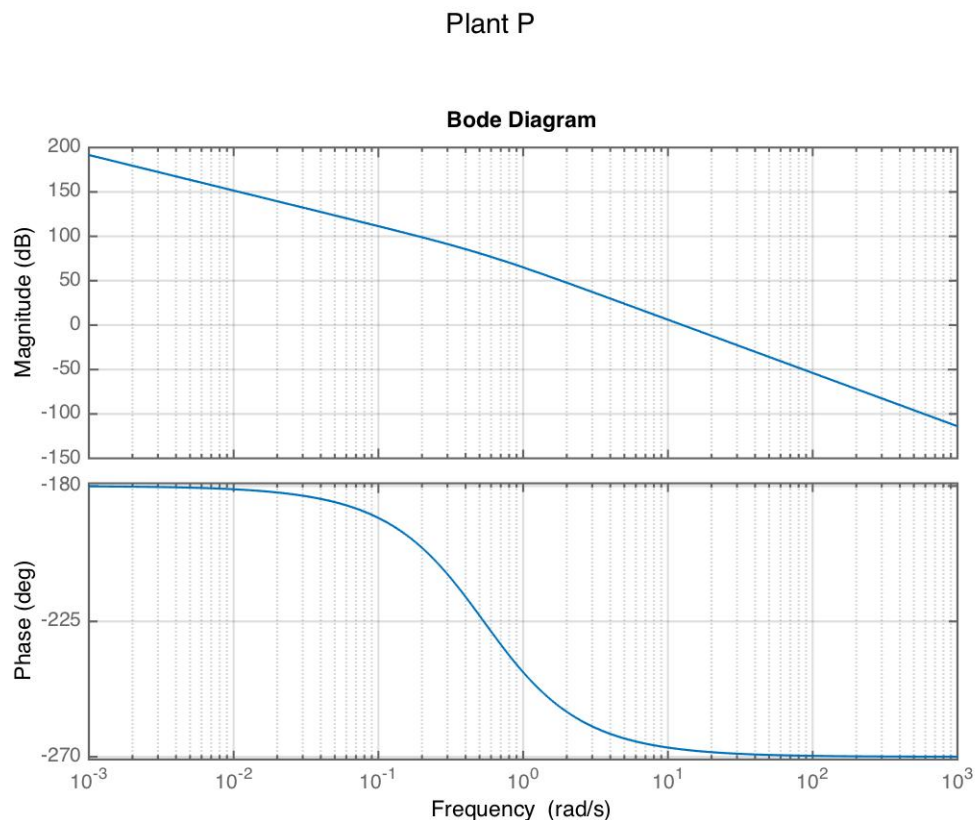


**Figure 4.19:** Nominal Plant :P

Controller K ,  $\zeta=0.8$

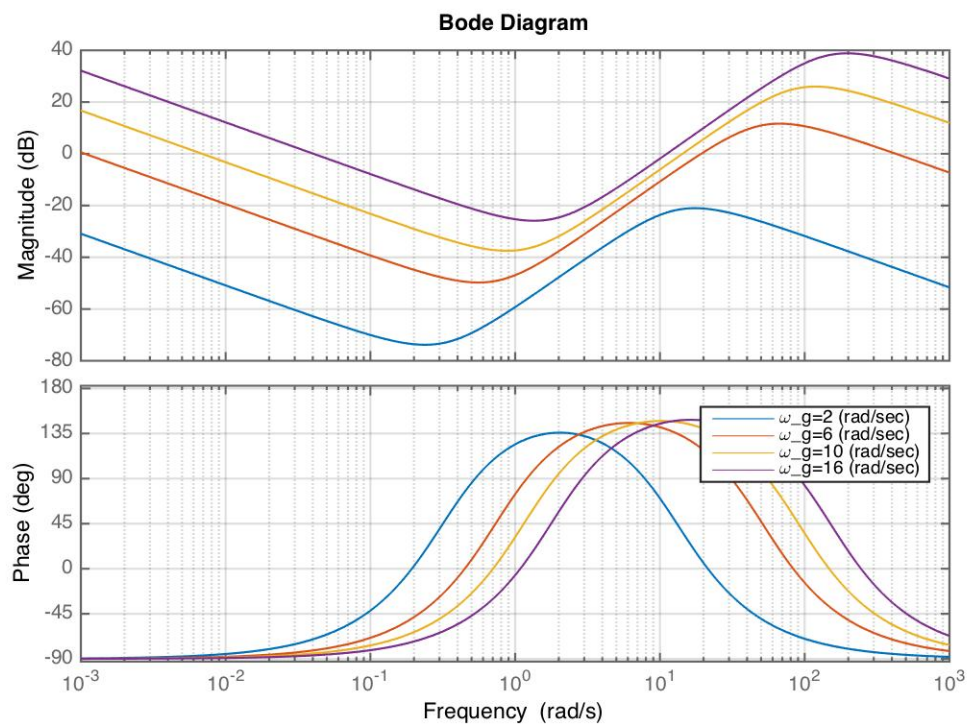


**Figure 4.20:** Controller

- As  $\omega_g \uparrow |K| \uparrow$ .

### Open Loop [L]= PK

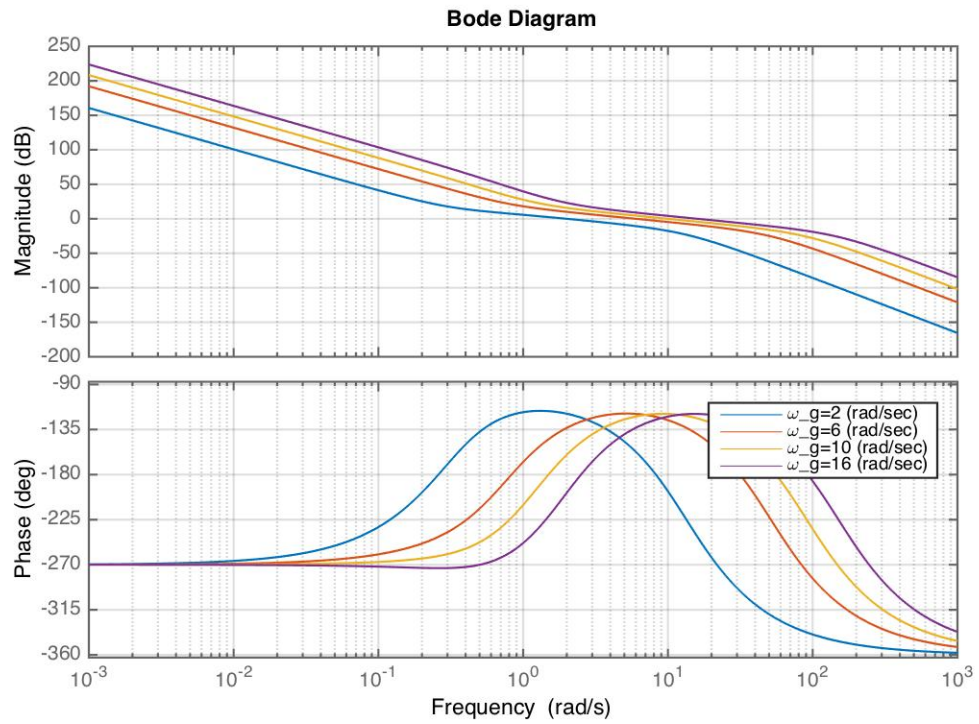


**Figure 4.21:** Open Loop : L

The open loop bode magnitude plot shows the singular values for the second input channel

- The singular values decrease with a slope of -60 db/dec due to two integrators from the plant and one integrator from the controller.
- Low frequency reference commands will be followed.
- Low frequency output disturbances will be attenuated.
- High frequency sensor noise will be attenuated.

Reference to error :  $T_{re}$ ,  $\zeta=0.8$

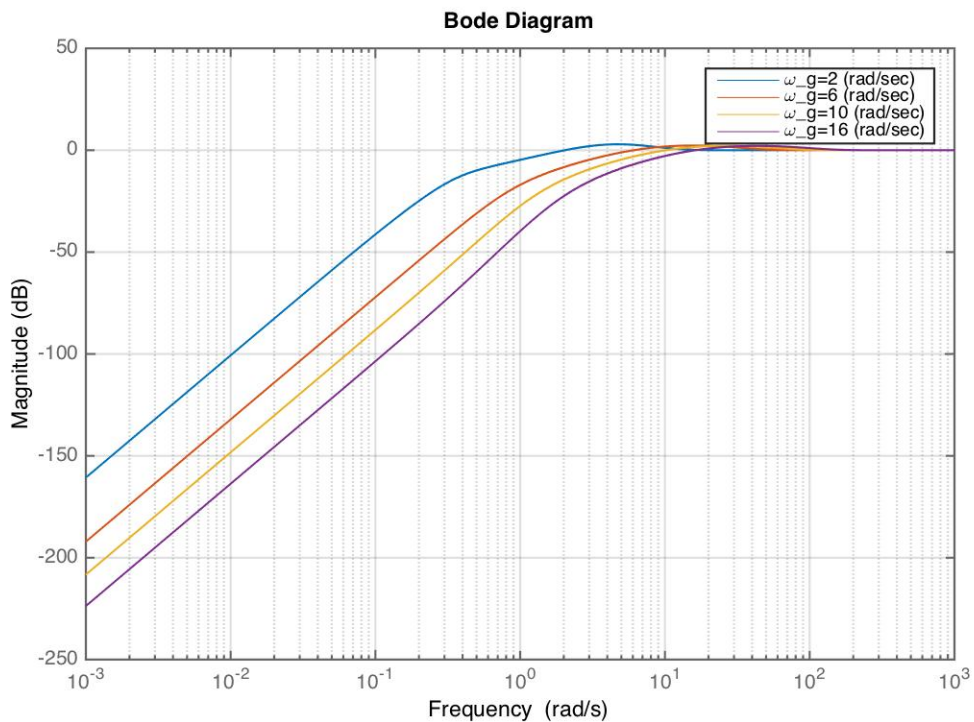


**Figure 4.22:** Sensitivity :  $|S_o|$

The sensitivity singular values are plotted using the bode magnitude plot. The plot suggests that

- Low frequency reference commands will be followed.
- Low frequency output disturbances will be attenuated.

Reference to output :  $T_{ry}$ ,  $\zeta=0.8$

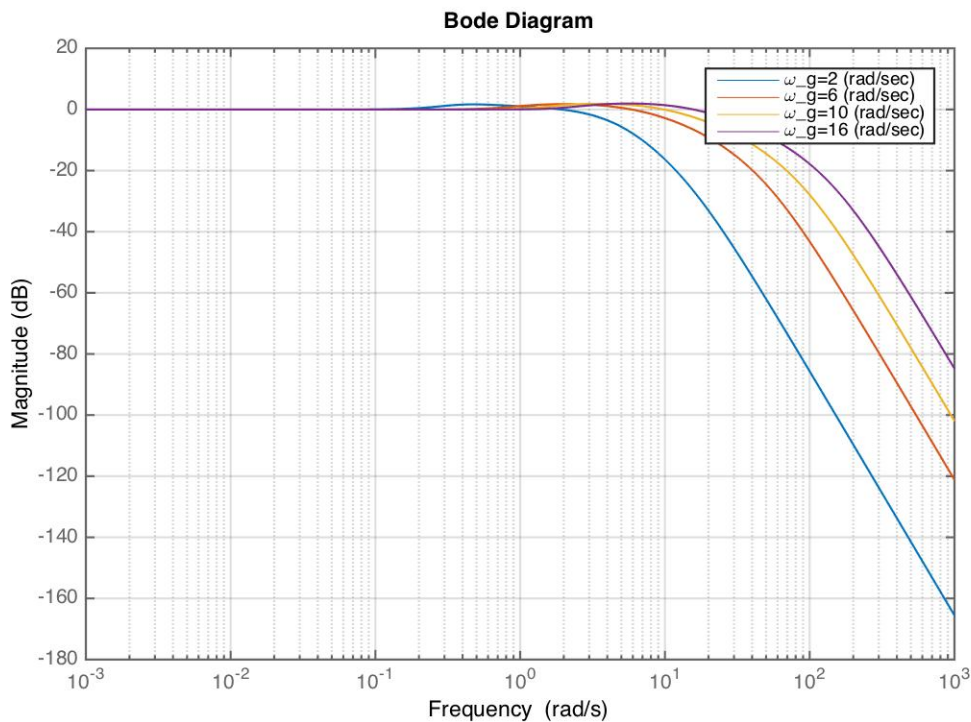


**Figure 4.23:** Complimentary Sensitivity :  $|T_o|$

The bode magnitude plot for the complimentary sensitivity suggests that

- Low frequency reference commands will be followed.
- High frequency sensor noise will be attenuated.

Reference to Control :  $T_{ru}$ ,  $\zeta=0.8$

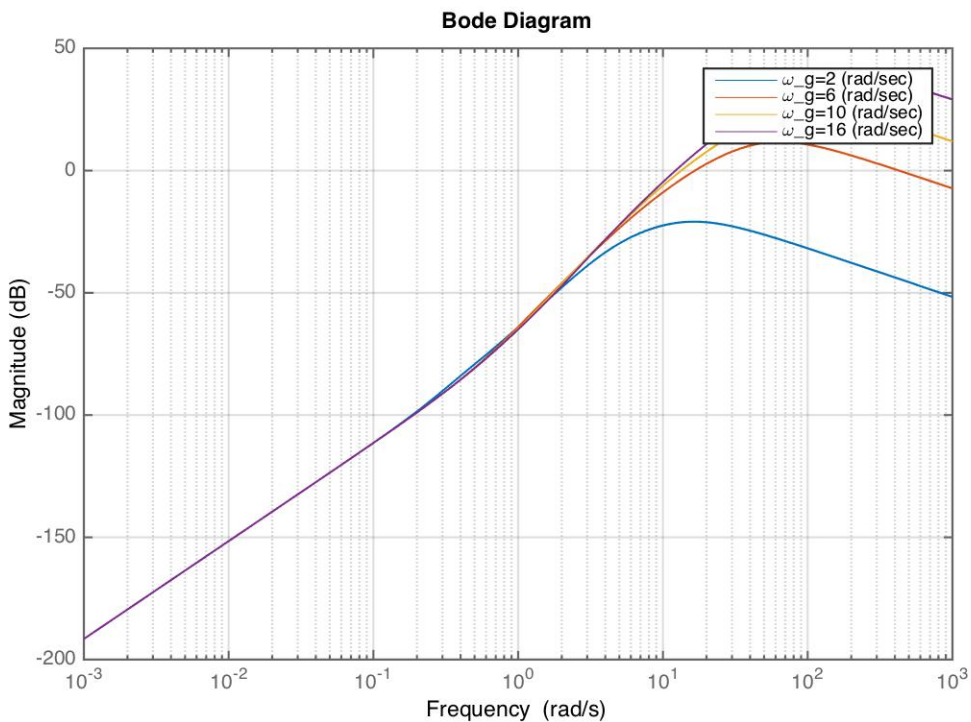


**Figure 4.24:** Reference to Control Action :  $|KS|$

- From eqn(4.1.5) we see that low frequencies  $|KS|$  is  $|P|^{-1}$ . Thus we have very little control action at low frequencies.

Fig(4.24) will help us assess the impact of the control inputs.

- Low frequency reference commands will be attenuated.

Input Disturbance to Output :  $T_{\text{diy}}$ ,  $\zeta=0.8$

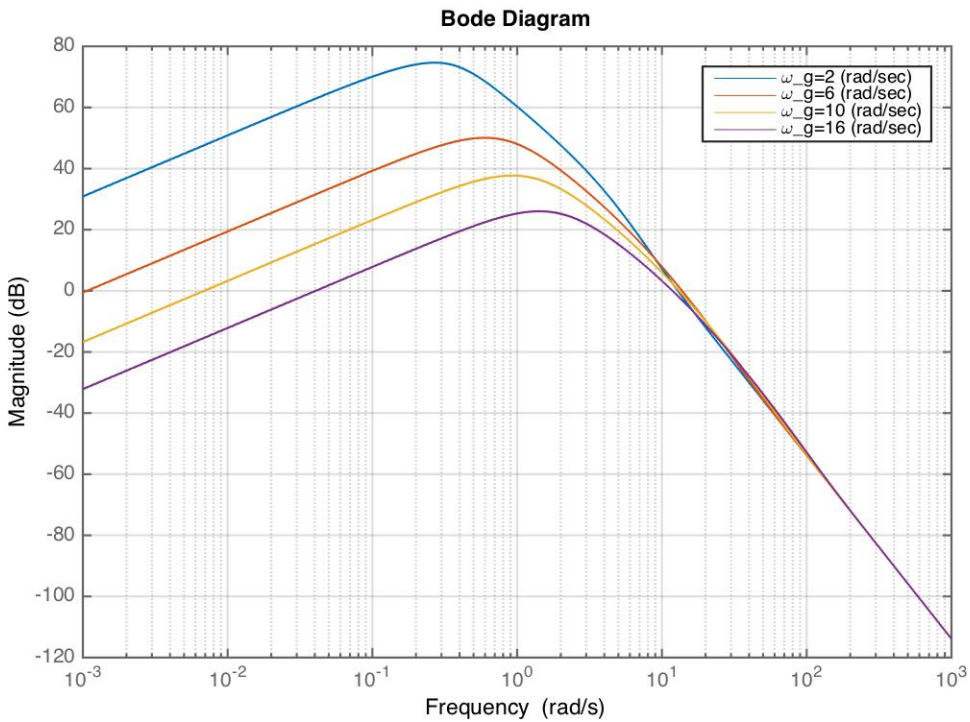


**Figure 4.25:** Input Disturbance to Output :  $|PS|$

- From eqn(4.1.6) we see that at low frequencies  $|PS|$  is  $|K|^{-1}$ . Thus we have little input disturbance rejection at low frequencies.

To assess the impact of the input disturbances we consider the fig(4.25)

- High frequency input disturbances will be attenuated.

#### 4.2.1 Linear Simulation

The controller developed for the vertical velocity and the forward velocity from eqn(4.5) and eqn(4.4) was implemented on a linear model of the quadrotor for different flight modes as shown in the figures below

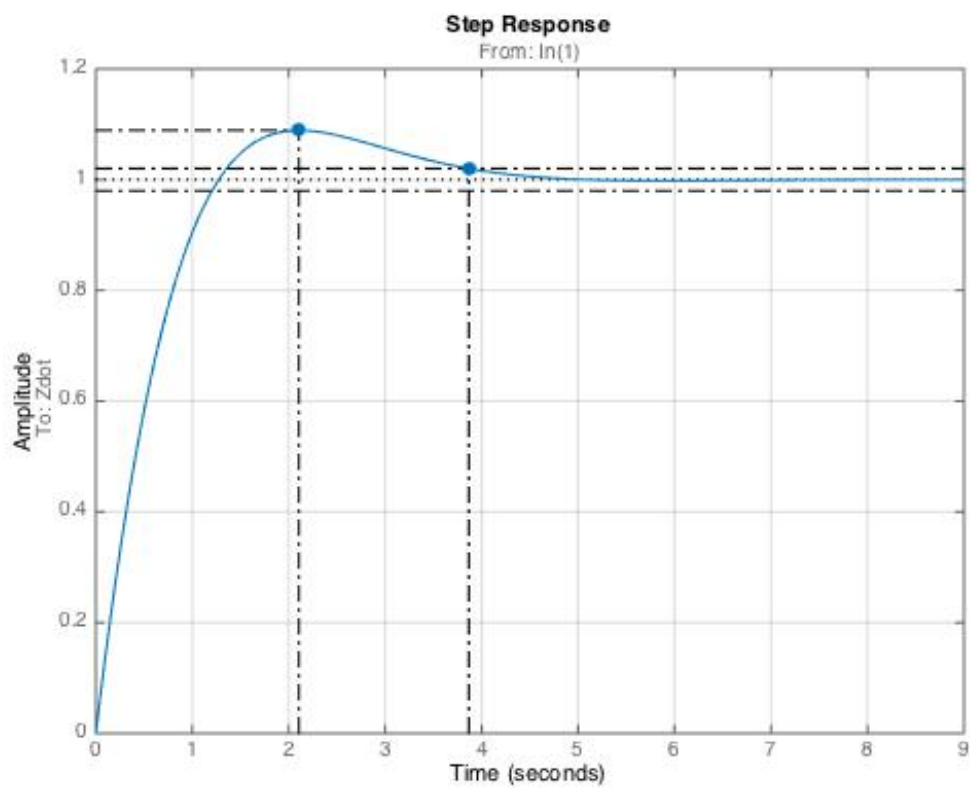


**Figure 4.26:** Step response: Hover Controller

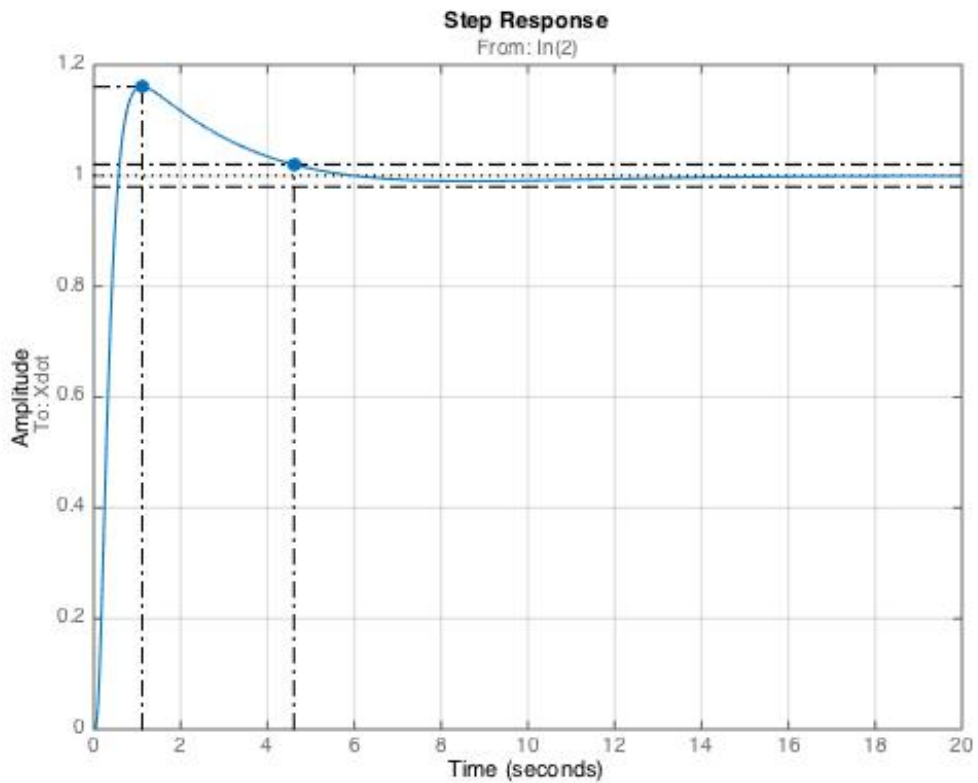


**Figure 4.27:** Step response:  $\dot{x} = 1 \text{ m/s}$

### 4.3 Summary and Conclusions

This chapter described a methodology for generating controller for hover and longitudinal mode for a quadrotor using a classical leadlag approach. From the analysis we see that there exists a tradeoff between input disturbance rejection and control action.

## Chapter 5

### SUMMARY AND DIRECTIONS FOR FUTURE RESEARCH

#### 5.1 Summary

In this report, a comprehensive modeling strategy was developed. A classical PID and lead-lag control design procedure was illustrated to see the trade-offs in the performance characteristics. Implementation of LTI model with the controller was illustrates the utility of the design strategy.

#### 5.2 Directions for Future Research

Future efforts would be directed towards incorporating a more accurate aerodynamic drag model and propeller dynamic model to model the effects more precisely. The control strategy would be tested to see the limits of applicability of SISO controllers using the tool developed in this report. A multi-variable control strategy is one of the avenues still remaining to be explored.

## REFERENCES

- [1] Beard, R. W., “Quadrotor dynamics and control”, Brigham Young University (2008).
- [2] Bouadi, H. and M. Tadjine, “Nonlinear observer design and sliding mode control of four rotors helicopter”, World Academy of Science, Engineering and Technology **25**, 225–229 (2007).
- [3] Boyne, W. J. and D. S. Lopez, “The age of the helicopter–vertical flight”, Washington, DC: Smithsonian (1984).
- [4] Castillo, P., R. Lozano and A. Dzul, “Stabilization of a mini rotorcraft with four rotors”, IEEE Control Systems Magazine **25**, 6, 45–55 (2005).
- [5] Gonzalez-Sanchez, M., L. Amezquita-Brooks, E. Liceaga-Castro and P. d. C. Zambrano-Robledo, “Simplifying quadrotor controllers by using simplified design models”, in “Decision and Control (CDC), 2013 IEEE 52nd Annual Conference on”, pp. 4236–4241 (IEEE, 2013).
- [6] Hoffmann, G. M., H. Huang, S. L. Waslander and C. J. Tomlin, “Quadrotor helicopter flight dynamics and control: Theory and experiment”, in “Proc. of the AIAA Guidance, Navigation, and Control Conference”, vol. 2 (2007).
- [7] Huang, H., G. M. Hoffmann, S. L. Waslander and C. J. Tomlin, “Aerodynamics and control of autonomous quadrotor helicopters in aggressive maneuvering”, in “Robotics and Automation, 2009. ICRA’09. IEEE International Conference on”, pp. 3277–3282 (IEEE, 2009).
- [8] Kroo, I., F. Prinz, M. Shantz, P. Kunz, G. Fay, S. Cheng, T. Fabian and C. Partridge, “The mesicopter: A miniature rotorcraft concept–phase ii interim report”, (2000).
- [9] Luukkonen, T., “Modelling and control of quadcopter”, Independent research project in applied mathematics, Espoo (2011).
- [10] Messner, W., “The development, properties, and application of the complex phase lead compensator”, in “American Control Conference, 2000. Proceedings of the 2000”, vol. 4, pp. 2621–2626 (IEEE, 2000).
- [11] Messner, W. C., M. D. Bedillion, L. Xia and D. C. Karns, “Lead and lag compensators with complex poles and zeros design formulas for modeling and loop shaping”, Control Systems, IEEE **27**, 1, 44–54 (2007).
- [12] Pounds, P., R. Mahony and P. Corke, “Modelling and control of a quad-rotor robot”, in “Proceedings Australasian Conference on Robotics and Automation 2006”, (Australian Robotics and Automation Association Inc., 2006).
- [13] Raffo, G. V., M. G. Ortega and F. R. Rubio, “An integral predictive/nonlinear h control structure for a quadrotor helicopter”, Automatica **46**, 1, 29–39 (2010).

- [14] Rodriguez, A., *Analysis and Design of Multivariable Feedback Control Systems* (CONTROL3D,L.L.C., Tempe, AZ, 2002).
- [15] Stevens, B. L. and F. L. Lewis, *Aircraft control and simulation* (John Wiley & Sons, 2003).
- [16] Tayebi, A. and S. McGilvray, “Attitude stabilization of a four-rotor aerial robot”, in “Decision and Control, 2004. CDC. 43rd IEEE Conference on”, vol. 2, pp. 1216–1221 (IEEE, 2004).